Radiative Response on Massive Noble Gas Injection For Runaway Suppression in Disruptive Plasmas

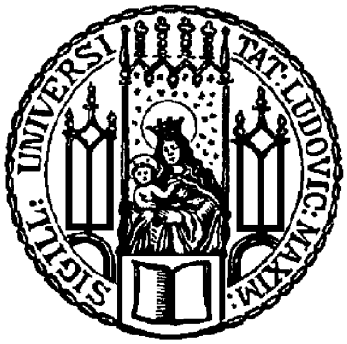

Dissertation
der Fakultät für Physik
der Ludwig-Maximilians-Universität München

von
Bernhard Reiter
aus Traunstein

München, 21. Mai 2010

Erstgutachter:	*Prof. Dr. H. Zohm*
Zweitgutachter:	*Prof. Dr. F. Krausz*
Datum der mündlichen Prüfung:	*16.09.2010*

Zusammenfassung

In einem disruptiven Tokamakplasma entsteht durch abruptes Kühlen ein relativ starkes elektrisches Feld, welches Elektronen in das relativistische Geschwindigkeitsregime beschleunigen kann. Relativistische Elektronen, die sogenannten Runaways, akkumulieren Energieen im MeV Bereich, vermehren sich multiplikativ und können erheblichen Schaden anrichten, wenn sie auf die Wand des Vakuumgefäßes treffen, was insbesondere für Fusionsreaktoren der nächsten Generation ein ernsthaftes Problem darstellt.

Diese Dissertation verfolgt das Prinzip der abrupten Erhöhung der Elektronendichte im gesamten Plasma durch lokale, massive Injektion von Edelgasen. Die sich daraus ableitende Erhöhung der Reibungskräfte soll Runaway-Population unterdrücken. Die Tatsachen, dass der Prozess auf kleinen, disruptionstypischen Zeitskalen abläuft und gleichzeitig die Verteilung der injizierten Materie im dreidimensionalen Raum charakterisiert werden soll, stellt die Diagnostizierungsmethoden in einem solchen Experiment vor hohe Anforderungen.

Um Einblicke in die Wechselwirkungsdynamik zwischen der kalten Materiefront und dem heissen Plasma zu erlangen, wurde im Zuge dieser Arbeit ein System zur Messung breitbandiger elektromagnetischer Strahlung aufgebaut. Die Diagnostik basiert auf der AXUV-Technologie und umfasst 176 Sichtlinien, deren räumliche Anordung die Erfassung der helikalen Strahlungspropagation erlaubt.

Diese Arbeit eröffnet den Einblick in die Dynamik und die große Asymmetrie der Strahlungsverteilung unter der Ausbildung komplexer filamentärer Strukturen. Eine derartige Charakterisierung der Strahlungspropagation erlaubt es ausserdem, Rückschlüsse auf die Trajektorien der Ionen zu treffen.

Die Ergebnisse dieser Arbeit fließen direkt ein in die weitere Entwicklung von Injektionsverfahren zur effektiven Runaway-Unterdrückung in zukünftigen Fusionsanlagen wie ITER.

Abstract

In a disruptive tokamak plasma, rapid cooling induces a high electric field, which potentially pushes electrons into the relativistic velocity regime. Relativistic electrons, the so-called *runaways*, accumulate many MeV, they multiply quickly and can cause substantial damage when they hit the wall of the vacuum vessel. This constitutes a big challenge in particular for fusion devices of the next generation.

This thesis follows the principle of rapidly increasing the electron density up to values, where the retarding collisional force leads to a suppression of runaway population. The method of injecting high amounts of noble gas particles locally into the plasma is put into practice in the ASDEX Upgrade fusion test facility. The prerequisite for the success of this approach is the spatially uniform redistribution of the injected particles on short timescales typical for disruptions.

In the framework of this thesis, a multi-channel photometer system was built with the intention of diagnosing the spatial propagation of radiation. The new diagnostic employs the AXUV technology and is equipped with 176 lines of sight. It is made up by toroidally spaced detectors, which allows for unfolding the helical transport times. This thesis reveals the asymmetric radiation evolution growing from a highly dynamic zone of interaction between cold injected matter and hot plasma. Complex filamentary structures in the plasma periphery formed during the injection process are analysed and characterised.

The results of this thesis directly support the further development of methods for future experiments on runaway suppression, which are of great value for next generation devices like ITER.

Acknowledgements

I am very grateful to Prof. Hartmut Zohm, who made it possible for me to carry out this thesis at the *Max Planck Institute of Plasma Physics* in Garching. I kindly acknowledge also for his stimulating comments on the manuscript of this thesis.

I would like to thank very much Dr. Gabriella Pautasso, who also supported the manuscript and generously assisted my work.

Many thanks to Dr. Thomas Eich for buying all the nice diagnostic equipment and making comments on several talks performed in the course of the work and also on some parts of this manuscript.

Many thanks to Dr. Josef Neuhauser, who was very interested in my results and inspired me in very helpful discussions. Sincere thanks for the comments on this manuscript.

Thank you goes to Dr. Ralph Dux and to Prof. A. Kallenbach for their suggestions and comments on the manuscript of this thesis.

I am indebted to Dr. Asher Flaws, who supported me for generating the very first tomograms with my diagnostic. His groundwork helped me a lot for coming faster to successful disruption analysis.

Thank you goes also to Dr. Tilman Lunt. He provided the codes for the impressive 3-D visualisation of the vessel and adjusted the CMOS camera according to my wishes.

I am very grateful to Dr. Mark Maraschek, who adjusted his programs to my diagnostic and helped in many questions regarding data acquisition as well as magnetic mode analysis.
I wish to thank also Dr. Valentin Igochine and Dr. Anja Gude, who allowed me to use their setup for diode calibration. Thanks also to Dr. J. C. Fuchs for providing magnetic equilibrium data.

Thank you goes to Dr. Martin Balden, for helping me with the focused ion beam microscopy and the EDX device.

In addition, I am indebted to all the technicians for their support. Especially, Heinz Wolf for giving me the possibility of using his laboratory. The team of Dr. Albrecht Herrmann, for their help during the installation times inside the vessel, Michael, Florian and Gabi. In particular, of course, Wolfi Zeidner, who measured the camera positions many many times. I am very grateful to the electricians, forth and foremost Ludwig Kammerloher, who perfectly tackled the problems came about through many unforseen issues. Thanks also to Gerald Sellmair, Thomas Schwarz, Horst Eixenberger and Gerold Schramm. Also,

many thanks to the DAQ group of Dr. Karl Behler, especially Andreas Lohs and Helmut Blank.

Many thanks to Christian Vogel, for helping me to plan the excursions of graduate students during our time as students representatives.

Finally, I dedicate this work to my family, which has supported me as long as I can think.

Bernhard Reiter Munich, 21st May 2010

Contents

Chapter I

INTRODUCTION

Aspects of nuclear fusion were initially considered in discussions on earth's and sun's age inceptioned in the second half of the 19^{th} century. Geologists and evolutionary researchers claimed that earth could not be much younger than about 300 millions of years, which posed the moving question, how the sun is able to burn for such a long time. A battery of questions constituted the starting point for finding the pieces of a scientific puzzle. Several approaches went nowhere until Albert Einstein introduced the famous relation $E = m\,c^2$. The mass-energy equivalence in combination with some other important puzzle pieces shed new light on the mechanisms interior of the sun: Aston's discovery that four hydrogen nuclei are heavier than one helium nucleon (1920), Eddington's proposal of fusion of hydrogen in the core of the sun (isochronal), the earlier discovery of helium in the solar spectrum by Lockyer (1890), Payne's confirmation of hydrogen being the main component in the sun (1925), investigations on the quantum mechanical tunnelling by Gamov, Gurney and Condon and, finally, Bethe's quantitative calculations on the fusion reaction in a hydrogen plasma[1] that is powering the sun (1939). Bethe was awarded the Nobel prize for Physics in 1967 [1], which clearly demonstrates the importance of his work.

The history of controlled fusion in a plasma of hydrogen isotopes began a bit delayed with respect to Bethe's work namely in the fifties, first and foremost by Spitzer in the US, Thomson in the UK and Sacharov and Tamm in the UDSSR. The researchers have been incited and have pursued from then on the idea of developing a sun-like energy source based on a self-sustained and eco-friendly principle. However, all devices that have been built until now, could not produce an energy gain sufficient for electric power production albeit one has to note that the present generation of fusion devices are test facilities and devoted to plasma experiments. Today, in the year 2010, we are already confronted with an extensive price pressure in the era of fossil fuels, which certainly grows in the near future and endangers international security and stability. Moreover, the climate change is one of the greatest challenges facing mankind. At the present stage of rapidly

[1] A plasma is a partly or fully ionised gas

developing energy demand of a steadily growing world's population, the future calls for an ecological-pragmatic politics, which puts high priority on the compromise between industry and environment. Nuclear fusion indeed promises to add significant contribution to an intelligent energy mix albeit not in the decades to come. It is still a long-term project which has to tackle complex issues. This thesis is devoted to one of the major problems for next generation devices: The plasma disruption in a tokamak[2].

The next generation device ITER[3] is currently under construction [2]. Its capabilities exude confidence of becoming a milestone on the way towards the fusion power plant *DEMO* [3]. The latter aims at demonstrating the principle of economical viability. The most relevant reactants for fusion on earth is deuterium (D) and tritium (T). In terms, it is expressed as

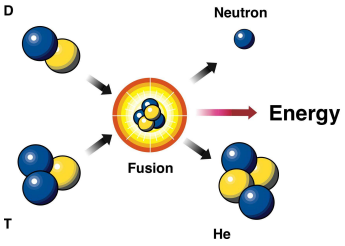

$$ {}^{2}_{1}\mathrm{D} \;+\; {}^{3}_{1}\mathrm{T} \;\rightarrow\; {}^{4}_{2}\mathrm{He} \;+\; {}^{1}_{0}\mathrm{n} \;+\; 17.6\,\mathrm{MeV}. $$

The quantities of deuterium and lithium required annually for a 1 Gigawatt fusion power plant could be delivered in a single truck. ITER is planned as a test reactor, which promises to produce fusion power of 500 MW at an energy gain of $Q = 5$-10. The quantity Q gives the ratio of α-particle related heating to input power.

Fusion is possible when the positively charged reactants are of sufficiently high kinetic energy for overcoming the mutual repulsing forces. The cross-section or probability for the reaction is small at low energies and reaches a maximum at about 64 keV. Particles in a plasma can be heated to very high temperatures by microwave resonance heating or by collisions with injected neutrals of high kinetic energy. In a fusion power plant, the α-particle itself shall deposit its kinetic energy within the plasma and sustain hereby the high temperature. Considering a plasma of potential reactants for fusion, it must be guaranteed that the nuclei react before they lose their energy. The generation of a plasma of hydrogen isotopes prerequisites an operation under vacuum conditions, where contact between the hot particles and the chamber wall has to be avoided. The plasma and its energy have to be confined - with at least a duration, which is long enough for making the impact at high temperatures possible. In this context, also the density plays a major role, because the more particles present, the higher is the reaction rate. The currently recognised assumption for the required *triple product* or *fusion product* is given by

$$ n\,\tau_{\mathrm{E}}\,T \;>\; 5 \times 10^{21}\,\mathrm{keV\,s\,m^{-3}}, \tag{I.1} $$

[2]Russian acronym equivalent for *'toroidal chamber with magnetic coils'*

[3]two meanings: *I*nternational *T*hermonuclear *E*xperimental *R*eactor and lat. *The Way*

in which n is the density, τ_{E} stands for the energy confinement time and T denotes the temperature. It has not been achieved by any fusion device yet. Two approaches are presently investigated for producing net energy gain from fusion in a plasma: The principle of inertial confinement and the magnetic confinement. The latter is subject of this thesis.

The tokamak confines the energy by steering the particles on fixed pathways. Helical field lines that wind around in the interior of the toroidal chamber close in themselves for avoiding end losses. The helical magnetic field line arrangement is due to a superposition of poloidal and toroidal magnetic fields. The latter is generated by external field coils - the earlier by an internal toroidally driven plasma current. This internal plasma current is of high magnitudes in the order of mega amperes. A small plasma resistivity allows for such high currents even at low loop voltages ranging in the order of 1 Volt. The plasma current is the fundamental property of the tokamak. It is necessary for sustaining equilibrium - on the other hand, the current instabilities can arise with the danger of rapid confinement losses and strong thermal energy expulsion. The dramatic event of an uncontrolled thermal energy removal followed by a rise of plasma resistivity leads to a quenching of the internal current. Such a process is referred to as disruption. The difference to the usual, preprogrammed plasma shut down is the time scale. A disruption reduces the thermal content on the sub-ms scale and the current drops within milliseconds[4]. Contrarily, a preprogrammed shut down can last several seconds. The rapidity of a disruption puts threat on vessel components due firstly to high thermal energy fluxes and secondly, due to hazardous inductive forces on surrounding conductors.

The knowledge about mitigating loads from the thermal and current quenches are nowadays relatively well established [29], [30]. This thesis is motivated by a furthermore consequence of the disruption: Synergetic effects in the run of a disruption can form toroidal beams of relativistic runaway electrons [81], which we name *runaways*[5] in what follows. A runaway beam potentially accumulates kinetic energies up to the order of several MeV during several millions of toroidal turns. If the toroidal beam is lost from the initial orbit without being collisionally decelerated by plasma electrons, it impinges the wall and can cause severe material damage even underneath the first wall [76], [77]. Runaways stand out upon the other wall load effects due to the localised high currents flowing into the material, where they deposit the energy by bremsstrahlung and ionisation [75]. Energy flux densities could reach values of up to 80 $\mathrm{MJ/m^2}$ within a few square centimetres [79], [78]. Runaway caused incidences are documented, such as a water leak

[4]The current decay time is different from device to device, ranging from a few milliseconds up to several tens of milliseconds

[5]Electrons of higher energy than 500 keV are relativistic, because these energies exceed the relativistic electron mass at rest ($E = mc^2$).

in the Tore Supra tokamak [83], or wall vapourisation in the JET tokamak[6]. Therefore, it is appropriate to control the trajectories of runaways - if they are unavoidable - by the magnetic field. Impressive experiments on active runaway beam positioning in Tore Supra were performed [84] and experiments towards runaway control in the DIII-D tokamak are ongoing. Both exude some optimism.

In the context of predictions for the hazardousness of runaways in ITER, one has to involve scaling rules, because the ITER device is designed for higher plasma parameters compared to existing tokamaks. Figure I.1 shows the relations between three tokamaks.

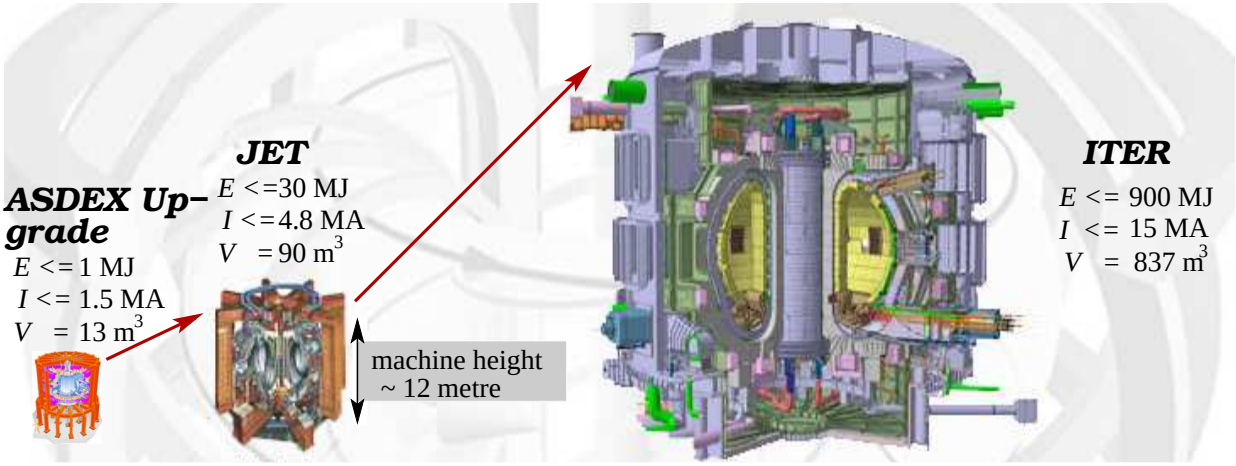

Figure I.1: True-to-scale cutaway of Germany's largest facility ASDEX Upgrade (left), the European JET (middle) and the international device ITER. Source: ITER: http://www.iter.org/org/team/odg/comm/Pages/Images.aspx, 30.04.2010.

A scaling of the magnitude of disruption consequences is possible on the basis of empirical values gained from previously and currently operated tokamaks. For example, from ASDEX Upgrade to JET, scaling rules can be fixed on the basis of experimental results. Contrarily, from JET to ITER, great physical changes will accompany the drastical enlargement of the geometrical dimensions. Theoretical predictions play an important role for the ITER design and theoretical claims actually constitute that a disrupting plasma in ITER will be populated with runaways of magnitudes higher compared to presently known cases. This originates mainly from the longer disruption duration, which results in a higher runaway yield via avalanching.

[6] Joint European Torus

This thesis critically challenges massive gas injection (MGI) in order to achieve progress in examining whether a massive injection of noble gases during a disruption could suppress runaways in ITER. It follows the principle of rapidly fuelling the plasma core for enhancing the electron density up to values, at which the friction force on the electrons is in the order of the accelerating force on the thermal electron. Calculations on the target density are performed in [26]: The minimum total electron density[7] requested for collisional runaway suppression amounts approximately to $4{\times}10^{22}\,\mathrm{m}^{-3}$. This demands on a density increase of a factor of 500 with respect to the nominal background density around $8 \times 10^{19}\,\mathrm{m}^{-3}$.

For this purpose, we perform experiments in the ASDEX Upgrade device using a new kind of injector, which is charged with up to 8×10^{22} gaseous noble gas neutrals. It is installed as close as possible to the hot plasma periphery in order to deliver the atoms with low losses to the plasma. The major aim is to enhance the density and to reach the above-noted target density on a short timescale typical for disruptions. The density is measured by a CO_2 laser interferometer, which is equipped with two vertical lines of sight at one toroidal location. In order to investigate the impurity propagation and clarify the question whether they populate the plasma column uniformly - which is appreciable for an effective runaway suppression - we installed a new XUV multi-channel photometer for radiation tomography. This diagnostic system reveals complex radiative dynamics hitherto not been resolved in ASDEX Upgrade plasmas. Spectrally unfiltered AXUV detectors resolve microsecond processes and exhibit a continuous responsivity from hard X-rays to the near IR [17], [18]. This broadband responsivity is essential in order to follow the rapid spectral sweep performed by the disruptive plasma during the cooling down sequence. The broadbanded radiation spectrum acquired is an information carrier, which implies the physical parameters of the plasma diluted by the injected noble gas. The captured information is the combination of changes in density, temperature and states of ionisation or excitation, because the applied noble gases neon and argon are not fully stripped in the periphery of an ASDEX Upgrade plasma. For this work, I apply 144 lines of sight for radiation tomography and 32 additional channels for observing the radial penetration of the noble gas jet from above. The two channel subsets are toroidally spaced in a way that we gain knowledge about the toroidal propagation of impurities. We will identify a screening effect of the plasma and a retarded penetration of the impurities into the bulk plasma. Complex structures, which rotate around the torus are identified, a clear onset of strong dynamics in the plasma core is observed and locations of impurity amassment are depicted. Particular attention is also set to the diagnostic itself, because it provides a new kind of data in disruption sequences, which have hitherto been obscure.

[7] Bound and free electrons

The structure of the thesis:

First of all, subject related basics are introduced such as the magnetic topology of a tokamak plasma, the plasma dilution, radiation and magnetic mode formation. The subsequent chapter will introduce special issues of the disruption complexity. The chronology of events is traced followed by an overview of disruption consequences and load mitigation. In a further chapter, the diagnostics used for this thesis are introduced. The centre stage takes, in this context, the newly installed photometer. The subsequent chapter introduces the methods used for analysing the diagnostic data. Those methods are applied to experimental data, in order to assess the capabilities of the diagnostic. On this fundament, Chapter VI presents and discusses the experimental results of massive gas injection scenarios by focussing mainly on radiative processes. The subsequent summary and conclusion briefly reviews the gained knowledge, puts it into a context with the density measurements in [26] and closes finally with an outlook for the future experiments on ASDEX Upgrade.

Chapter II

Basics

The ensemble of collectively interacting charged particles in gaseous state is called a *plasma*. For the external observer, it usually appears as a neutral gas, because every ion charge is shielded by a negative potential from a surrounding electron sphere. Nevertheless, microfields appear in a plasma, which change the kinds of collisions with respect to the hard sphere impacts in a neutral gas. An additional significant plasma property is the response to externally applied electric and magnetic fields. Thus, the plasma motion is controllable by electric and magnetic fields - the neutrals motion not. A plasma emits electromagnetic radiation. The latter gives information about density, temperature, the species composition and the energy loss. The equilibrium and gross stability of a tokamak plasma is usually investigated using MHD (magneto hydrodynamics). It is a system of equations made up by Maxwell equations and gas dynamics and Newton's equation for a fluid element.

II.1 Plasma topology

The basic aim is to confine the plasma. In the toroidally symmetric tokamak setup, this is done by steering charged particles along magnetic field lines via the Lorentz force. If the magnetic field was purely toroidal, an extra drift force arises with a charge dependent sign. It results in a charge separation in vertical direction with the consequence of a vertical electric field. Crossed with the toroidal B, this electric field causes an $E \times B$ velocity and henceforth, a loss of the plasma on the timescale of milliseconds. The methodological approach is to reduce the drift by adding a poloidal field component. The superimposed magnetic fields form a helical field line structure. In a given helical field, the particle, which is guided along a field line, drifts away from the field line as long as it explores the region below the midplane - above the midplane, it is forced to come back to the field line. Therefore, the net displacement away from the field line is kept low. The additional poloidal field component necessary to generate helicity, is produced by a toroidal current.

Primarily, it is driven externally by a loop voltage[1].

Each field line covers a toroidal surface. All field lines together build up a nested topology of virtual tori, because the field lines do not cross each other. On the circumferential surfaces of those tori, the poloidal magnetic flux Ψ is constant. We call these surfaces 'magnetic flux surfaces'. They are labelled with q. On the left in Figure II.1, the flux surfaces are drawn in a cross-sectional view. On the right, a 3-D illustration shows two toroids.

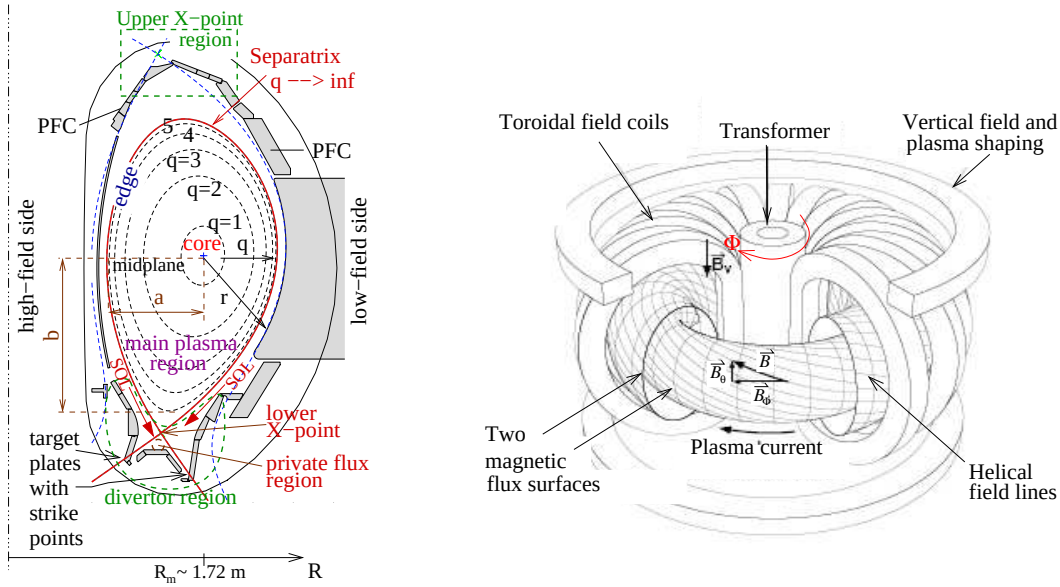

Figure II.1: Magnetic flux surfaces and coil setup of the tokamak. On the right, a schematic 3-D drawing illustrates the coil setup and helical traces of the field lines. The vectors of the toroidal and the poloidal magnetic fields B_Φ and B_Θ, respectively, are illustrated as a helical field B traced by the magnetic field lines. On the left, cross-sectional view of the magnetic topology. The $q-$label corresponds to Equation II.1. Some denotation: The SOL is the *'scrape-off layer'*, which is located in between plasma facing wall components (PFC) and *'separatrix'* (red line). The *'edge plasma'* is a radially narrowly constricted poloidal region inside the separatrix. The *'main plasma region'* is represented by closed flux surfaces (confined region). The *'core'* represents the plasma in the magnetic centre vicinity, basically inside $q = 2$.

The safety factor q is a measure for the helicity. It is the ratio between the toroidal and the poloidal turns of a field line until it joins in itself. It can be expressed as

$$q = \frac{\mathrm{d}\Phi}{\mathrm{d}\Psi} = \frac{1}{2\pi}\oint \frac{r}{R}\frac{B_\Phi}{B_\Theta}\,\mathrm{d}s, \tag{II.1}$$

[1] furthermore current sources arise from effects during neutral beam injection, electron cyclotron heating and due to neoclassical transport

where Φ and Ψ are the toroidal and poloidal magnetic fluxes through the respective surface and B_Φ and B_Θ are the toroidal and poloidal components of the magnetic field. The line integration is along a poloidal cross-section of the flux surface. For a circular cross-section and by substituting Ampère's law ($B_\Theta = 1/(2\pi r)\mu_0 I(r)$), Equation II.1 can be written as

$$q(r) \;=\; \frac{2\pi r^2 B_\Phi}{I(r)\mu_0 R} \tag{II.2}$$

The $q-$profile implies the current distribution $I(r)$. In the standard H-mode operational mode[2], which are considered in this thesis, temperature, conductivity and thus the current are peaked at the magnetic axis ($r = 0$). This implies that q decreases towards $r = 0$ ($q(r) \propto I(r)^{-1}$).

The $q-$parameter is called *safety factor*, because it is a kind of a measure how rigid the plasma reacts on current driven instabilities. A tokamak plasma was found to be stable, if in the centre $q > 1$ and in the edge $q > 2$ [10]. A rough estimate for the q profile can be deduced from q_0 and q_{95}, which is the q at the magnetic centre at $r = 0$ and the q close to the plasma boundary, respectively. The latter is defined as the q number of the magnetic flux surface, which encloses 95 % of Φ. Such a convention is necessary, because in diverted plasmas, the q of the plasma boundary, which is referred to as separatrix, goes infinite due to $B_\Theta \to 0$ (see Equation II.1).
The toroidal magnetic flux coordinate ρ_Φ is defined as

$$\rho_\Phi \;=\; \sqrt{\frac{\Phi \,-\, \Phi_0}{\Phi_{\mathrm{sep}} \,-\, \Phi_0}}, \tag{II.3}$$

where the flux on the magnetic axis is Φ_0 and the flux on the separatrix is Φ_{sep}. Analogously, the poloidal magnetic flux coordinate ρ_Θ is defined by using the poloidal flux functions Ψ, Ψ_0 and Ψ_{sep}.

The current j flows in the magnetic surface. Crossed with the magnetic field B, it counterbalances the expansion of the plasma as

$$\nabla p \;=\; \vec{j} \times \vec{B}, \tag{II.4}$$

The pressure gradient ∇p is perpendicular to $\vec{j}$ and $\vec{B}$. It follows $\vec{j} \cdot \nabla p = \vec{B} \cdot (\vec{j} \times \vec{B}) = 0$. The pressure gradient is always perpendicular to the magnetic flux surface and zero within the surface. The flux surfaces, which are shown on the left in Figure II.1, are determined on the basis of the force balance equation, which is referred to as Grad-Shafranov equation:

$$R\frac{\delta}{\delta R}\left(\frac{1}{R}\frac{\delta \Psi}{\delta R}\right) \;+\; \frac{\delta^2 \Psi}{\delta z^2} \;=\; \Delta^* \Psi \;=\; -2\,\mu_0\,\pi\,R\,j_\Phi \;=\; -\mu_0 (2\,\pi\,R)^2\,p'(\Psi) \;-\; \mu_0^2\,I_{\mathrm{z}}'(\Psi)\,I_{\mathrm{z}}(\Psi) \tag{II.5}$$

[2] H-mode is an abbreviation for high-confinement mode.

The solution of the non-linear Grad-Shafranov equation is approximated by measurement data interpretation. In this thesis, flux surface reconstructions were carried out partly with the CLISTE code (*C*omp*L*ete *I*nterpretive *S*ui*TE*) and with a function parametrisation code [9], [22].

II.2 Elongation and diversion

As shown on the left in Figure II.1, the magnetic flux topology is elongated vertically by shaping coils. An elongated plasma of a given q carries higher currents on the flux surfaces compared to circularly shaped plasmas. This is due to the increased poloidal circumference $s(\Theta)$ of an elongated plasma. Higher plasma currents allow the operation under higher densities[3] and this, in turn, allows for a higher plasma β, which is defined as $\beta = \langle p \rangle / (B^2/(2\mu_0))$, where $p = nkT$. The plasma β basically implies how many reactants are available for a fusion reaction and implies thus the performance of a future fusion reactor.

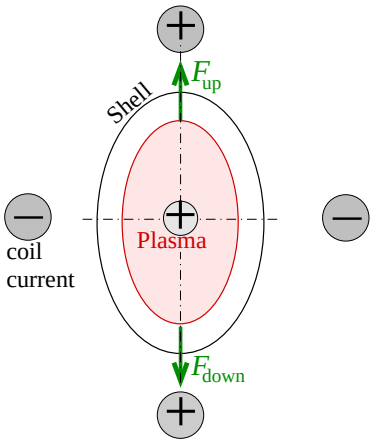

Figure II.2: Marginal vertical stability of elongated plasmas.

However, the benefits of elongation are accompanied by a significant disadvantage: Elongated plasmas are vertically unstable. The forces, F_{up} and F_{down}, apply to the plasma as depicted in the neighbouring Figure II.2. As long as the plasma is centred, $F_{up} = F_{down}$. Surrounding conductors such as the shell or copper loops, stabilise the plasma inductively. Additionally, small deviations from the centred position can be caught by the feedback controlled positioning system. But gross instabilities in disruptive plasmas often perform a vertical movement, which is too fast for being controllable and too strong for being avoided by surrounding conductors. Then, the plasma comes closer to one of the two coil currents. An accelerating force arises in the direction of displacement. The point where the force balance holds, constitutes a marginal stability - if violated, strong plasma-vessel interactions could arise. The consequences are described in Chapter III.

The diversion of the plasma boundary: The elongated magnetic flux topology, as shown in Figure II.1, is made up by the main plasma region and a narrow layer of open flux surfaces[4], which is referred to as *scrape-off layer* (SOL). The latter has a radial width of

[3] The empirically found density limit is treated again in Chapter III.

[4] The field lines of open flux surfaces are loosely denoted by *open* field lines, because they do not close inside the vessel but penetrate the chamber wall and close outside

only $\approx 1\,\mathrm{cm}$ around the midplane. The flux surface, which separates the two regions is called *separatrix*. Inside the separatrix, the plasma is confined (main plasma). Inevitable radial transport leads to a particle flux out of the main plasma into the SOL. There, the particles are transported down to targets (see Figure II.1, on the left, bottom). The plasma flow hits the tile at the strike point (strike line in 3-D)[5]. The arising heat load must be kept within the tolerable limits. The fact that the separatrix is diverted results in two strike points and a halved heat flux to the tiles. The high energy particles, which leave the confined region and enter the SOL travel the way down for a duration, which is in the order of milliseconds dependent on the B-parallel temperature gradient [60]. During this time, the particle interacts with the cold electrons in the SOL and kinetic energy is dissipated. In front of the targets, the temperature is only of a few eV. The divertor region constitutes a source of impurities due to relatively high heat loads on wall components [53]. But the principle of elongation and diversion allows for increasing the distance between the targets and the hot plasma region. The divertor decouples, so to speak, the 'dirty' from the 'clean' region. In Düchs, *et. al.* [52], goals and background of diverting the plasma are overviewed.

The plasma dilution: The magnetic topology makes it possible to create and sustain current, pressure, temperature and density profiles versus the minor radius r. All those profiles are peaked around $r \approx 0$. However, inevitable energy transport perpendicular to B limits the confinement capability of a tokamak. Friction perpendicular and parallel to B and anomalous transport[6] mechanisms lead to particle fluxes across magnetic flux surfaces. An unavoidable presence of impurities in addition to an impurity yield by plasma wall interaction leads to a dilution of the hydrogen plasma. For instance, carbon, oxygen or tungsten are relevant impurities. Nitrogen or noble gases are deliberately puffed into the plasma for controlled radiative cooling. The fractional abundances of the ion stages form radial shells along the flux surfaces, on which T_e is approximately constant. Each ion stage occupies a certain shell around the magnetic axis, where $T_\mathrm{e}/\,E_\mathrm{ion,z} \approx 1$. In case of a low-$Z$ impurity such as nitrogen, the innermost shell is relatively broad and extends deeply into the plasma interior, where it is populated by fully stripped ions. Contrarily, the edge of an H-mode plasma, which is characterised by a strong temperature gradient is populated by many ionisation stages due to charge exchange and radial transport. A steep gradient of the ionisation stage z is the result [5]. Also in the confined region, magnetic flux surfaces are populated with a composition of ionisation stages of several different impurity species due to the B-perpendicular transport mechanisms. Radiation from the confined plasma region is thus composed of various contributions from bremsstrahlung, recombination radiation or impurity line emission.

[5]The tile surface area affected by the heat flux is referred to as *wetted area*.

[6]The naming is due to the initial surprise that particles are not perfectly steerable along magnetic field lines.

II.3 Radiative loss factors

Electromagnetic radiation in a tokamak plasma covers a wide field from generation over absorption through to the issues of radiation transport. The latter allows for diagnosing atomic or molecular processes and includes the topic of plasma cooling or heating. With respect to the radiation measurements carried out in this thesis, radiation losses in an ASDEX Upgrade plasma are discussed by considering the implications of radiative loss parameters. The radiation parameter L and the radiative potential are subjects in the following.

In the radiation parameter L, radiative bound-bound, free-bound and free-free transitions are absorbed. The parameter adds the contributions from all charge stages assuming the corona ionisation equilibrium[7] at temperature T. A plasma, which consists of elements x, radiates with

$$P_{\mathrm{rad}} \;=\; n_{\mathrm{e}}^2 \sum^{x} f_{\mathrm{x}}\, L_{\mathrm{x}}, \tag{II.6}$$

where $f_{\mathrm{x}} = \frac{n_{\mathrm{x}}}{n_{\mathrm{e}}}$ for the element x and n_{e} stands for the electron density. For a fully ionised impurity, L is dominated by bremsstrahlung. For not fully stripped ions, line radiation is dominant.

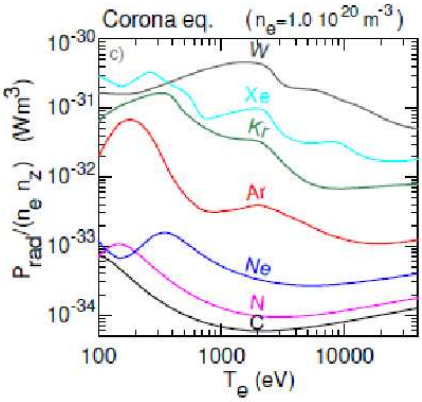

Figure II.3: Radiation parameter L in case of corona ionisation equilibrium. Figure courtesy by Dr. R. Dux.

The application of L is appropriate in the main plasma region, where the time scale for achieving the ionisation - recombination equilibrium is shorter than the particle residence time. The L parameter scales basically with z^3 [55], where z is the charge stage. The curves for several elements, where the corona ionisation stage is assumed for all charges stages, are plotted versus electron temperature T_{e} in Figure II.3. Tungsten radiation in the core has to be considered in the ASDEX Upgrade device, because its inner wall is fully lined with tungsten [101], from which an impurity source arises due to vaporisation or sputtering effects.

Impurity concentrations in the core plasma depend on the impurity production rate, the location of impurity production and the perpendicular and parallel transport coefficients [5]. The tolerable concentration of tungsten in the plasma core is $f_W = 10^{-4}$. At higher concentrations, the radiation losses come close to the input power, which violates the equilibrium conditions.

[7] Corona ionisation equilibrium means balance between electron impact ionisation and radiative and dielectronic recombination.

The radiative potential: The divertor and the edge of a tokamak plasma are characterised by a short particle residence time τ compared to the corona ionisation equilibration time. In such conditions, the radiative potential ansatz is used [56] instead of the corona model. It represents the energy a particle is radiating during the time τ, in which the neutral undergoes a stepwise collisional excitation and ionisation to higher charge stages. The resulting line radiation emitted is calculated using atomic data and a collisional-radiative model (for the plots in Figure II.3, the ADAS database is used [7]). Figure II.4 presents curves, which are evaluated on the basis of the radiative potential per atom for the product $n_e\tau = 0.1$ (left) and $n_e\tau = 10$ (right).

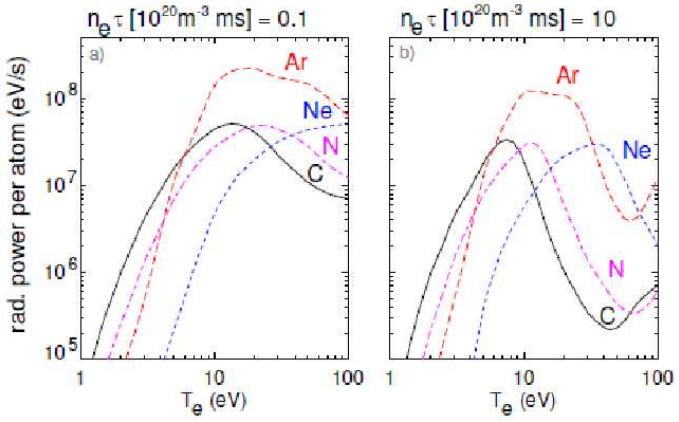

Figure II.4: Radiative factors based on the radiative potential ansatz [56]. The two cases differ in the residence time τ at a given electron density n_e: On the left, $n_e\tau = 0.1$, and $n_e\tau = 10$ on the right. The x-axis corresponds to edge and divertor temperatures in an ASDEX Upgrade plasma. Figure courtesy by Dr. R. Dux.

Keeping the electron density n_e constant and enhancing the residence time τ with a factor of 100, the radiation potentials change their behaviour correspondingly to the two diagrams shown in Figure II.4. The consequence is a reduced radiated power per atom in the case of a high τ (right hand side, Figure II.4), which comes closer to coronal ionisation equilibrium conditions. This radiation reduction applies in particular to electron temperatures ranging in between $T_e = 10...100\,\mathrm{eV}$. Generally, the deviation from the coronal ionisation equilibrium leads to enhanced radiative losses.

II.4 Current driven modes

Beginning with Ohm's law, which is expressed as

$$\eta j_{\parallel} = E_{\parallel} + v_{\perp} \times B, \tag{II.7}$$

where η is the resistivity, j stands for the current along the magnetic field line, $E_{\parallel}$ is the electric field parallel to B. If $\eta = 0$, $E_{\parallel}$ must be zero, which means that the magnetic flux is conserved. The consequence is that the topology can not change. If, however, resistivity applies and $E_{\parallel}$ arises, a velocity $v_{\perp}$ perpendicular to B evolves for matching Equation II.7. Henceforth, the plasma is steered away from the line of magnetic force. Neighbouring field lines are also deviated from their initial pathway, because in ideal MHD, field lines can not cross each other. A structure is formed, which we call a *magnetic mode*. Normally, this deviation is very small and becomes compensated but effects could occur, which constitute a drive for the mode growth. Large modes imply several negative effects like global confinement degradation or the formation of disruptive instabilities. While the topic of disruptions is delayed and thoroughly described in Chapter III, mode growing mechanisms shall be described here albeit it is referred to Rutherford [25] for consulting the details of the mathematical background, which actually would go beyond the intention of this subsection.

A tearing current is what we refer to as *tearing instability* with the consequence of a *tearing mode* (TM). Deviated field lines can reconnect and form locally closed field lines what we call *magnetic islands*. They consist of a separatrix, an X-point and closed flux surfaces as shown in Figure II.5 on the right.

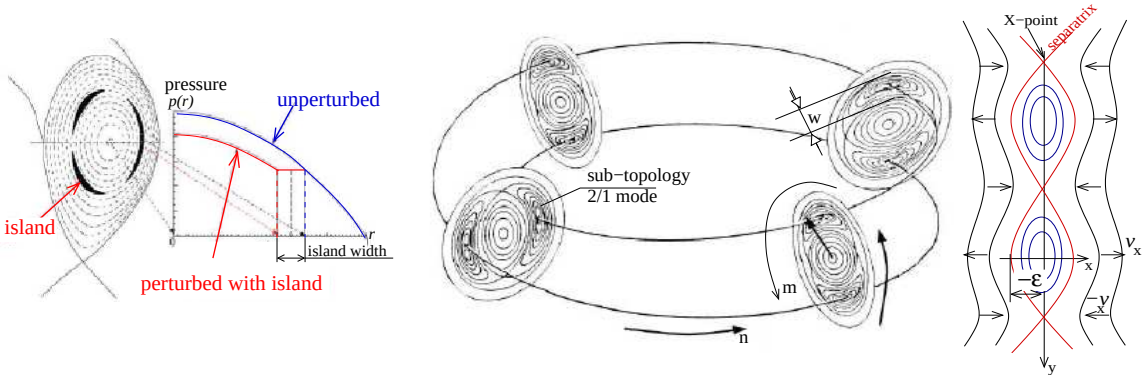

Figure II.5: Magnetic islands illustration. Left: An $m = 3$ chain of islands with the corresponding pressure profile modification (diagram). In the middle: An $m/n = 2/1$ magnetic mode with islands in 3-dimensional toroidal geometry. On the right, a scheme of a slab model: An island chain with closed flux surfaces (blue), the separatrix (red) and affected but not reconnected neighbouring field lines (black).

Regard the left hand side of Figure II.5: A chain of islands is formed (poloidal $m = 3$ number). In the interior, closed flux surfaces scan a certain r and shortcircuit therefore temperature and pressure, which leads to a reduction of those parameters in the plasma core. The pressure profiles for the cases with (red) and without (blue) island are shown in the diagram in Figure II.5. The global pressure reduction leads to a degradation of the overall confinement, which constitutes a limitation in β and simultaneously, a limitation in reactor performance. Very small islands do not show a pressure flattening and are, in this regard, not noteworthy. However, small islands constitute seed islands for a further growth. For considerations of growing mechanisms, the Δ' parameter is used. This meaningful parameter was introduced by Rutherford [25] and is commonly used in this field of research. It is given as the difference of derivatives of magnetic flux perturbation at $x = -\epsilon$ and $x = \epsilon$, with respect to the slab model in Figure II.5 on the right.

$$\Delta' \;=\; \frac{1}{\Psi}\left[\left.\frac{\mathrm{d}\Psi}{\mathrm{d}x}\right|_{x=\epsilon} \;-\; \left.\frac{\mathrm{d}\Psi}{\mathrm{d}x}\right|_{x=-\epsilon}\right] \tag{II.8}$$

In words: The Δ' parameter gives the free energy available for mode growing or shrinking. Switching from the slab to a cylindrical geometry, the point $x = 0$ becomes $q = m/n$, where m and n are the poloidal and toroidal mode numbers, respectively. The plasma equilibrium behaves - under the influence of a perturbed helical flux $\tilde{\Psi}$ - as given by the so-called tearing mode equation. It is expressed as

$$\Delta\tilde{\Psi} \;-\; \frac{\mu_0 \frac{\mathrm{d}j}{\mathrm{d}r}}{B_\Theta\,(1 - q\frac{n}{m})}\,\tilde{\Psi} \;= 0. \tag{II.9}$$

Equation II.9 implies that the perturbation $\Delta\Psi \to \infty$, if $m/n \to q$. Stability will crucially depend on the value of $\mathrm{d}j/\mathrm{d}r$ in the vicinity of a resonant surface. At irrational q, no resonant condition would apply. The mode would grow, if $\Delta' > 0$ and the threshold for the growth is exceeded[8]. The mode would shrink, if $\Delta' < 0$ and it would be stabilised, if $\Delta' = 0$. The value of Δ' is dependent on the (global) plasma equilibrium and hereby, significantly on the current profile. This actually implies recursive effects, because the mode modifies the global equilibrium. In disruption physics, we have to deal with low-m / low-n modes[9], which means 3/1, 3/2, 2/1 and even 1/1.

Ordinary tokamak equilibrium configurations provide $\Delta' < 0$. From this point of view, tearing modes are suppressed anyway. However, other effects, which are still under discussion, increase the Δ' parameter and modes can grow. The threshold for the growth is still obscure, but effects like turbulence or transport across the separatrix are suggested effects.

[8]This condition constitutes the classical picture of tearing mode growing.

[9]For large m, Δ' behaves as $\propto -m$, which constitutes a strong suppression for large m modes.

Chapter III

Plasma Disruptions

This chapter provides additional information on disruptions introduced in Chapter I. We briefly discuss disruptive instabilities, the disruption itself, the consequentially arising loads, the avoidance of plasma instabilities and the mitigation of the loads.

In the beginning, the disruption causes are introduced and an example[1] is shown. It exhibits several precursors, which constitutes a chain of events in the prehistory of a disruption. De Vries *et. al.* [62] have performed dedicated long-term work on this complexity on the JET tokamak. A detailled understanding of the chain of events is essential for disruption avoidance. We will progress through an example, in which an ASDEX Upgrade plasma performs a chain of precursors of diverse facets.

In following sections, the background and the consequences of the thermal and current quenches are considered. The last section is devoted to avoidance and mitigation of disruptions and the requirements on a rapid shut down scenario - a validation of massive gas injection (MGI).

III.1 Disruption causes and precursors

For clarity, we separate the two terms *cause* and *precursor*: A *'cause*' initiates a chain of instabilities that leads to a disruption. A *'precursor*' is this instability or it is another instability, which resulted from the first. Note, the cause is what a human mistake or a technical failure initiates by operating or influencing the plasma in a way that boundaries of MHD stability are exceeded. Henceforth, the cause is what we have to avoid, the precursor is the detectable quantity, which has to be recognised and, if possible, suppressed by a disruption intervention system. The wording *precursor occurrence* thus is dependent on the diagnostic ensemble in use. This exact denotation is the basis for the later consideration of avoidance and mitigation techniques. When reading the definitions of causes and

[1] Experiments are presented without going into diagnostic details for the time being. The information necessary for understanding the signals is integrated here - thorough details are situated in Chapter IV.

precursors as above, the disruption avoidance does not seem to be a dramatic problem, because the operator simply has to determine the discharge parameters such that they comply with the physical boundaries. However, physical boundaries are not necessarily fixed for the whole discharge duration but are complex functions of changing plasma parameters. Thus, criteria for stability can be violated although an instability-rigid scenario was initially applied. In conclusion, physics plays - in addition to the human mistake and technical failure - an important role in the context of causes and, moreover, it introduces a multitude of characters into the disruption complexity.

III.1.1 Operational space

Plasma operation is limited in parameter space: The electron density, the plasma current and the kinetic pressure. These are the well-known limits - if exceeded, an MHD instabilities arises. The symbols in the formulas: I_p is the plasma current, C is a factor which depends on plasma parameters, a is the minor radius, B stands for the toroidal magnetic field.

Electron density:	The so-called *Greenwald density* is empirically known to be a boundary, expressed as $n_\mathrm{GW} = I_\mathrm{p}(\mathrm{MA})/\pi\, a^2(\mathrm{m}^2)$ in $10^{20}\,\mathrm{m}^{-3}$
Current profile:	The q_{95} parameter must be > 2.
Pressure:	Limitation of the normalised volume-averaged toroidal beta, the *Troyon limit* $\beta_\mathrm{N}(\%) < C\, I_\mathrm{p}\,(\mathrm{MA})\, a^{-1}(\mathrm{m}^{-1})\, B^{-1}(\mathrm{T}^{-1})$

III.1.2 Causes and precursors

A process, which violates the above-listed operational limits is referred to as *cause*. Causes are e. g. tile fragments, which fall into the plasma and perturb the equilibrium. Other examples are inaccuracies of external field coil positioning and irregularities in the coil shapes and current feeds to the coils. Due to deviations from axisymmetry, error fields in the toroidal field arise, which can - if large enough - interact with the fields of magnetic islands in the plasma. The interaction can lead to a retardation of the magnetic island rotation or even to a complete stop. The latter is denoted by *'mode locking'*. A locked mode can also be produced actively by error field induced seed islands ([35] ... [38]). Figure III.1 shows a mode locking for a time duration of almost 10 ms, which ends up in a minor disruption. In the following, we will restrict the description of the multitude of precursors to an extent important for this work. This concerns the appearance of modes, of the MARFE and the minor disruption.

Magnetic modes are excited by exceeding one of the critical boundaries listed above. As explained in Chapter II, magnetic modes arise in the vicinity of rational flux surfaces of a low q. The growth rate of m/n=2/1, 3/1 or 3/2 modes is often of non-linear characteristic and large modes can initiate a rapid thermal energy expulsion in the form of a minor or a major disruption. The occurrence of a low-m, low-n magnetic mode is a disruption precursor. Modes can be detected and techniques are studied, in which ECRH heating is applied for controlling the mode growth [68].

Figure III.1 shows an occurrence of several modes in the low-q discharge[2] #24413. As a precursor for the first two minor disruptions, a changing mode activity is identified. In the first one, the mode amplitude grows, which could have caused an overlap of neighbouring modes. Stochastic variations of the pathways of magnetic field lines could possibly arise in such a condition, which leads to an enhanced radial transport and a loss of confinement. The second minor disruption was signalised by the slowly rotating $m/n = 3/1$ mode between 0 and 16 ms and its locking marked by the green cursor.

Mode locking is based on resistive MHD [39], [40]. The locked modes are resistive tearing modes in the vicinity of the rational surface $q = m/n$ [47]. A mode rotates toroidally due to a torque caused by superimposed effects such as diamagnetism or e. g. NBI momentum input. If the mode results in island formation and the island is of sufficient width to induce significant eddy currents in the surrounding conductors, an opposite torque retroacts on the rotation and reduces the plasma rotation [41]. This is a normal condition and applies generally. However, if the error field matches the mode in a way that it reduces the plasma rotation to a sufficient extent, an abrupt locking could occur. When the mode is locked, it ultimately grows and reduces the confinement due to the flattened pressure inside and the short-circuited internal temperature, which results in an efficient radial transport. An example for mode locking is presented in Figure III.1.

The uncontrolled MARFE, is known to be a precursor for density limit disruption [96]. It is a cold radiation condensation instability[3] appearing when the density limit in the edge is approached [50]. The threshold density scales linearly with the plasma current I_p . The MARFE appears as a toroidal structure. It is poloidally localised partly in the SOL and - in small parts - also within the confined plasma region [43]. The radiated energy is related to the temperature T_e, the impurity mix and the radiation potential of the relevant impurities. As presented in the previous chapter, Figure II.4 shows the radiation potential versus T_e for several elements. The functions presented on the right have a pronounced maximum. In regions with a negative derivative, a local temperature

[2]The purpose of the discharge (studies on X3-mode heating) is explained in [95]. The ECRH system is overviewed in [94].

[3]MARFE is the abbreviation for *M*ultifaceted *A*symmetric *R*adiation *F*rom the *E*dge

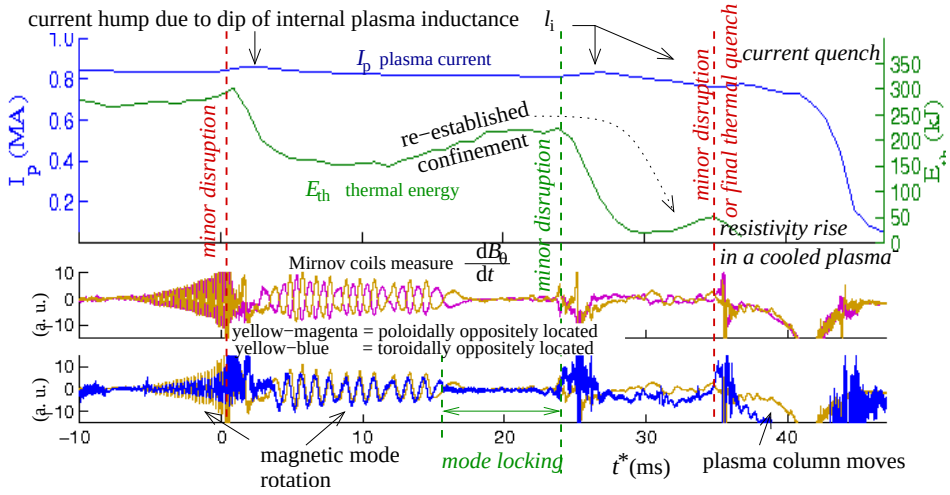

Figure III.1: Series of minor disruptions and mode locking (discharge #24413). Find the signal labels as attachments to the plots. The $x-$axis is zeroed at $t = 2.8932\,\mathrm{s}$ for making the time scale more feasible. Magnetic coils measure the change of the poloidal magnetic field in the vessel wall vicinity on the midplane [93].

decrease would lead to an increase of radiation losses - this corresponds to an instable condition. If the radiation loss cannot be compensated by heat conduction [60], the local volume becomes thermally unstable, grows or starts to move [49]. We call this condition an *uncontrolled MARFE regime* in this work. The cause of such a regime is an insufficient energy flux across the plasma boundary into the MARFE volume. If the other extremum is the case, namely a too high energy flux into the edge, then, the MARFE flushes out [43] and impurities are redistributed. A controlled MARFE regime establishes in cases of a well-balanced input/output condition meaning the core must be hot enough for providing the energy flux for stabilising the MARFE in the edge.

Minor disruptions are possible precursors of a major disruption. A minor disruption shows features comparable to the thermal quench. It differs from the thermal quench in the regard of the E_{th} expulsion: A minor disruption only removes a fraction - a thermal quench expels the full magnitude of E_{th}. A minor disruption in fact modifies density, pressure and current profiles but does not affect the plasma in such a way that it leads to a full expulsion of E_{th} and a subsequent current quenching. The discharge thus continues. In Figure III.1, a series of minor disruptions removes successively the thermal energy content E_{th} from the plasma with intermediate E_{th} rises. After the third minor disruption, however, the plasma is cooled such that the current quenches. This quench is the major disruption.

A minor disruption is a precursor to a major disruption, because it could affect the density, pressure and current profiles such that boundaries are exceeded.

III.1.3 The chain of events

An essential issue for an effective application of avoidance techniques is the information about the primary cause of the chain of events and how the source of instabilities is eliminable. Figure III.2 is devoted to the complexity of the chain of events, which finally results in a disruption. On the left hand side, the complete discharge #24428 is shown.

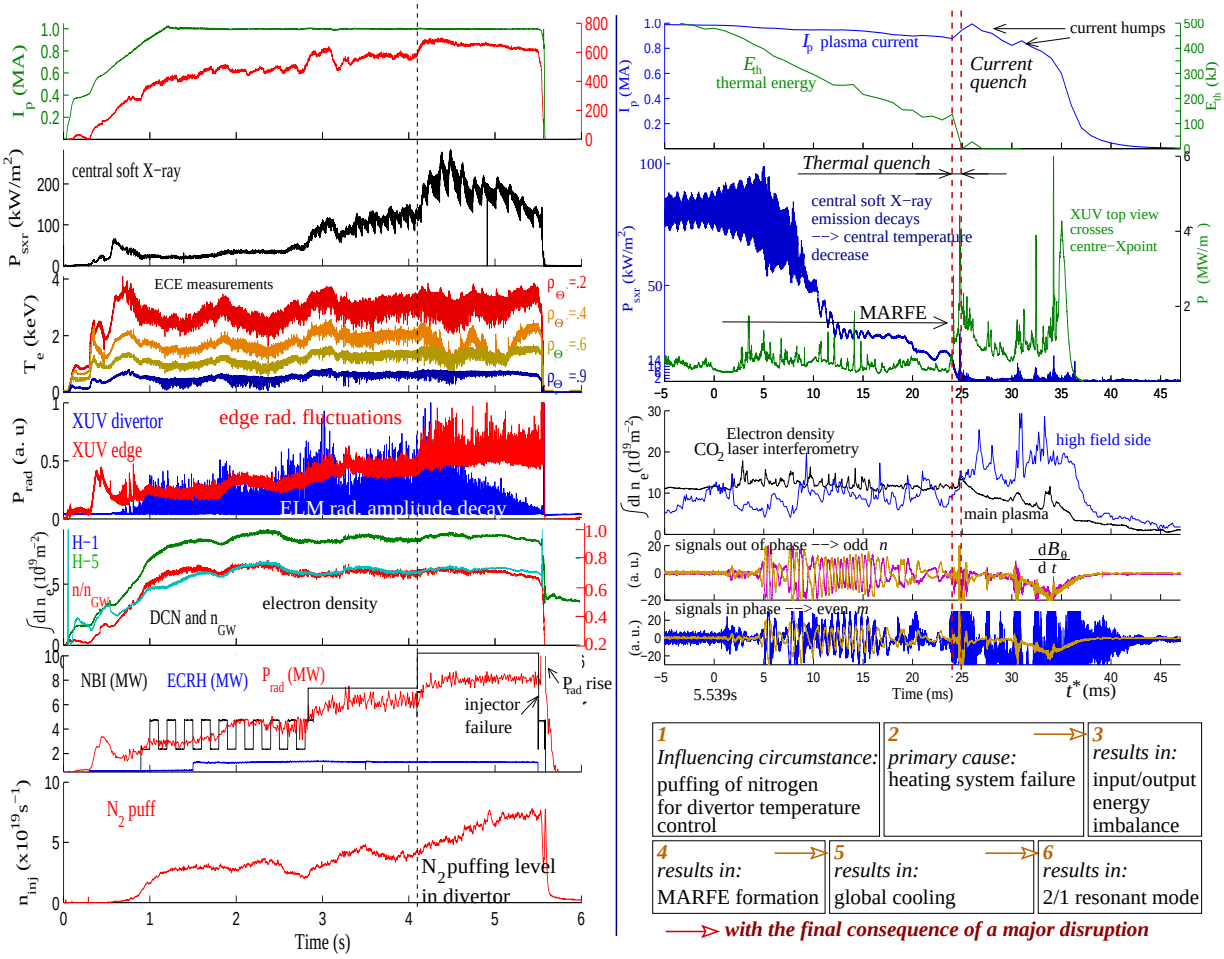

Figure III.2: Chain of events in an edge cooling disruption. Find the signal labels as attachments to the plots. DCN laser interferometry [91] crosses the main plasma - the CO_2 interferometer [92] views the high-field side as well as the main plasma, given as $\int \mathrm{d}l\, n_\mathrm{e}$, where l is the length of the line of sight. (n_GW see Section III.1.1.

On the right, the disruption is zoomed. We will consider first the precursor activity and will then go backwards in time as far as necessary to trace the full chain of events: The growth of an $m/n = 2/1$ resonant mode leads to a disruption clearly featured by the Mirnov coils in the right part of Figure III.2. The red cursors temporally demarcate the thermal quench. The resonant mode was excited by a steepened current gradient, which is deducible from a risen inner plasma inductance l_i (not shown in Figure III.2). Such

a rise of l_i is known in scenarios, in which extensive edge cooling leads to an increased resistivity in the edge. And this is indeed the case here: A MARFE, which resides in the divertor, enters the uncontrolled regime and starts to move at 5.539 s upwards along the inner heat shield. Before this time ($t = 5.539\,\mathrm{s}$, or $t^* = 0\,\mathrm{s}$), the stabilised regime in the divertor was made up by balanced energy fluxes (see Paragraph III.1.2) for several seconds. The regime changes from a controlled to an uncontrolled MARFE if energy fluxes become imbalanced as described above. In the considered case, the reduction of the energy conducted down into the MARFE region was caused by a failure of one of the neutral beam injectors (NBI heating system). The NBI failure finally constitutes the primary disruption cause.

The chain of events in #24428 is supported by an influence from the human side: The plasma was actively cooled for the whole discharge duration by a feedback controlled moderate puffing of nitrogen in order to retain the divertor temperature at the predefined level. This initiated the controlled MARFE regime from which we benefited with low divertor temperatures.

This example clearly demonstrates that *a precursor phase originates from an unfavourable interplay of effects attributable to technical, human and physical influences*.

III.2 Sudden loss of thermal energy: The thermal quench

Minor and major disruptions imply a thermal quench, which is a rapid cooling of the plasma. A possible mechanism for the sudden thermal energy expulsion is e. g. a field line stochastisation in case of neighbouring tearing modes, which are located close to each other. Magnetic reconnection in plasma areas of different helicity can occur.

Examples for thermal quenches were shown above in Figure III.2 and Figure III.1. Regarding the diagnostic signals in general, the thermal quench is characterised by a collapse of both the E_th content and the central soft X-ray emission (Figure III.2). A change of the internal inductance l_i (not shown in the figures) indicates a current redistribution. The result is a current hump in order to sustain the magnetic energy E_mag ($\propto I_\mathrm{p}^2$). These humps are marked in both figures. Central soft X-rays and magnetic measurements such as the Mirnov coil signals are perturbed by fluctuations, which could be attributed to magnetic stochastisation or reconnection effects. These fluctuations are not clearly depicted by the referred figures but they are used in more precise elaborations on MGI, where they constitute the most important indicator for the thermal quench onset. We will also see in many graphs throughout this work that the radiation losses can be very high, which depends on the impurity content during the disruption. In cases of low initial impurity concentration, the thermal quench is characterised by low radiation magnitudes,

whereas the current quench is accompanied by high radiation levels.

The crucial issue of the thermal quench is the energy expulsion from the main plasma, which is typically conducted along the narrow SOL and hit the target plates. Thermal energy is therefore deposited in a rather restricted area, the so-called *wetted area*. The size of the wetted area scales with the machine radius R and the radial decay length λ_{SOL}. Comparing ITER and JET, the surface area ratio is of 2.2. But the problem arises from the ratio of E_{th} contents of plasmas in ITER and JET: An ITER plasma will store 30 times more E_{th} than a plasma in JET. This is why we fear thermal energy conduction along the SOL in ITER, because the higher energy flux density exceeds possibly the load limits of the targets. This measure, however, is still obscure: The scaling of λ_{SOL} during the thermal quench, the wetted area, the vapour sheath formation in front of the targets, the remaining E_{th} content at the thermal quench, etc. are up to date not reliably scaleable to disruption scenarios in ITER.

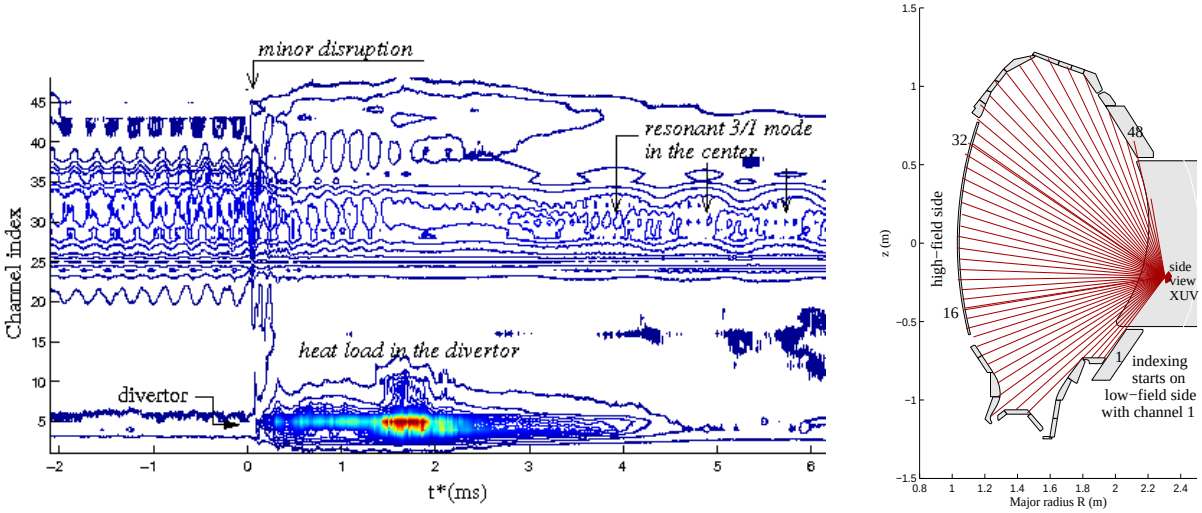

Figure III.3: Thermal energy expulsion during the thermal quench of a minor disruption (#24413, first minor disruption in Figure III.1, $t^* = 0$ @ $t = 2.8932\,\mathrm{s}$, same time axis as in Figure III.1). The *XUV* photometer views the plasma from the side with 48 pinhole lines of sight. On the left, signals are presented versus time in form of a contour. The y-axis implies the channel indeces, which are illustrated on the right hand side. Thorough details on the photometer in Chapter IV.

Figure III.3 shows signals of the *XUV* photometer, which is explained in Chapter IV in detail. Here, the energy deposition in the divertor after the occurrence of a minor disruption is shown: In the centre, modes interact with each other, which leads to a minor disruption (marked). Energy is dissipated in the core plasma and conducted down to the divertor, where the heat pulse arrives. The latter is featured by the rising signals in channels, which view the divertor (4-7).

III.3 Current quench

The current quench follows the thermal quench. The current decreases from the order of MA down to zero within a few milliseconds due to the resistivity rise in a cooled plasma ($\eta \propto T^{(-3/2)}$) . The resultant ohmic reheating does not return to the plasma, but is radiated away by the impurities. The poloidal magnetic energy, which can be calculated by

$$E_{\mathrm{mag}} \;=\; 0.5\, I_{\mathrm{p}}^2\, \mu\, R \ln\left(\frac{8R}{a\sqrt{\kappa}} \;-\; 2 \;+\; \frac{l_{\mathrm{i}}}{2}\right) \tag{III.1}$$

is dissipated basically via radiation. (The symbols: The major plasma radius R, the minor radius on the midplane a, the internal inductance l_{i}, and the elongation $\kappa = b/a$, see Figure II.1.) The rapid change of the poloidal magnetic flux induces electrical currents in surrounding conductors, which in turn generates EM stresses in the wall material. The poloidally elongated plasma is affected by an $m = 1$ instability, which implies a strong vertical position instability. The plasma column is displaced on a time scale equivalent to the time scale of the current decay in passively stabilising structures in the plasma surrounding. If the loss of vertical control comes about through the rapid changes of l_{i}, β, etc. in the thermal quench, we speak about a thermal quench initiated vertical displacement [51]. But VDEs can also have other kinds of causes: The VDE possibly originates from technical failures in position control or saturated control coils. A destabilisation could also originate from a very large ELM[4]. Due to the fact that the position stability point of an elongated plasma is of marginal characteristic, large perturbations can lead to a vertical motion of the plasma column, which is accompanied by an induction of electromagnetic forces in the surrounding conductors.

If the plasma displacement is large such that it touches the wall, the SOL field lines intersect the surrounding shell and poloidal currents flow through the material. These currents are referred to as halo currents ([45], [44]). The halo current crossed with B_Φ give rise to vertical electromagnetic forces [46], [45].
The global magnitude of the vertical force [29] is estimated to

$$F_{\mathrm{Z,max}} \;=\; 0.7\, I_0\, \Delta Z_{\mathrm{max}}\, \frac{\delta B_{\mathrm{r,eq}}(\Delta Z_{\mathrm{max}})}{\delta Z} \tag{III.2}$$

where I_0 is the predisruption or pre-VDE plasma current, $\delta B_{\mathrm{r,eq}}/\delta Z$ is the radial equilibrium field gradient evaluated at the location ΔZ_{max}, which stands for the maximal plasma column displacement. An essential feature is that the current, which is still carried by the plasma at Z_{max}, is of the magnitude of $2/3 \cdot I_0$ implicated by the factor 0.7 in Equation III.2. In an ITER plasma of $I_0 = 21\,\mathrm{MA}$, this would result in 150 MN, or 15000 t. Aside from the electromagnetic forces, which arise due to the halo currents, the wall is

[4]The so-called ELMs are edge localised modes [54].

additionally loaded by heat flux due to the direct attachment. Gas injection during the disruption reduces both the force according to Equation III.2 as well as the heat load [27].

III.4 Disruption interventions: Prediction, avoidance, mitigation

Regarding the operation in ITER, it is mandatory to avoid disruptions, because they reduce the lifetime of ITER and potentially - in the worst case - cause severe damage to internal components (runaway-caused water leak in the Tore Supra tokamak, R. Nygren, *et. al.* [83]). Time and money consuming shut downs, repair work and reconditioning phases could be the consequence. The need for a well-established disruption avoidance/mitigation system is undisputed. The section above showed the big drawback that the causes of disruptions do not come about by human mistakes or technical failures in each of the cases even though the operational boundaries are predictable in a particular discharge scenario.

III.4.1 Overview

Disruption avoidance starts with the determination of discharge parameters to guarantee a safe operation. A safe discharge is rigid against MHD instability onset, it guarantees vertical stability, a controlled impurity content, etc. During an ongoing discharge, *avoidance* means a feedback controlled counteraction against instabilities that are known as disruption precursors. This presupposes a technique for recognising this instability, which demands on a well-established diagnostic equipment and analysis. For instance, current profile reconstruction by the MSE diagnostic (Motional Stark Effect) [22], [90]. If, despite of any counteraction, the precursor grew or other precursors developed, the safety system has to decide for terminating the discharge before the hazardous major disruption occurs.

A disruption intervention or safety system, which provides for prediction, recognition, counteraction, decision-making and termination is not available yet. In Figure III.4, a possible run of a disruption is sketched from recognising over counteracting through to the decision-making process. Prediction of instabilities bases e. g. on neural networks which analyse data by applying the method of Self Organisation Maps (SOM) [65]. The principles of neural networks have been tested in [61] and [63], where the approaches reached relatively high success rates. In [64], the predictor system was directly applied to experiments and triggered a pellet injector for terminating the discharge with the so-called 'killer pellets'. Precursor prediction in the prehistory of high-β disruptions were performed in [66]. With respect to avoidance, several approaches are currently undertaken: Resonant mode stabilisation by ECRH heating on the $q = 2$ surface in [67] and [68], or

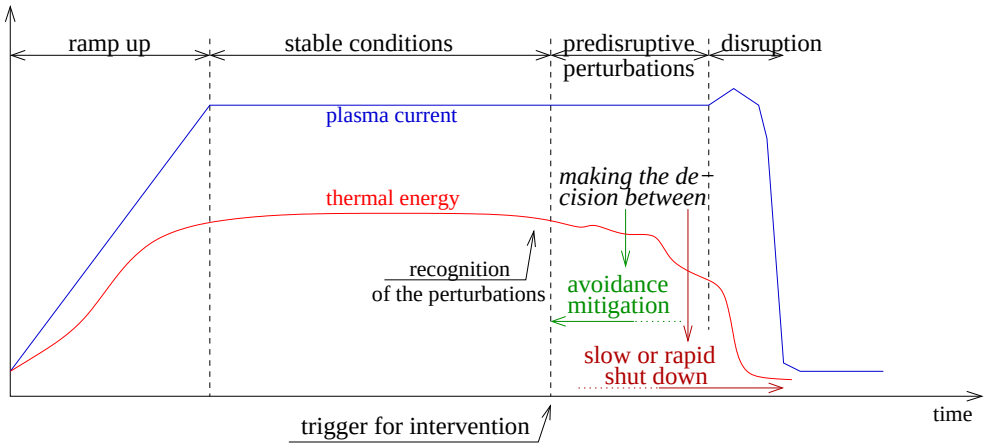

Figure III.4: Schematic illustration of a disruption: In red, the thermal energy is sketched, in blue, a typical trace of the current is drawn.

MHD instability suppression on the $q = 3$ surface in [69]. The approaches for mitigating the loads caused by disruptions base on the increase of the fraction of radiatively dissipated energy and an in turn decrease of conducted heat deposition. Under discussion is the use of liquid impurity jets [73], laser-ablated high-Z material [74], injection of cryogenous pellets [72] and gaseous jets [27]. Runaway steering approaches are undertaken on the principle of confining the beam in the toroidal magnetic field [84]. In [85], the opposite is intended: Externally induced magnetic ripples on B_Φ for avoiding the beam formation in order to lose the runaways in an early stage for reducing an avalanching. Fuelling techniques for enhancing the density in order to suppress runaways by collisions are covered by MGI experiments, e. g. in ASDEX Upgrade [28], [26], in Alcator C-Mod and DIII-D [32], [31] and JET [33].

The previously performed studies lead to the following preliminary conclusion: It might be impossible to operate ITER in disruption-free scenarios, because it must be assumed that prediction, recognition and counteraction methods will have a certain failure rate and therefore, a technique for mitigating the loads arising from disruptions has to be available. Gas injection proved in many experiments to reduce wall loads significantly, which promises to be a proper technique for load mitigation in ITER disruptions. On the contrary, runaway avoidance and suppression is still, in some regards, obscure: For instance, it is experimentally observed that some tokamaks are not affected by runaway population in disruptions. The origin for this phenomenon is supposed to come about by the differences in B_Φ, the plasma shapes or the various time scales of disruptions. Also the vertical position stability influences the runaway population because in non-diverted circular plasmas, which are very rigid against a displacement, runaway occurrence is much more frequent [86] than in diverted elongated plasmas like Alcator C-Mod or ASDEX

Upgrade, where runaways are hardly observed or even absent in disruptions.

Massive gas injection for an abrupt density buildup is a promising technique for suppressing runaways in ITER [29]. It is simple to inject gas - in contrast to other ideas, which were mentioned above. But on the other hand, open questions are whether the heat protectors in the surrounding of the nozzle could survive the radiative wall load or how the impurities propagate, whether condensed structures are formed or impurities are backscattered. And in fact, limited fuelling efficiencies are indicated in [26]. This thesis is dedicated to shed new light on the mixing behaviour during the shut down.

III.4.2 Gas injection for mitigating thermal loads

The SOL, which is of radial extension in the order of $\approx 1\,\mathrm{cm}$ on the midplane, leads the heat flux to the target. One can reduce the heat flux by using two divertors. Furthermore, magnetic field lines in the vicinity of the target can be tilted up to a certain extent. Nevertheless, a plasma in a 1.5 GW fusion power reactor delivers 30-100MW/m^2 to the targets, which is too large for being handled by conventional materials and cooling technologies [59]. Radiation could abate the problem by distributing the power uniformly over the first wall.

III.4.3 Gas injection for mitigating mechanical loads

The mitigation of mechanical loads in ASDEX Upgrade is thoroughly documented in [34]. It is proven that even moderate gas injection (0.18 bar l) lowers the vertical forces to even less than 50 % compared to unmitigated disruptions. In massive gas injection experiments (up to 3.3 bar l), the forces could be further reduced down to magnitudes typical for the preprogrammed ramp-up and ramp-down scenarios. The difference between unmitigated and mitigated disruptions is the extension of the plasma movement.

III.4.4 Massive gas injection for runaway suppression

Runaway electrons can be present in a tokamak plasma due to several reasons. The Dreicer effect [87] or, for instance, the hot-tail mechanism based on a non-perfect thermalization of the electron velocity distribution [88] are possible source mechanisms. Tokamak plasmas are populated with a certain amount of suprathermal electrons in the hot tail of the Maxwell velocity distribution. An additional source for suprathermal electrons is given in a DT plasma in ITER, where - in contradiction to currently operating tokamaks - the Compton effect [89] related energy transfer between gamma rays and electrons is of significance. However, if the friction force on the electrons is sufficiently large, runaway evolution is suppressed (due to a high electron density). However, in a disruptive plasma, a density rise is not mandatorily the case but far more important in this context is the

current profile change, from which an electric field E_Φ in the order of several tens of V/m arises. The accelerating force eE_Φ counteracts against the friction force F_f on the electrons. The latter reads as

$$F_\mathrm{f} = \frac{e^4\, n_\mathrm{c} \ln\Lambda}{4\pi\varepsilon_0^2\, m_\mathrm{e} v^2}\left(1 + \frac{Z_\mathrm{eff}+1}{\gamma}\right), \tag{III.3}$$

with $\gamma = 1/\sqrt{1-v^2/c^2}$. The speed of light is denoted by c, the electron velocity is v, the Coulomb logarithm is symbolised by $\ln\Lambda$ and Z_eff is the effective charge. A so-called critical density n_c, which is the minimum electron density at which electrons are prevented from running away is expressed as

$$n_\mathrm{c} = \frac{4\,\pi\varepsilon_0^2\, m_\mathrm{e} c^2}{e^3 \ln\Lambda} = 1.961\times 10^{22}\,\frac{\mathrm{E}}{\ln\Lambda} \tag{III.4}$$

As suggested in [80], relativistic electrons interact not only with free but also with bound electrons. The ratio of the collisional cross-sections amounts to $\sigma_\mathrm{e,bound}/\sigma_\mathrm{e,free} \approx 0.5$. The electric field in an ITER disruption is predicted in [26] as 38 V/m and the resulting n_c is estimated to about $4.1\times10^{22}\mathrm{m}^{-3}$. If the electric field rises such that the friction force is exceeded, the electrons accelerate and accumulate relativistic energies. This is the Dreicer effect. The higher the kinetic energy of the electron, the lower becomes the dragging force and the electron runs away.

In a disruption, seed runaways are produced by the Dreicer effect during the current profile redistribution. Those seed runaways push additional electrons into either the suprathermal or relativistic energy regime. It can lead to a multiplying avalanche yield, which is related to the time of the current quench. It will last tens of milliseconds in ITER, which gives rise to an intensive avalanching. The current quench duration is much longer than known from presently operating tokamaks and therefore, the ITER disruption places new challenges with respect to runaway suppression. The density increase to n_c for rising the friction force to magnitudes where the new-born runaways are instantaneously decelerated without leading to a significant avalanching is referred to as *collisional runaway suppression*. Experiments presented in this thesis perform first attempts towards n_c, albeit, as mentioned in Section III.4.1, investigations on runaways characteristics itself can not be performed in ASDEX Upgrade, because the disruptions are not significantly populated with runaways.

III.4.5 Desired and performed plasma shut down scenarios

In MGI experiments, gaseous noble gas particles are injected up to 80 times the nominal particle content. The injection lasts in between 2 and 3 ms, which is in the order of the precooling time before the thermal quench. The massive injection triggers a discharge termination, which is disruption-like: The fluctuating soft X-ray and Mirnov signals are observed during the decrease of the thermal energy, which hints at stochastisation or reconnection processes constituting the thermal quench. With a slight delay, the current hump arises actually within the thermal quench phase. Thermal energy and current decrease simultaneously, which means that the two phases, namely the thermal quench and the current quench, overlap in time. This is a fundamental difference to disruptions without gas puff, where they are clearly separated from each other. In later presentations of MGI shut down scenarios, this overlap is clearly depicted. Figure III.5 shows the way how we execute MGI: We do not react on an ongoing disruption but inject the gas into plasmas of well defined conditions. We use standard H-mode scenarios[5], in order to achieve a best possible degree of reproducibility, which is essential for comparing the effects arising from changing the jet parameters. The sequences of disruptive instabilities is therefore bypassed in the scheme. In the experiment, this is realised by a preprogrammed triggering of the MGI valve.

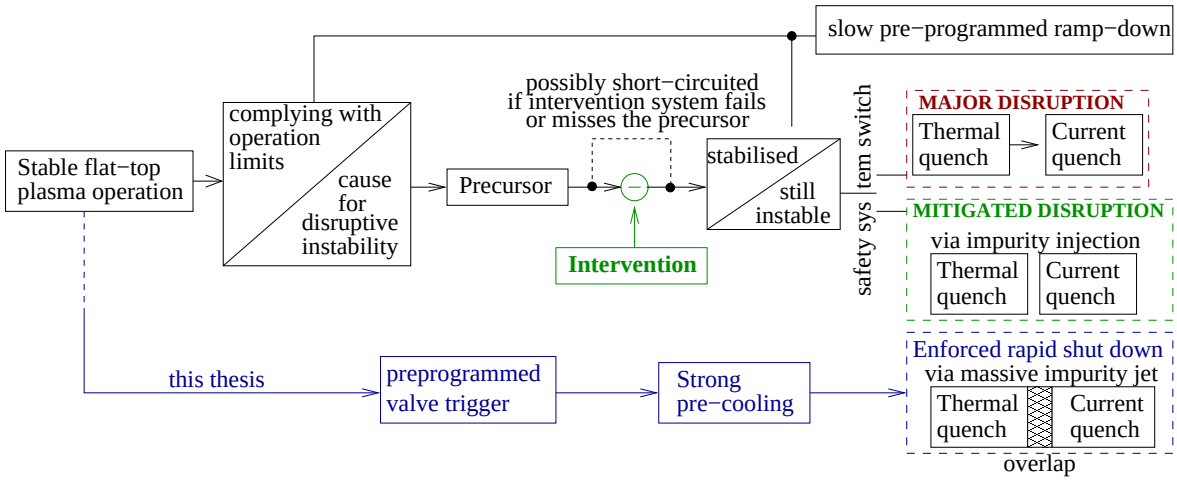

Figure III.5: The scheme of executing MGI experiments (lower path, concerns experiments in this thesis) compared to the disruptive scenario (middle path) and the desired scenario (upper path). MGI does not mitigate an ongoing disruption but terminates a stable discharge.

Current ramp down rates of shut down scenarios for stable discharges in ITER will be in the order of 0.5-1 MA/s [57]. In this thesis, MGI quenched the plasma current with

[5]High confinement operational mode.

rates of up to 250 MA/s, which implies that a 1 MA pulse can be terminated within 4 ms. The used sorts of gases, the plasma and impurity jet parameters are listed in Table VI.1.

Chapter IV

Experimental Setup

Tools are described, which are important for this work. The full experimental setup is the tokamak itself, which can be overviewed in [6].

IV.1 Disruption mitigation valves

Figure IV.1 shows both the setup of the distant valve for disruption mitigation as well as the newly installed MGI valve. The earlier is part of the safety system (middle path in Figure III.5), the latter is triggered in dedicated discharges (lower path in Figure III.5). Both valves are installed at the toroidal angle $\Phi = 0$. In what follows, this angle is to be defined the origin, because the toroidal transport of the impurities starts here.

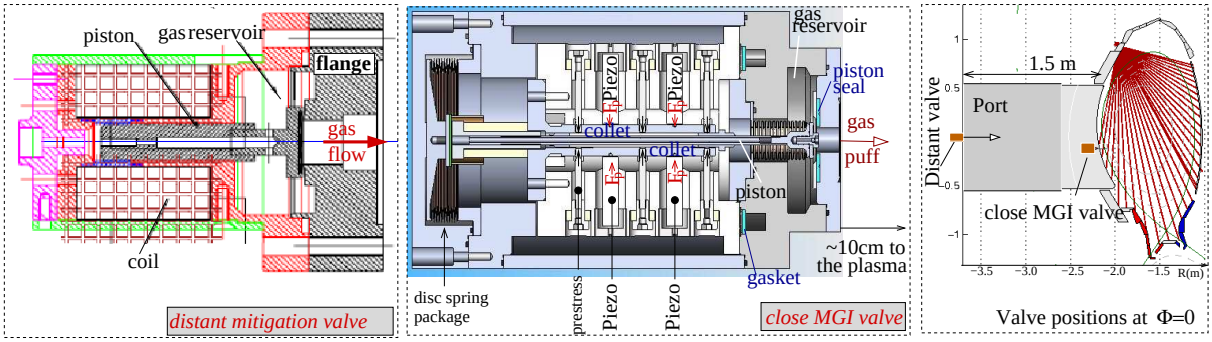

Figure IV.1: Valves for disruption mitigation. On the left, the distant mitigation valve (electromagnetic opening principle), middle, the MGI valve for massive gas injection (piezo driven piston) and on the right, an scheme of the positioning.

The distant valve for disruption mitigation is mounted onto the port flange (on the left in Figure IV.1). It can be triggered by the $n = 1$ mode detector system [48] by a hardwired connection. The latter implies an absence of intermediate processes, which would cause a delay between recognition and triggering. The piston is pushed back by an electromagnetic opening mechanism. In order to avoid an unintentional opening of the valve by magnetic fields, it is not allowed to apply it close to the plasma. The pressure in the valve reservoir is usually determined to 0.1 MPa. The injected volume amounts to 32 cm^3, the distance to the plasma edge is of about 1.5 m and the opening time lasts roughly 1 ms (opening time $\triangleq$ latency time of the mechanical components in the valve setup + time of flight of the impurities to the plasma periphery).

The MGI valve was installed in 2007 [28]. It is situated close to the plasma edge at $\Phi = 0$. The distance between plasma edge and nozzle depends on the plasma position and was of 13 cm in average in those discharges included in this thesis. This valve constitutes the closest injector for disruption mitigation ever used in a tokamak. A short opening time of down to only 230 μs, a large orifice of 14 mm diameter and low leakage ($< 10^{-19}$ mbar l/s) are noteworthy properties. The charging pressure is of up to 5 MPa, which is 50 times larger with respect to the distant valve. The functional principle of the closing/opening mechanism relies on piezo-actuators, which hold/release a central collet. This technique makes an application nearby the plasma possible, because the piezos are unaffected by the magnetic fields. Note that this constitutes the outstanding property compared to the distant valve.
Figure IV.1, middle: The piston, which is guided through the hollow collet is fixed when the piezo-actuators are set under voltage. When the voltage is discharged, the piston jumps back pushed by the prestressed disc spring package and the gas is released.

The two valves in comparison:

The impurities released from the distant valve, which is installed far back in the port, will first fill the port before they approach the plasma edge. Practically, the plasma will be affected by the approaching impurities on the whole outer midplane region on the low-field side. In contrast, the MGI valve delivers the atoms in a narrow Mach cone and generates a spot-like interaction zone at the beginning of the shut down scenario. The difference of the plasma response and its consequences are shown in Chapter VI.

IV.2 Radiation metrology

IV.2.1 Overview of the 3-D setup

Figure IV.2 presents an in-vessel drawing of ASDEX Upgrade in 3-D and a top view sketch. It gives a spatial impression of the positioning of the valves and diagnostics used in this thesis.

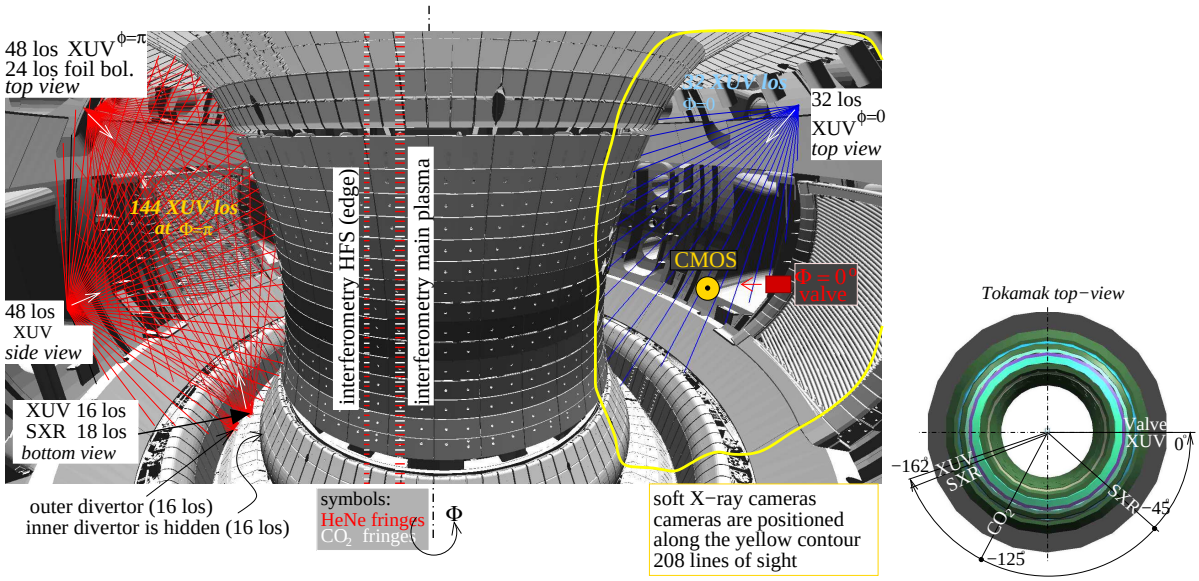

Figure IV.2: Schematic view of diagnostic geometries. Left: In-vessel view with diagnostic positions. Right: Top view with the toroidal angle dimensioning. The abbreviation *los* stand for *line of sight*.

IV.2.2 Resistive foil bolometry for absolute radiation measurement

The detector of the bolometer is a gold foil acting as a radiation absorber. The basic measurement principle relies on the temperature change of the absorber by irradiation [19]. The foil is attached in a self-supporting construction in order to keep the thermal connection to the other components low. Basically, the heat conductivity of the substrate as well as the capacity of the gold foils determine the time resolution. The latter depends on the absorber thickness. Meander lines of copper are lithographically patterned on the back surface of the absorber foils. The resistance change of those meanders is measured by a Wheatstone bridge, which compares exposed with unexposed detectors (the latter are masked). The signal conversion from the imbalanced measuring bridge to incident

power is given in [58]. Basically, it follows the principle expressed as

$$E = \frac{C}{\tau}\int U\,\mathrm{d}t + C\,U, \quad \text{with the time derivative} \quad P = \frac{C}{\tau}U + C\frac{\mathrm{d}U}{\mathrm{d}t}, \qquad \text{(IV.1)}$$

in which the measuring voltage and the device dependent constant are denoted by U and C, respectively.

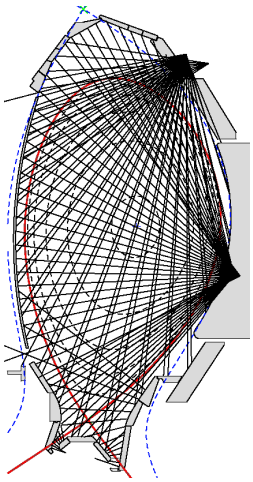

Figure IV.3: Foil bolometry. LOS at $\Phi = \pi$.

The temperature decays with a time constant τ of typically 100 ms. With the presently applied bolometers, detectable photon energies range from ≈1 eV to 8 keV, which corresponds to the emissivity range of an ASDEX Upgrade plasma. The bolometer detectors differ basically from semi-conductor detectors (XUV and soft X-ray diagnostics, presented below) in terms of accumulating the incident photon energy. A temperature change is generated if the photon enters the foil. In contrast, the semiconductor only detects the photon, if a charge carrier is produced by the incidence. In the earlier case, the restricting physical effect is reflectance - in the latter, the restriction of detection is related to semiconductor and interface physics. Some aspects are summarised in Section IV.2.3.

With respect to disruption radiation measurement, the following issues are remarked:

- The MGI induced rapid increase of neutral pressure implies a potential error source, because if the foils are bent, they would act like a strain gauge.

- Due to only one toroidal diagnostic position, the foil bolometry does not take toroidal radiation asymmetries into account, which are in particular of large significance in MGI.

- The restriction to 5 to 10 ms time resolution - basically determined by a relative high noise level - prevents from using the bolometer for the radiation power evaluation in the thermal quench of a disruption. In most cases, the energy quenching itself lasts in the order of 1 ms.

Though foil bolometry is affected by these above-listed disadvantages, it is used to a certain extent in this thesis. The principle of application is described in Chapter V.

IV.2.3 Novel XUV multi-channel photometer

The diagnostic was set up in the framework of this thesis. It is based on AXUV diodes. The acronym stands for *A*bsolute measurement in the e*X*treme *U*ltra*V*iolet spectral region. The manufacturing company is *International Radiation Detectors, Inc.* (IRD) in Torrance/USA [11]. The detectors mainly are applied in lithography devices [16]. In this work, the diagnostic acronym XUV is used concerning the outstanding property of UV and XUV light detection albeit the A is omitted. That is because an $\underline{A}$ bsolute radiation measurement is not possible in the wide range of photon energies emitted by the rapidly cooled, disruptive plasma. However, this thesis especially focuses on the radiative phenomena, which are by far not restricted to a spectral band. This is evident, firstly from the very fact that different sorts of mitigation gas are used, which exhibit different radiation efficiencies in, again, different photon energy regions. Secondly, the fact that argon and neon are used implies also the requirement of a spectrally broadbanded detector sensitivity, because those species are radiators at high as well as low temperatures.

This subsection is structured as follows: Firstly, the issues of the AXUV detector are worked out. Secondly, an overview of the line of sight arrangement in the vessel is presented and the third subitem describes the electronic DAQ system. In the final paragraph, the algebra for converting photocurrents into radiant power flux signals is given.

Opto-mechanical setup

Each camera was equipped with the same sort of linear detectors arrays. The pinhole principle was generally applied, while the camera housings were designed with special regard to the available space for installation and the demanded line of sight geometry. Figure IV.4 exemplarily shows the divertor camera, which is equipped with 48 channels. Table IV.1 gives the geometry inside the cameras. Figure IV.5 shows the camera positioning in the vessel with the respective the stereo positions. The cameras at the stereo measurement positions are denoted by $XUV^{\Phi=0}$ and $XUV^{\Phi=\pi}$, which the diagnostic acronym superscripted by the respective toroidal angle (while keeping in mind that the symbol for the toroidal angle of π stands for the accurate toroidal angle of 198 degrees).

The full line of sight setup is shown in Figure IV.5. The linear detector arrays consist of 16 silicon AXUV photodiodes. The geometrical dimension of one single detector is $2{\times}5\,\mathrm{mm}^2$ with a gap of 0.12 mm in between.

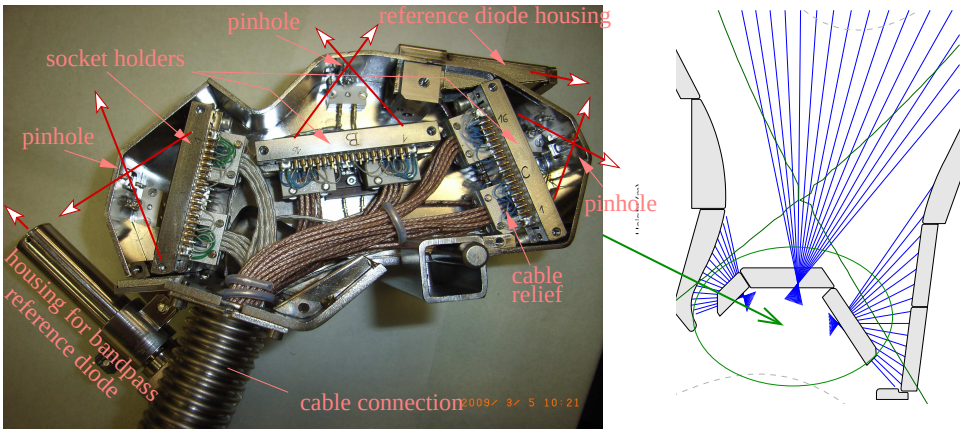

Figure IV.4: Divertor camera. A photography on the left shows the setup of the camera. Inside, three linear AXUV diode arrays are fixed. On the right, the line of sight configuration of this camera.

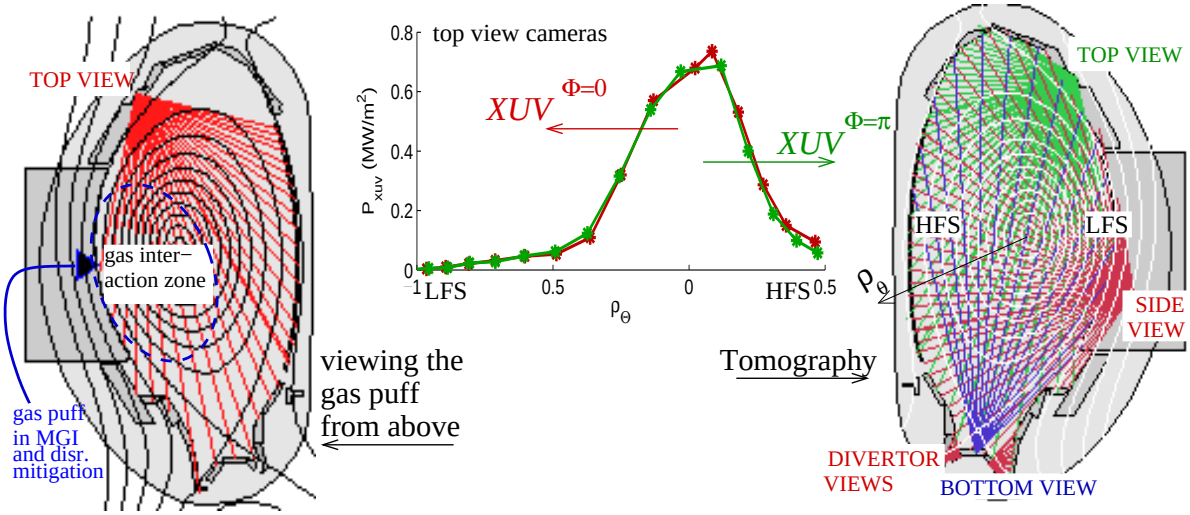

Figure IV.5: Full *XUV* setup. On the left, $XUV^{\Phi=0}$ with 32 lines of sight (LOS) is shown. Additionally, the position of the gas valve. On the right, the setup at $XUV^{\Phi=\pi}$ with 144 LOS is presented. In the middle, the stereo measurement of the top-view cameras is inserted (#24352, at $t = 3.1\,\mathrm{s}$) versus ρ_θ, see Chapter II.

	SIDE VIEW	*TOP VIEW*	*BOTTOM VIEW*	divertor
Pinhole-diode distance (mm)	38.8	38.8	29.5	20
Pinhole size poloidal×toroidal (mm)	0.8×2	0.8×2	0.8×2	0.8×3

Table IV.1: Pinhole imaging parameter.

AXUV detector

Photon detection

The outstanding properties of the n-on-p AXUV diodes are the 100 % internal carrier efficiency for *XUV* photons [17] and a relevant responsivity in the vacuum ultra-violet (VUV) spectral region [16]. The device responsivity γ_{D} is defined as the ratio of the measurable photocurrent yield and incident radiation power. The unity is therefore A/W. In Figure IV.6, responsivity versus photon wavelength is graphically shown.

The factor f_{vuv} inserted on the right in Figure IV.6 constitutes practically the worst case, meaning the maximal deviation of responsivity if all the incident radiation would be of $\lambda = 122\,\mathrm{nm}$. The factor f_{vuv} compares the reduced responsivity to the nominal responsivity. In this work, the signals are evaluated using the nominal responsivity $\langle\gamma_{\mathrm{D}}\rangle = 0.24\,\mathrm{A/W}$.

Figure IV.7 shows a scheme of the layer setup of the n-on-p AXUV diodes used in this thesis. The active area has a depth of approximately $50\,\mu\mathrm{m}$. The nitride passivating layer on top is of only 7 nm thickness, which lies in the range of the absorption length of VUV photons in SiO_2. Therefore, a fraction of the incident VUV photons transmits and reaches the depletion region, where they contribute to the measuring signal.

Neutrals detection

The non-responsivity of semi-conductors to neutrals is a noteworthy difference with respect to the foil bolometry. The foil signals are interfered by the stopping energy from fast neutrals deposited in the foil interior.

Responsivity degradation

In this thesis, silicon detectors were used, which are passivated by a silicon oxynitrided coating on top instead of conventional SiO_2. This principle relies on the higher energies required to break a Si-N bond compared to pure oxides as postulated in [14]. The formation of effective positive charges in the passivating layer shall thus be suppressed (Si-SiO_2 trapped states [13]) in order to avoid quantum efficiency loss. The issue of long-term degradation, which could arise due to the effect of latent recombination centres as reported in [12], was anticipated by applying a renewed detector assembly especially for the experiments presented in this document. During the plasma operation beforehand the series of MGI experiments, sensitivity degradation of the detectors was identified, which is documented in the following:

The reduction of the responsivity is due to superimposing effects arising from continuous ageing and repetitive radiation load or particle impact [15] during plasma operation. The earlier is an application independent, continuous degradation. The latter might be higher in disruptions or special heating configurations such as neutral beam injection,

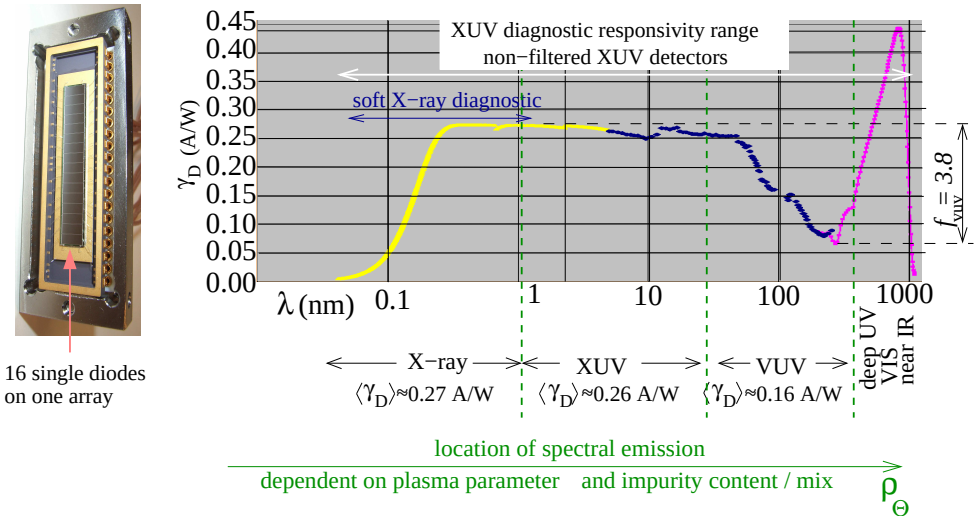

Figure IV.6: Responsivity of AXUV diodes. On the left, a photography of the 16-diodes array AXUV16ELG [11]. Right: The responsivity graph provided by the manufacturer IRD, Inc. The average responsivity value in selected spectral regions is denoted by γ_D. The factor for signal correction in the VUV spectral region is denoted by f_{vuv} (it is inserted exemplarily for the maximal deviation in the VUV).

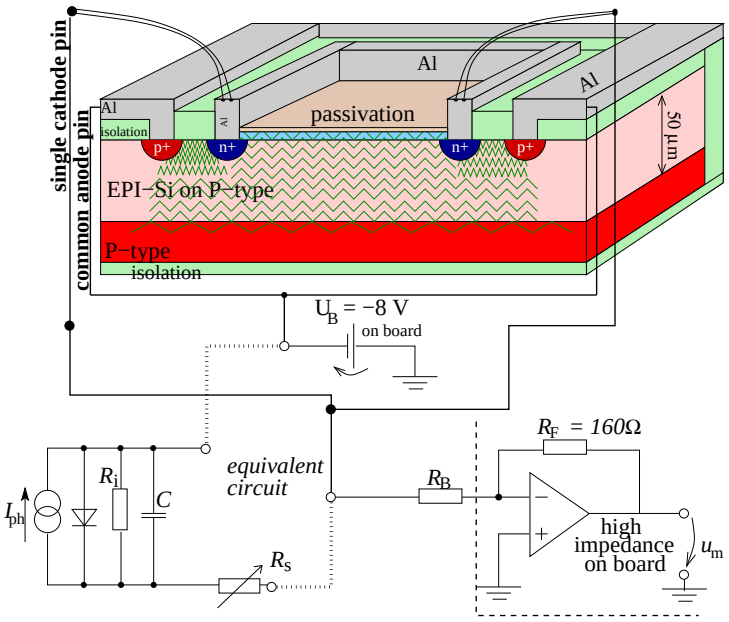

Figure IV.7: Scheme of the AXUV diode setup (AXUV16ELG) connected to the electric measuring circuit, where I_{ph} is the photocurrent.

which produce higher amounts of energetic particles and neutrons. Influences also may originate from the biasing or a deposition of carbon or tungsten on the detector surface (via EDX surface investigations, we found tungsten balls on the entrance window of a few diodes). The interplay and the major reason for sensitivity loss could not finally be clarified. An assessment of the transient behaviour of degradation is a nontrivial issue, because in a tokamak, there is no calibration lamp for any spectral region, which could have helped for characterising the effect.

Figure IV.8 represents the responsivity deviation between exposed diodes and unexposed ones. The unexposed diode array was not installed in the vacuum vessel. It serves as a reference.

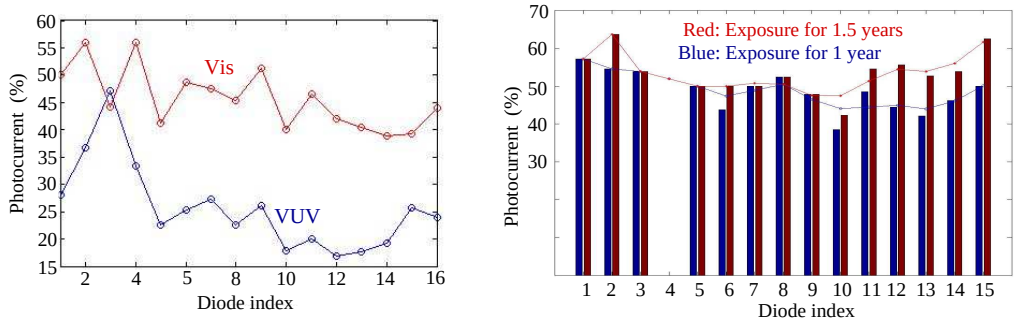

Figure IV.8: Instability of AXUV diode responsivity. Both plots show the responsivity of exposed diodes normalised to the responsivity of an unexposed diode versus channel indeces. Left: Spectral region related degradation degree. Exposure for two experimental periods (1 year ≈ 50 min plasma radiation). Responsivity reduction in the VIS (tungsten lamp) and VUV (254 nm) spectral region. Right: Responsivity loss during two exposure durations in comparison (1 year in blue and 1.5 years in red bars). The measurement was carried out using a sodium vapour lamp at 589 nm.

Figure IV.8 shows on the left the diode degradation dependency on the spectral region of incident light. The considered diode exhibits a reduced responsivity on VUV radiation down to only 30 % compared to the reference detector. The responsivity in the visible spectral region was degraded down to about 50 %. On the right in Figure IV.8, $\gamma_{\mathrm{D}}(\lambda = 589\,\mathrm{nm})$ of this diode is compared with an array, which was one full experimental period less applied. Though the durations of their application differs with half a year, the responsivity loss is comparable. This suggests that the responsivity loss comes about in two subsequent phases, while in the earlier, the loss might decrease faster and in the later, it might settle around a saturated degree. Note again, as clearly shown by the plots on the left hand side, the degree of degradation varies with different spectral regions.

Reference detector

Due to the photon energy dependent variation in responsivity, bandpass filters were applied in order to receive a reference signal for the critical VUV spectral region. Beyond this, two attempts were undertaken to equip the diagnostic with additional reference detectors covered by a bandpass filter with centre wavelength at 122 nm. As a first approach, two alone-standing MgF_2 substrate based Al multilayer filters were used. After 4 months of operation, the filters were laced with surface errors. The second attempt has been based on directly deposited filters on the diodes provided by IRD. The results are currently under investigation.

Capacity of the depletion region The thickness of the diodes determine the capacity, which has changed during two operational campaigns of plasma operation down to only 35 % of the initial value. Table IV.2 gives the reduction of the capacity C and the increase of the dark current I_d. The latter is a measure of the amount of structure errors in the layer.

		$\langle C \rangle$ (pF)	σ_C	$\langle I_\mathrm{d} \rangle$ (nA)	σ_{I_d}
AXUV16EL-G 6-1 #16	Exposed (2008)	191	44	70	21
AXUV16EL-G 6-1 #14	Unexposed	533	3.0	< 2	
AXUV16EL-G 6-1 #23	Unexposed	535	1.2	< 2	

Table IV.2: Reduction of capacity C and increase of the dark current I_d during exposure in 2008. The σ values give the standard deviation on one array.

Response speed According to manufacturer's data, the response time constant τ_r is of 0.5 μs.

$$\tau_\mathrm{r} \propto R_\mathrm{s} C \tag{IV.2}$$

where R_s is the serial resistance of the diode during irradiation (see equivalent circuit in Figure IV.7). As it was shown above, C degrades during exposure. Note that the response speed is a measure of the mobility of the free charge carriers equivalent to the mean free path L_e. The dark current I_d implies the amount of defect centres in the semiconductor interior. All in all, a small I_d and a big L_e result in a short τ_r. This applies for an unexposed diode. In case of degradation however, I_d dramatically increases, as shown in Table IV.2. In turn, L_e goes down but simultaneously, also the capacity decreases (according to Table IV.2). The response speed is changed depending on which effect is of stronger influence: The capacity decrease would enhance the response speed but the lower

mobility would lower the speed. In this work, however, a reverse bias of 8 V was applied, which should increase the response speed in either case[1]. The reverse bias voltage should also reduce the reabsorption losses due to a higher velocity of the free charges in the diode interior.

In conclusion, diode degradation is a serious problem with respect to the application over some months of operation. Against this background, the experiments investigated in this work, were rapidly completed within 13 days[2]. The *XUV* system was completely renovated with new diodes for these discharges. A diode sensitivity change during the short time slice was not of observable significance such that the comparability between the discharges presented in Chapter VI is guaranteed.

Electronic-DAQ setup

The DAQ of the *XUV* system is a new development in the ASDEX Upgrade data acquisition environment. The diagnostic is not integrated into the usual CAMAC bus system but runs on a distant UNIX multiprocessor RT-capable operating system (RT-OS). Data is saved in a direct memory access architecture for providing follow-up systems without significant latency (DMA). This pace-keeping data handling actually allows for *real-time* processing. The *XUV* DAQ system basically consists of three modules:

i. Analogue front end plug-in cards, PCI bus and interface cards

i. $\rightarrow$ *ii.* Hotlink II distant by Cypress (bidirectional optical fibre)

ii. SIO interface (serial input output) and cPCI(e) bridge design

iii. SUN station with a Solaris OS and an extended distant for PCIe

The diagram in Figure IV.9 shows the three subsystems schematically.

The analogue front end is a plug-in module, on which the transimpedance amplification, a user-defined amplification, an offset adjustment (Track and Hold, level-shift) and finally the analogue-digital conversion is integrated on board (ADC AD9243, quantisation step = 5 V/16384, Ampere $\rightarrow$ digits: $\frac{\text{Photocurrent}}{\text{Digits}} = \frac{954\,\text{nA}}{1\,\text{digit}}$, which gives a detectable photocurrent range of 15.6 mA.). In Figure IV.9, the dual stage amplifier arrangement is remote controlled by the user and can be adjusted via the bidirectional Hotlink II remotely in between the pulses. The adjustment of the amplifications automatically includes also the level-shift to a predefined offset in a Track and Hold circuit, which is active for 25 seconds. The setpoint was manually adjusted once. The board is applicable with

[1] The sampling rate is 2 μs, meaning, in the order of the response speed.

[2] From the 07.05.2009 (#24395) until 20.05.2009 (#24491). The previous discharges #23304...#23308 were carried out with a different set of diodes on one day.

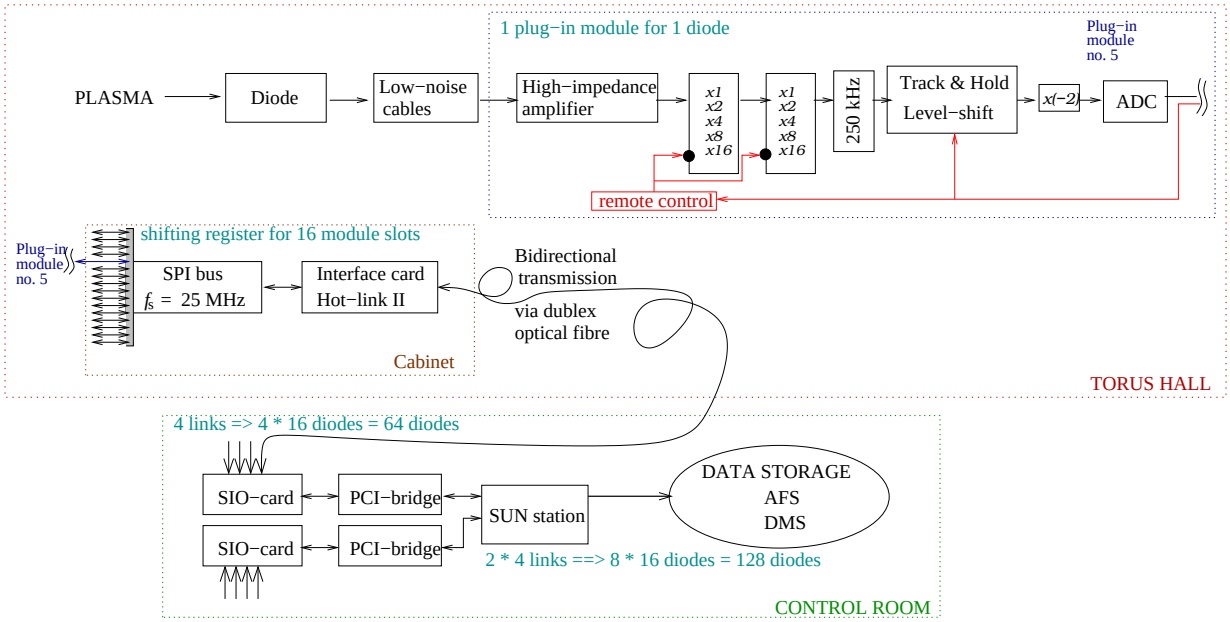

Figure IV.9: DAQ system of the *XUV* diagnostic. Signal amplifications are denoted by $x1$, $x2$, etc.

a difference input as well as with a reference input. In this thesis, both configurations were tried out, while the S/N ratio in both cases was extremely low. As already shown in Figure IV.7, the board applies a bias of 8 V.

The backplane, on which the modules are plugged in, is a macroscopic 16-bit parallel shift register (pipeline) with 20 insert points (16+1 are used, because 16 diodes compose one AXUV array, one slot for the FPGA board). Each slot constitutes a tri-state buffer, which either takes over the data from the board that is actually plugged in, or it treats the data from the neighbouring board. The FPGA board is the interface for communicating with the SIO-card in the control room. Dublex fibre optics connect the two cards.

The SIO-card (serial input output) consists of four logic modules:
The central FPGA, the four bidirectional slots for the 500 Mb Hotlink II connections, the timer clock receiver and a pluggable cPCI or cPCI(e)-controller. The SIO-FPGA is equipped with a timer, which generates time stamps for each sample. This prevents from a confusion of frames in the serial read-out process. If one computer treats two SIO cards, a frame of 128 data points is acquired each 2 μs. If a frame does not consist of 128 data points by the end of the sampling time, the frame is discarded completely. Otherwise, there would be the risk that shifts occur in the serial listing of the signals. Another safety measure is that the SIO-card tests the connections to the pipeline controllers in the torus hall before the plasma discharge starts. If one of the links is lost, data acquisition is not started.

Signal conversion

The relative calibration factor F_{geo} is given as [21]

$$F_{\mathrm{geo}} \;=\; \frac{A_{\mathrm{d}}\, A_{\mathrm{p}} \cos^2\alpha}{4\,\pi\, d^2}, \tag{IV.3}$$

where A_{p} is the pinhole area, A_{d} denotes the diode area, d is the distance between diode and pinhole and α is the incidence angle. The expression assumes the pinhole as a point source - which is applicable with an error smaller than 1 % because of the relatively far distance d between pinhole and diode compared with the extension of the pinhole h ($d\,/\,h \,=\, 30$). Table IV.1 lists the view design parameters.

The basic geometric factor F_{geo} must be multiplied with the responsivity factor $\langle\gamma_{\mathrm{D}}\rangle$, which implies the responsivity reduction in the VUV spectral region. As explained above, $\langle\gamma_{\mathrm{D}}\rangle$ introduces an uncertainty dependent on γ_{D} in Figure IV.6. In this thesis, $\langle\gamma_{\mathrm{D}}\rangle$ was set to 0.24 A/W in each discharge.

IV.2.4 Soft X-ray diodes

The soft X-ray cameras are situated at two toroidally spaced locations. It applies 208 photodiodes spectrally filtered by a Be-foil [8] in front of the entrance window. It permits the transmittance of photons from about 1 keV on [22]. The detector responsivity is related to the thicknesses of the depletion layer and the Be filter, as well as to the optical transmittance characteristics of Be.
Comparison of *XUV* and soft X-ray diagnostics: The discharge under consideration was introduced in Chapter III, where the series of minor disruptions was considered (Figure III.1).

Regard Figure IV.10, on the right: The soft X-ray signal is traced in blue, the *XUV* C-X views[3] at $\Phi = 0$ and $\Phi = \pi$ in red and green. All the three lines of sight cover poloidally the same plasma area. The energy expulsion at each minor disruption is featured by falling soft X-ray signals. An analysis of the expulsion itself is therefore hardly possible. Contrarily, the *XUV* diodes capture the energy bursts nicely. The amplitude is time-shifted, because the C-X views observe the heat pulse when it arrives in the divertor (this delay was also depicted by Figure III.3). The left hand side: The mode oscillations, which are clearly identified by the *XUV* channel, are not featured by the soft X-ray diagnostic, which is indeed not surprising due to the cooling. Under predisruptive plasma conditions, the *XUV* diagnostic is advantageous over the soft X-ray diagnostic for mode analysis.

The combination of the soft X-ray and the *XUV* diagnostics give a rough hint at the temperature evolution during a disruption. This is of great importance in MGI ex-

[3]The C-X channel is an almost vertical line of sight of the top view camera, which crosses the Centre and the X-point.

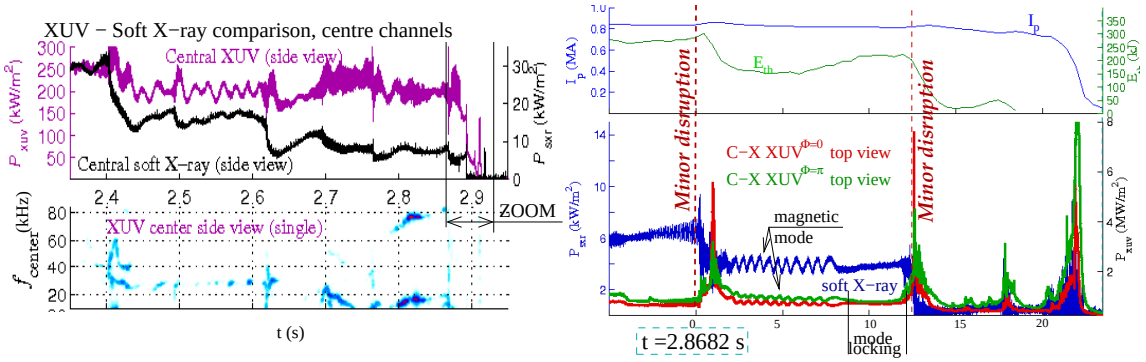

Figure IV.10: Soft X-ray - *XUV* comparison. Minor disruption series in discharge #24413. On the left: Two poloidally overlapping views through the central plasma from the side (side view cameras). Lower left: Spectrogram of the above-shown *XUV* signal. Right: The final three minor disruptions traced by signals from vertically viewing channels (C-X passes through the centre and the X-point). Symbols: E_{th} thermal plasma energy, I_{p}, plasma current.

periments, where temperature measurement by the ECE[4] is impossible due to the high densities.

[4]Electron cyclotron emission measurement is only possible below the cut-off density

Chapter V

Methods For Plasma Radiation Analysis

The fundamental methods for radiation analysis are described in this chapter. The XUV diagnostic is applicable for 2-D radiation tomography at one toroidal position ($\Phi = \pi$). The aims of tomography and the problems arising from the restriction in the number of lines of sight are explained in the first section. The subsequent section presents the calculation guideline for evaluating the total radiation loss under consideration of the toroidal asymmetry. The final section considers examples for the application of these methods for analysing disruptive plasmas. On the basis of the introduced methods and the diagnostic information given above, resistive foil and XUV behaviour in a disruption is documented and the chain of predisruption events in an edge cooling disruption is explained.

V.1 Radiation tomography

The aim of radiation tomography during an MGI scenario is to reconstruct the behaviour of radiative structures. In the subsequent chapter, the focus lies on studying the dynamics of a radiation front formed during the injection in an MGI scenario. Capturing the radial penetration velocity of the radiation front towards the core and finding poloidally concentrated impurity amassments are the tasks. Additionally, tomograms are used for converting radiant power flux densities to local emissivity.

V.1.1 Basic accuracy limitations

Tomography in a tokamak is based on stationary cameras. In this point, it basically differs from tomography in medicine, where the camera head rotates around the patient and thus consists of a large number of lines of sight. However, for plasma radiation recon-

struction, two approaches are commonly used for enhancing the image quality: Rotation tomography *a*) and the principle of including physically reasonable boundary conditions *b*).

a) Rotation tomography simulates a quasi-rotation of the cameras around the plasma column [22]. This is possible in cases of the known periodicy of a magnetic mode, which rotates around the torus. Then, the program calculates synthetic signals for virtual cameras positioned around the cross-sectional poloidal area at one toroidal location. Those synthetic signals are used in a subsequent step to reproduce the mode radiation again - now, with a higher accuracy. This is finally equivalent to e. g. magnetic resonance tomography with the difference that in the tokamak application, the lines of sight ensemble is partly virtual.

b) The diffusion on magnetic flux surfaces is used as a boundary: Under normal confinement conditions, the ratio between perpendicular diffusion coefficient $D_\perp$ and parallel diffusion $D_\parallel$ is only 10^{-6}. Henceforth, the density along a considered flux surface can be considered as a constant [20].

However, both methods *a*) as well as *b*) can not be applied for reconstructing disruption radiation. Rotation tomography is out of question, because in regard of a disruptive plasma, we are interested also in incoherent effects in various spectral regions. The aid of physical boundary conditions also can not be applied because of an enhanced perpendicular transport by turbulence and island formation often present in disruptions. Consequentially, disruption radiation reconstruction must be carried out without any physical boundary conditions and without virtual lines of sight. As a consequence, artefacts and inaccuracies will arise, which are explained and discussed with respect to both the intentions pursued by applying tomography as well as the allowed tolerances.

V.1.2 Maximum entropy tomography

The maximum entropy tomography system bases on the code package employed on W7-AS [23] and further developed for soft X-ray tomography on ASDEX Upgrade [22]. Imagine the plasma cross-sectional area, which is covered by the visual ranges of the crossed XUV lines of sight. In this respective plane, a grid is defined. The grid for XUV reconstructions cover - in contrary to the soft X-ray grid[1] - the entire vessel cross-sectional area and consists of 1073 squared pixels. A detector is illuminated by the pixel k, if the location of the pixel was within the respective visual range. The detector sees a bunch of pixels. Each one contributes to the measurement signal depending on the distance from the pinhole and depending on the distance between pinhole and detector. The contribution is normalised

[1] Soft X-rays are radiated in the core - the edge plasma is not considered. The regions relevant for XUV, however, concern the edge as well as the core.

such that the sum over all pixels with respect to the visual range of one detector, is 1. The contribution of pixels located outside of the visual range is 0. With this principle, each detector receives a contribution matrix $\underline{\mathbf{T}}$, which gives, multiplied with the pixel emissivities, the detector signal. However, the other way around, namely an allocation of emissivities to each pixel on the basis of given line of sight signals has to be done. The maximum entropy approach [24] bases on maximising the posterior probability P of the solution $\mathbf{g}$ with respect to a default model $\mathbf{m}$. The system has the entropy of

$$S \;=\; \sum_{\mathrm{k}} \mathbf{g}_{\mathrm{k}} \;-\; \mathbf{m}_{\mathrm{k}} \;-\; \mathbf{g}_{\mathrm{k}} \ln\left(\frac{\mathbf{g}_{\mathrm{k}}}{\mathbf{m}_{\mathrm{k}}}\right). \tag{V.1}$$

The posterior probability $P(\mathbf{g}|\mathbf{f}, I)$, which employs some *a priori* information I as well as the measured data $\mathbf{f}$ and the solution $\mathbf{g}$, reads as

$$P(\mathbf{g}|\mathbf{f}, I) \;=\; \frac{P(\mathbf{g}|I) \;\cdot\; P(\mathbf{f}|\mathbf{g}, I)}{P(\mathbf{f}|I)} \tag{V.2}$$

The maximisation was done with the curve fitting package Newton [23]. There are no boundary conditions or correlation rules involved - each pixel is completely independent on adjoining ones.

For later considerations on the radiation front penetration from the edge towards the plasma core, the geometrical position of the pixels are mapped to the magnetic coordinate q in order to give an emissivity profile versus q. The plasma equilibria during the MGI scenarios were reconstructed with a $100\,\mu$s time resolution. The equilibria were interpolated to the time scale of the XUV diagnostic in order to give radiation front positions versus q at each XUV sampling time.

V.1.3 Information loss by tomography

As mentioned above, the aim of XUV tomography is to follow the evolution of the cooling front during the MGI scenario. This subsection shows that this is possible albeit in special cases artificial smearing and distortion effects reduce the reproduction quality. Figure V.1 presents a table of reconstructions. In the upper row, synthetic radiation patterns are shown. In order to check, how the tomography method reconstructs given radiation distributions, those emission patterns are reprojected through the pinholes onto the XUV diodes. This reprocessing yields detector signals, which are again reconstructed with the XUV line of sight arrangement. The resulting tomograms are shown in the lower row in Figure V.1.

Ring-shaped radiation pattern:

The leftmost case constitutes a usual radiation distribution in the VUV spectral region during a steady state discharge. The structure is in fact reproduced but smeared significantly on the high field side due to the very low spatial resolution in this area. The

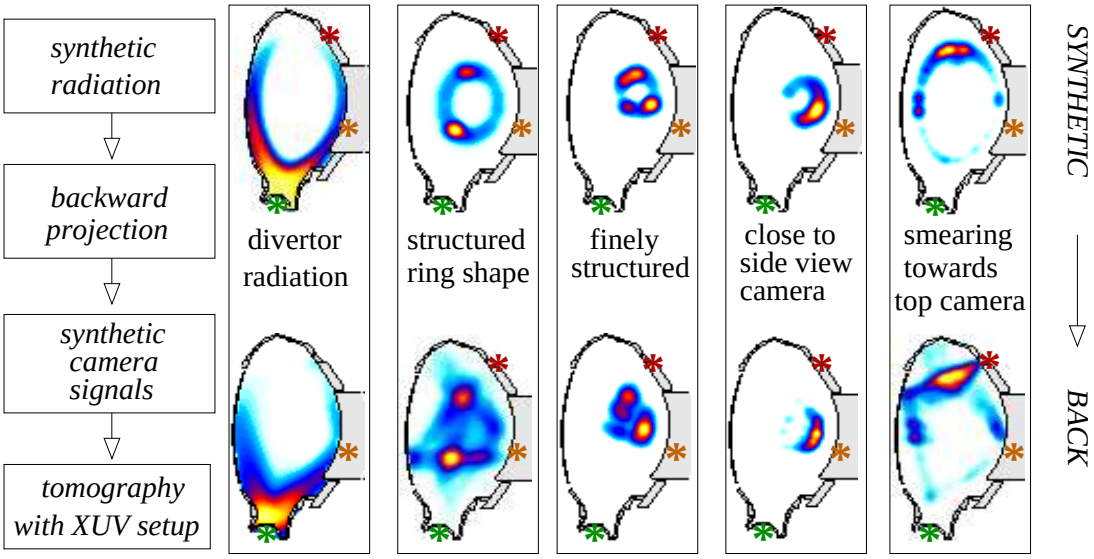

Figure V.1: Loss of information by radiation reconstruction. Patterns, which belong together, are ordered in columns. The upper row consists of synthetic test radiation patterns, the respective result is shown on the bottom. The reconstructions were done with the maximum entropy method without using any information about diffusive transport on flux surfaces. Asterisks mark the camera positions: Side view (light brown), top view (dark red) and the bottom view camera (green).

circular emission in the second case is distorted according to the line of sight geometry. Those views, which cross the points of higher emission are clearly visible and smear the emission points along their extension. The points itself, however, are located well. In the third column, the test radiation challenges the *XUV* setup, because two emission points in the luminous ring lie colinearly along one line of sight (bottom-up view). Such a case can lead to a slight displacement of the emission points. Regions of low emissivity actually can be dropped out absolutely, as demonstrated by the fourth case. The worm-like shape is reconstructed only in regions of sufficient luminosity. Note especially the rightmost case in the following paragraph:

Top view camera smearing:

The smearing by the top view camera is the outstanding case, which is of importance for correct interpretations in Chapter VI. The top view camera is installed close to the plasma and the radiation in the upper part of the plasma is dominant in first sequences in MGI scenarios. Pixels situated in the vicinity of the pinhole, have a nonzero contribution for several detectors simultaneously. In the maximum entropy regularisation, a smearing of the radiation towards those pixels is the case. A complete removal of the critical pixels would solve the smearing problem but would not be senseful, because in later investigations it is shown that the impurities injected during MGI are transported

along magnetic field lines, which leads to an appearance right in front of the camera, precisely in the critical region. Therefore, the pixels are generally included - meaning also in reconstructions of spontaneous disruptions worked out in this thesis.

Conclusions:

Bright areas are well locatable, structures of low-emissivities are distorted:

The shape of low-emissivity regions is poorly reconstructed, especially in front of the lower part of the inner heat shield (see first case). But - and this is the key point - the bright emission spots are locatable albeit special attention must be paid for the top view smearing. In MGI scenarios, where very bright and spatially constricted structures appear, we easily can neglect low emissivities and concentrate on radiation maxima and their decay versus q.

V.2 Stereo measurement

The radiation stereo measurement is realised by two toroidally oppositely situated diagnostic subsystems. It offers two important possibilities: Firstly, to evaluate the toroidal radiation asymmetry and secondly to give an approximation of the totally lost radiation. The earlier is important for assessing toroidal impurity propagation times when gas is injected at only one position. But also during the thermal quench, one is interested in the toroidal radiation asymmetry, because a toroidally asymmetrically radiating ITER plasma would cause localised heat loads, which could exceed tolerable limits of the beryllium wall. In this context of estimating total radiation radiation losses, the foil bolometry is treated as a reference detector in this section. In the subsequent section, applications of the methods are shown.

V.2.1 Radiation asymmetry

Since the detector housings of the top view cameras $XUV^{\Phi=0}$ and $XUV^{\Phi=\pi}$ are of identical internal setup and comparable poloidal adjustment, the measurement signals in Figure IV.5 match each other in case of unperturbed plasma operation. After normalising each detector signal p by the respective visual volume v_p of the line of sight geometry, the signals at each toroidal position are averaged over the 32 lines of sight at $\Phi = 0$ and $\Phi = \pi$, respectively. The indication number for toroidal radiation asymmetry TA reads as

$$\mathrm{TA} = \frac{P^0 - P^\pi}{P^0 + P^\pi}\ 100, \tag{V.3}$$

where P is the mean value of volume normalised radiation signals superscripted by the toroidal position Φ.

For MGI shut downs in particular, it is convenient to give indication numbers for TA in form of a temporal average in the shut down phase under consideration. Expressed in terms as

$$\langle \mathrm{TA} \rangle_{\mathrm{x}} \;=\; \frac{1}{\Delta t_0} \int_{t_{\mathrm{x}}}^{t_{\mathrm{x}}+\Delta t} \mathrm{d}t\, \mathrm{TA}(t), \tag{V.4}$$

where t_{x} stand for the start time of phase x of duration Δt.

Under stable discharge conditions, one would expect toroidal radiation symmetry, $\mathrm{TA} = 0$. Contrarily, a disruptive plasma could easily exhibit asymmetric radiation bursts due to e. g. locally penetrating impurities. In MGI experiments, where the gas is puffed at one toroidal position, a toroidal non-uniformity of radiation is not a surprise. Yet, the problem is complicated: The injected neutrals at $\Phi = 0$ ionise and radiate mainly at lines that correspond to first ionisation stages and cool the plasma efficiently. To higher ionisation stages, the energy necessary for further ionisations increases, which will lead to a lower ionisation rate and thus, a lower cooling efficiency. As long as the gas injection holds on ($\approx 2\,\mathrm{ms}$), the emission spectrum could dependent on the toroidal position. Such an effect would affect the TA number, because the detector responsivity is photon energy dependent. Since the plasma at $\Phi = 0$ will always be colder than at $\Phi = \pi$ during pre-cooling in MGI, the TA number could be underestimated. The worst case would be an error of a factor of 3.8, if all the photons detected would spectrally be concentrated in the VUV region. In the following, we will calculate TA without any corrections for possible temperature non-uniformities.

Two discharges are presented in this paragraph: The series of minor disruptions in #24413 introduced in Figure III.1 and discharge #24352, which was used in Section IV for demonstrating the toroidal radiation symmetry during flat-top conditions. The two considered cases exhibit fundamental differences, which makes clear that the TA behaviour in a cold plasma is not necessarily unique. The time windows in those pulses were selected under the criterion of comparable situations: In both cases, a fast radiation pulse at $\Phi = \pi$ is shown. Both last only a couple of microseconds (left: $16\,\mu\mathrm{s}$; right: $80\,\mu\mathrm{s}$). We may consider this burst as a sort of a *'test pulse'* and discuss the plasma response toroidally π around.

The basic principle of TA

Figure V.2: In the preprogrammed current ramp-down of discharge #24352, a disruption occurs with a very low amount of energy ($E_{\mathrm{th}} = 15\,\mathrm{kJ}$) and of low current ($I_{\mathrm{p}} = 80\,\mathrm{kA}$), traced in Figure V.2 on the upper left. In the zoomed time window below, the rising edge of the green $XUV^{\Phi=\pi}$ radiation curve, is only of $16\,\mu\mathrm{s}$. The toroidal answer to this pulse rises $40\,\mu\mathrm{s}$ later (red $XUV^{\Phi=0}$ curve, equivalent measurement to $XUV^{\Phi=\pi}$). On the bottom, left row, the resulting TA behaviour is traced: The burst is announced by an unbalanced toroidal radiation reflected in the drift of TA away from zero. The TA-peak

implies the burst at $\Phi = \pi$. After 40 μs, TA initially becomes attenuated, then reduced and finally even reversed due the strongly rising $XUV^{\Phi=0}$ signal. The sign change of TA occurs when the $XUV^{\Phi=0}$ exceeds the $XUV^{\Phi=\pi}$ signal. The considered time window is cut at a time, at which TA evolves towards zero.

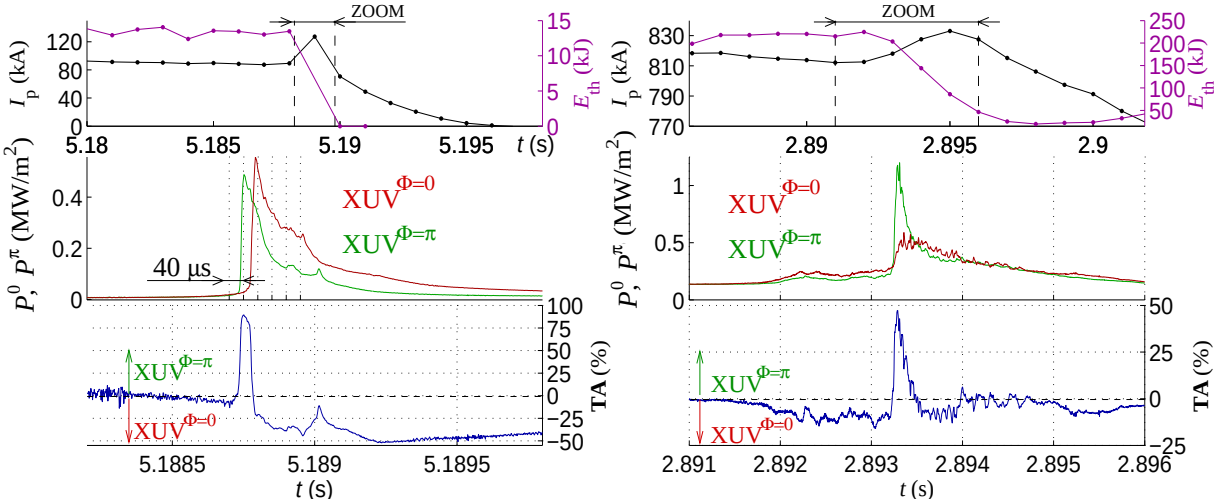

Figure V.2: Toroidal radiation asymmetry of fast bursts in unmitigated disruptions. Left: Disruption in discharge #24352. Right: End of the mode locking phase in the minor disruption series in discharge #24413. First row: E_{th} (violet) and I_{p} (black). Second row: Volume normalised average values of the top view camera signals at $\Phi = 0$ (red) and $\Phi = \pi$ (green) in a zoomed time window. Bottom: The TA number (according to Equation V.3).

The toroidal response characteristics diverge in a great extent comparing the left and the right case in Figure V.2. On the right hand side, the test pulse represents the release of thermal energy at the end of the mode locking phase in discharge #24413. The pronounced peak occurs only at one position.

Note, conclusively, the toroidal radiation asymmetry number TA reaches values close to 100 % in case of a temporal shift in between the emissivities at $\Phi = 0$ and $\Phi = \pi$.

V.2.2 Total radiation

In order to evaluate total radiation with the XUV diagnostic, the toroidal radiation asymmetry as well as the deviation from a reference detector must be taken into account. The toroidal asymmetry is evaluated on the basis of the stereo measurements. As reference detector, we use the foil bolometry, albeit the application is limited by the low time resolution. The idea is to tag each pixel of the XUV tomogram with two factors: An asymmetry factor and a factor, which implies the deviation from the reference detector. Firstly, the toroidal asymmetry is considered:

Figure V.3: The pixels of the XUV tomogram are plotted. Exemplarily, a close-up view of the inner divertor is shown. Each line of sight has a certain visual range. The

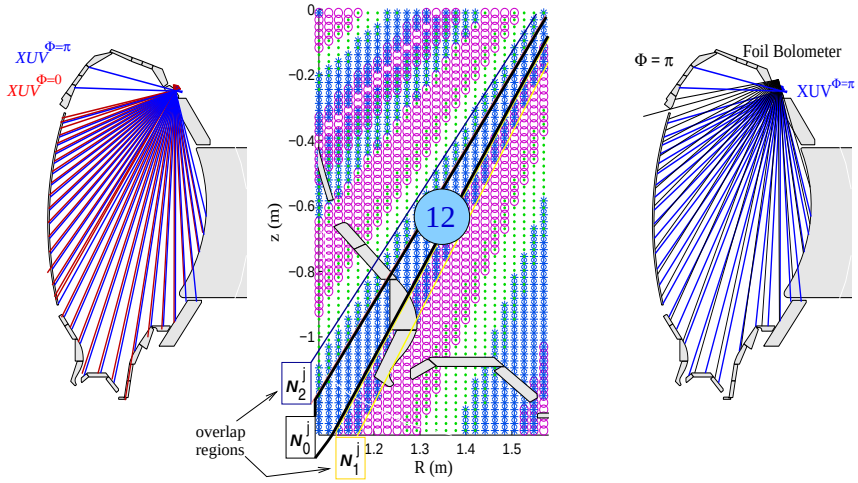

Figure V.3: Allocation of the pixels. The drawing in the centre shows the pixels in the visual ranges of different lines of sight of the top view camera $XUV^{\Phi=\pi}$. Each line of sight j sees a set of pixels $\mathbf{N}^j$. Regions, which overlap with neighbouring visual ranges are subscripted by '1' and '2', respectively. The non-overlap region (pixel subset) is subscripted by '0'. Exemplarily, the subsets are marked for line of sight 12.
Left: $XUV^{\Phi=0}$ and $XUV^{\Phi=\pi}$ lines of sight are drawn in one poloidal plane.
Right: The lines of sight of the top view cameras of foil bolometry and $XUV^{\Phi=\pi}$ are drawn.

pixels, which lie within the visual range of line of sight 12, for instance, are plotted in blue symbols. They are marked in the image. This channel overlaps with the neighbouring channels 11 and 13. The overlap regions are also marked. The detector signal of channel 12 is compared with the equivalent channel toroidally π around, which results in a toroidal asymmetry number only for the pixels, which lie within the visual range of channel 12. We name this number a *channel related asymmetry* number. The same is done for the other channels, which results in 32 channel related asymmetry numbers. Pixels, which lie in the overlap regions of e. g. channel 11 and 12 get the mean value of the asymmetry numbers of those channels. Note that the resolution of this channel related asymmetry applies only perpendicular to the lines of sight - along the lines, the pixels are tagged with the same number.

For evaluating absolute power values, the pixels are additionally tagged by a foil-to-diode ratio: Regard the right hand side in Figure V.3: The lines of sight of XUV and foil differ quite a lot in the poloidal adjustment. Toroidally, they are only a few centimetres separated. Channels were selected, which come as closest to each other[2] (in poloidal direction) and may therefore be comparable. The ratio between the volume normalised foil and diode signals are the correction factors for the selected lines. Hereby, the diode

[2]The space in between is interpolated, so that each pixel gets a foil-to-diode ratio.

is forced to the foil.

The two factors for each pixel can be written as matrices $\underline{\mathrm{TA}}$ for the toroidal asymmetry matrix and $\underline{\mathrm{FD}}$ for the foil-to-diode ratio matrix. They multiply in the radiation energy equation as

$$E_{\mathrm{rad}} \;=\; \sum^{\mathrm{n}} \underline{\mathrm{E}} \cdot \underline{\mathrm{TA}} \cdot \underline{\mathrm{FD}} \cdot \underline{\mathrm{U}} \cdot \underline{\mathrm{A}}, \tag{V.5}$$

where in $\underline{\mathrm{A}}$ the pixel areas and in $\underline{\mathrm{U}}$, the toroidal circumference for n pixels are saved.

In order to express the deviation between foil and XUV in one single time trace, the f_{vuv} factor is defined as follows:

$$f_{\mathrm{vuv}}(t) \;=\; \frac{1}{n} \sum^{n} \underline{\mathrm{FD}}(t). \tag{V.6}$$

According to the section below, where foil bolometry is compared to the diodes, the factor f_{vuv} could be regarded as a measure for the VUV contribution that the acquired signal implies. In case of high VUV contribution to the total radiated energy, the factor would reflect the responsivity dip of diodes in this critical spectral region. An understandable factor will be of 3.8 if the emissivity spectrum is concentrated to the VUV region. In the following section, however, it is shown that this factor reaches values of significantly higher magnitudes under certain conditions.

V.3 Applied methods

Up to this point, disruption issues were introduced, diagnostics explained and the methods for radiation analysis presented. This section is based on those items: In the first subsection, radiation signals are used to evaluate total radiation losses during a disruption. In this course, we will compare foil bolometry data with XUV data. The foils could in principle act as reference detectors. The bolometry is, however, equipped with an electronic filter circuit with a 50 Hz edge frequency due to a relatively high noise level. For MGI measurement, this time resolution is far below the demanded one, because an MGI experiment lasts only 4 ms in total. Therefore, a reference detector for MGI is not available. Foil bolometry is useable for the relative long pre-cooling phases in the minor disruption series as well as the edge cooling disruption. In the second subsection, we focus on the radiation dynamics depictable with the XUV setup.

V.3.1 Total radiation evaluation

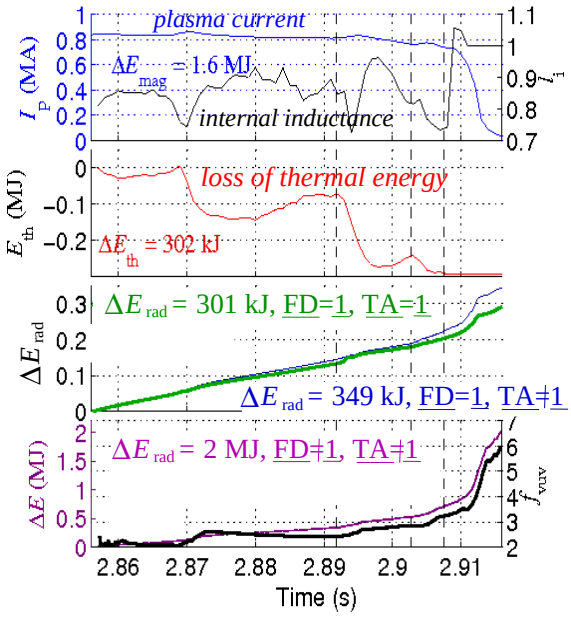

Figure V.4: Comparison: Foil bolometry and AXUV diode signals during the series of minor disruptions in discharge #24413.

Figure V.4 presents the radiation loss evaluated with the above-introduced methods. The inserted Δ-values give the change of the energy at the end of the plot window. On the top, plasma current I_p and internal inductance l_i, when substituted in Equation III.1, the magnetic energy E_{mag} can be evaluated. The third row concerns the application of Equation V.5. The toroidal asymmetry matrix TA is switched off (green) and on (blue). It is switched off, if we force it to 1. Significant: The blue and green curves come apart from each other during the thermal quench, which implies an increase in toroidal asymmetry. On the bottom: The f_{vuv} factor versus time (black), which gives the discrepancy between the foil measurement and XUV. The violet curve represents the application

of both TA as well as FD (violet). The f_{vuv} factor rises successively and reaches a value of 6 in the current quench, which means that the foil bolometer provides a 6 times higher signal than XUV. This feature is not deducible from the responsivity function shown in Figure IV.6. That curve, which is provided by the manufacturer, would allow a deviation not larger than a factor of 3.8. This dramatic increase of f_{vuv} to values lying well above the predictions might originate from a degradation of the diodes in the respective spectral region relevant in the colder plasma. Those deviations in the energy quenching phase forces us to regard the thermal and current quenches as critical phases, in which the radiation power is of high measuring error.

Although the origin of such a high magnitude of f_{vuv} is obscure, the cooling is nicely featured in Figure V.4. Regard the black f_{vuv} curve: Starting with an f_{vuv} of 2, the minor disruptions increase f_{vuv} subsequently. This feature is expected: The emissivity spectrum from the plasma shifts more and more from the soft X-ray and XUV into the VUV spectral region, where the diodes are of less sensitivity. The inverse behaviour, namely the reheating in between the first and second minor disruption (from 2.87 s to 2.89 s), is also obvious in a slight reduction of f_{vuv}.

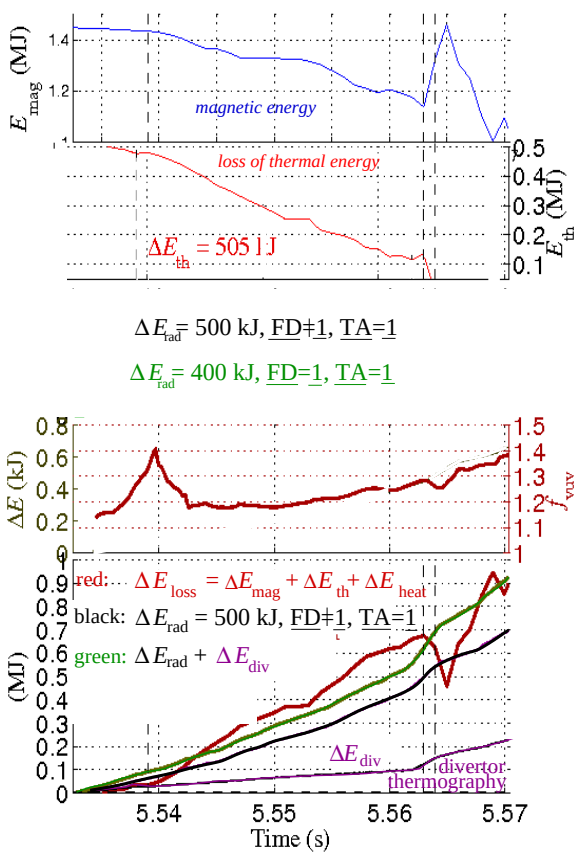

Figure V.5: Energy balance for the long pre-cooling phase in the edge cooling disruption.

With additional impurity content:
The edge cooling disruption is considered (overviewed in Figure III.2). Nitrogen is puffed during the whole discharge for controlling the divertor temperature. It provides for a uniform radiating mantle around the plasma [100]. Nitrogen is used for adjusting the main energy sink in the plasma periphery [99], while energy losses from the core are kept low. The relatively long pre-cooling phase in the edge cooling disruption in #24428 allows an appropriate use of foil bolometry for the energy balance. In the presence of nitrogen, the f_{vuv} is closer to 1 than in the above-presented case, where no impurities were puffed. The plasma radiation spectrum might be adjusted such that the relation between the detector responsivities (semi-conductor and gold foil) lead to a smaller deviation between the two diagnostic signals than above.

Figure V.5 and Figure V.4 demonstrate a fact, which is actually not a surprise: The impurity mix in the plasma determine the behaviour of f_{vuv}. In a disruptive scenario, this circumstance leads to a complex behaviour of f_{vuv}, because the plasma temperature change leads to a change in the radiated spectrum and therefore to a change of the diode responsivity ($\gamma_{\mathrm{D}}(\lambda)$). Additionally, this is combined with the responsivity instability, which is again related to the spectral region of incident light (see Figure IV.8).

V.3.2 Contour plots and tomograms - the edge cooling disruption

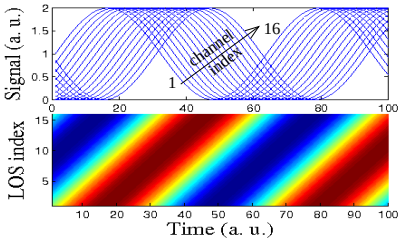

Figure V.6: Contour chart imaging. A spatially constricted radiation source passes through the fan of 16 lines of sight.

Luminous structures, which pass through the fan of lines of sight, are often considered throughout this work. The time shift of the signals captured by the channels of ascending index can nicely be featured by contour plots. In the neighbouring Figure V.6, signals are synthetically generated for 16 lines of sight (LOS). The channel index versus time gives a contour of inclined red stripes. In reality, this would be a radiation source, which starts moving on the low-field side (low channel indices) passing through the view geometry and arriving at the high-field side (high indices) after 30 time points.

An example for an oscillating radiator is given by the back-and-forth switching controlled divertor MARFE in the prehistory of the edge cooling disruption in discharge #24428. It was introduced in the context on the chain of events in Chapter III. The prehistory of the disruption reveals several interesting features:

- A controlled MARFE regime, in which the MARFE performs a periodic back-and-forth switching movement between the X-point and the inner divertor.
- An uncontrolled MARFE regime, characterised by a MARFE movement and 2/1 mode excitation.
- Core mode correlated edge cooling

Brief overview: The divertor feedback controlled valve puffs N_2 for keeping the divertor temperature below a predefined value [97], [98], [99]. Impurities build a uniform mantle around the plasma [100]. In the divertor, the XUV diagnostic observes a MARFE. It switches back and forth between the inner divertor and the X-point with a frequency of about 1 kHz. Such a MARFE regime is known [49]. The MARFE is stable at its respective position. Stable means that the energy input provided along the magnetic field line balances the impurity radiation from the MARFE. The MARFE moves, in case of imbalanced inwards/outwards energy fluxes. In this case, the MARFE moves between X-point and an area close to the divertor plates. These are two different input flux regimes. At the X-point, the cross-field transport will dominate the energy consumption - at the divertor plates, it will be the energy flux provided by the SOL. The system is complex and involves also recycling considerations, which are beyond the scope this thesis. The important event in this scenario is the NBI system failure at around 5.5 s. It leads to a

drop of the total input power and therefore to an imbalance of the MARFE condition. The MARFE stops the oscillation movement, leaves the divertor region and moves upwards along the inner heat shield. An extensive edge cooling situation arises and a resonant 2/1 mode is excited due to rising gradients.

Back-and-forth switching controlled divertor MARFE

Figure V.7 shows the back-and-forth movement. The X-point radiation is only seen by

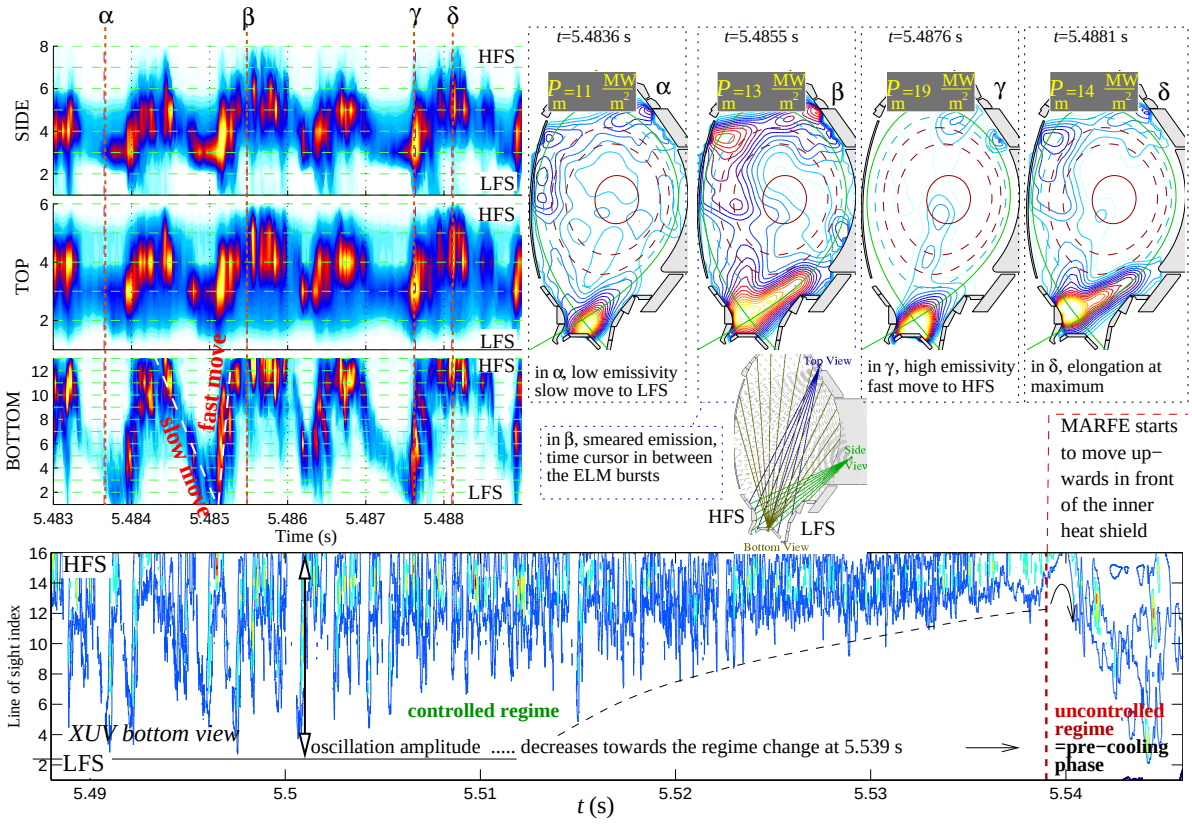

Figure V.7: Back-and-forth switching controlled MARFE in the prehistory of the pre-cooling phase in #24428. Left: Three contour charts present selected signals of XUV cameras (side, top, bottom). The contours include the lines of sight, which are geometrically shown in the vessel drawing in the middle. Right: Tomograms at the time points α, β, γ and δ (time markers also in the contours). Radiant power flux density is given as an average value from the top-view camera signals. Bottom: Bottom view camera shows the switching, the amplitude reduction and the end of the switching. HFS: High-field side. LFS: Low-field side.

6 lines of sight of the side camera, only four of the top view but at least by 13 of the bottom view. The back-and-forth movement of the X-point radiation spot is featured by each camera, which allows a tomographic reconstruction of the phenomenon. The third and fourth reconstructions in the presented series imply an oscillation amplitude

ranging from the private flux region[3] up to the high-field side region clearly above the X-point (the regions are shown in Figure II.1). The oscillation cycle time within the considered time window is about 1.2 ms. Two precedent tomograms were set to times in the short emissivity gaps marked by the leftmost cursors in the contours. The bright spots in the contours represent the short radiation peaks. On the bottom of Figure V.7, the chart spans over an extended time range, which also includes the onset and a part of pre-cooling phase from t=5.539 s on. As a prehistory with respect to the pre-cooling, the oscillation becomes restricted in its amplitude. This reduction of the oscillation amplitude and displacement of X-point radiation to the high-field side region upon the vertical z-coordinate of the X-point, is accompanied by a smooth degradation of the thermal energy content.

[3]Private flux region is marked in Figure II.1.

Uncontrolled MARFE regime

As a consequence of the heating system failure, the MARFE moves upwards along the inner heat shield as shown in Figure V.8.

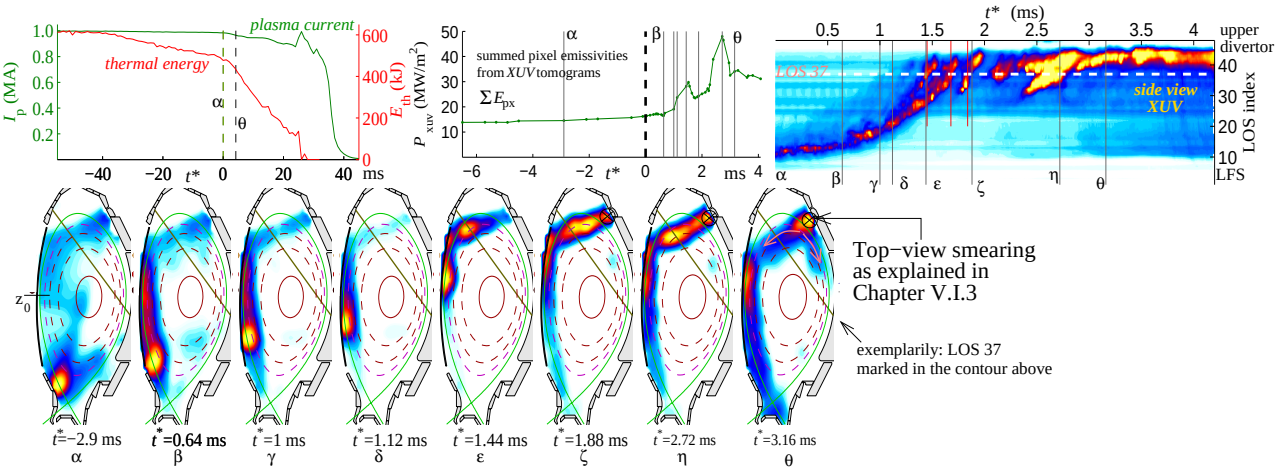

Figure V.8: Uncontrolled MARFE regime and the onset of pre-cooling.
$t^* = t - 5.539\,\mathrm{s}$. The green cursor in the plotting on the upper right marks the onset of the pre-cooling phase. The duration in between green and black cursors is zoomed in the plots on the right: Contour chart of *XUV* time signals from the side view camera. LOS stands for line of sight.

MARFE movement

At $t^* = 0$ (t =5.539 s), the MARFE starts to move, which is illustrated by the series of tomograms as well as the contour chart of the side view camera. In the latter, the vertically moving structure is indicated by the bent bright line. Tomographic reconstructions give the phase velocity of the radiation structure: The leftmost image presents the radiation distribution before the move. After t^*=0, the major structure accelerates slowly, while smaller structures escape already at the times t^* =0.64 ms and t^* =1 ms (see also the dark blue stripes in the contour chart before the luminous one). Below the vertical coordinate z_0, which denotes the smallest separatrix-limiter distance, a phase velocity of about 600 m/s is evaluated, while the structure accelerates up to velocities of about 1800 m/s reached above z_0 (z_0 is inserted in frame α). Here, the structure is split up into two separated parts.

The movement and radiation activity nearby the upper divertor enhances strongly the over-all radiated power. The time trace in the centre of Figure V.8 shows the radiated power: It traces the time evolution of the sum of all pixel emissivities of the tomograms.

Radiation activity during the pre-cooling phase

After the MARFE rapidly moved upwards, it is flushed out and impurities are distributed uniformly in the edge. The $m/n = 2/1$ mode in the centre appears during the uncontrolled MARFE sequence. A core mode correlated edge radiation appears[4]. Regarding Figure

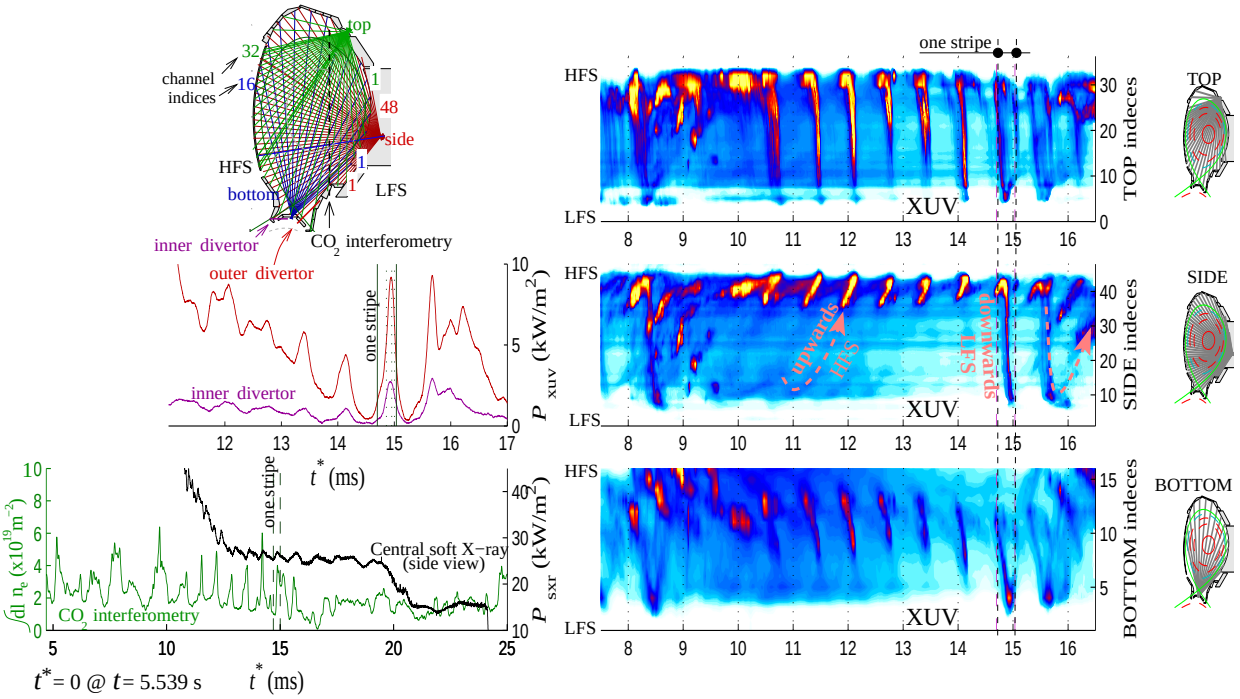

Figure V.9: Core-edge interaction during the pre-cooling in #24428. Top, side, bottom view contours of XUV on the right (plus the corresponding geometry). On the lower right, the laser interferometer signal of the main plasma view is traced. The poloidal and toroidal rotation frequencies of the mode are of 1.77 and 1.55 kHz, respectively.

V.9: The bright stripes, given in all the three contour charts, cover almost the full visual range of the cameras. They are generated in the edge plasma. The correspondence of the mode oscillation with XUV edge radiation is important also in MGI shut downs, where such structures appear in a scenario, where argon is injected. The assumption is that the central mode enhances the radial energy transport such that the impurity mantle, which surrounds the plasma, traces the mode position. The rotation is inferred from the stripe pattern: Stripes with two different inclinations appear: The dark blue stripes and the bright stripes, both marked in the side view contour (*upwards* and *downwards*).

[4]This correlation turned out previously in Figure III.2, in which soft X-ray and XUV were plotted in the same window (upper right)

Chapter VI

Analysis And Discussions On Massive Gas Injection Scenarios

Both the *XUV* diagnostic as well as the highly-pressurised MGI valve are technical novelties in the ASDEX Upgrade tokamak. Radiation phenomena, which are caused by the massive injection of noble gases into the plasma edge, had not been diagnosed before this work. As explained in Chapter IV, the *XUV* diagnostic is able to resolve the dynamics in time over a broad emission band. But although the *XUV* diagnostic is advantageous over previously applied radiation diagnostics for disruption radiation measurement, the absolute power evaluation is affected by the dependence on impurity composition and temperature (shown in Chapter V). It is therefore hardly possible to reassess absolute radiation power without a reference detector. The approach of applying spectrally filtered *XUV* diodes failed and spectrometers were disconnected for safety reasons during MGI. Absolute radiation power evaluation is therefore only possible by taking the input/output energy balance into account - keeping in mind the knowledge gained from Section V.3: Foil bolometry and *XUV* signals disagree more and more with decreasing plasma temperature even if no impurities were present (surprising effect of $f_{\mathrm{vuv}} \rightarrow 6$ as discovered in Figure V.4 possibly originating from responsivity reduction for particular photon energies). Consequentially, a restriction to the prehistory of the major disruption in an MGI scenario is mandatory for determining absolute power values.

Note the basic issue of radiation power evaluation does not impact the investigations on impurity propagation, because the sensitivity on photons from the XUV over the VUV, the UV through to the Vis spectral region is sufficiently high for providing the full information for the whole disruption duration. With respect to the development of theoretical models, it is mandatory to trace and characterise the impurity dynamics in three dimensions. This is the aim in this chapter, which is organised as follows: At first, we will overview an MGI pre-cooling phase and a moderate puff from the distant gas valve for visualising the significant differences. In the subsequent sections, we will focus on MGI

exclusively and investigate the radial, toroidal and poloidal impurity propagation. In the following, the quench phases will be considered.

VI.1 Comparison of moderate and massive injection

A comparison between the pre-cooling time in massive injection of 3.3 bar l and the pre-cooling induced by the moderate puff of 0.18 bar l is subject of this section. The moderate puff scenario corresponds to the flow chart in the middle of Figure III.5, which represents a disruptive plasma. In this special case presented here (#24383), an intervention for suppressing precursors before the major disruption was not applied. The prehistory of the sequence zoomed in Figure VI.1 is comparable to the series of minor disruptions as presented in Figure III.1 and Figure IV.10, which reduces the thermal energy of the plasma step by step. It is the same low-q operational scenario with non-linear mode growth. The *locked mode detector* [48] reacts on magnetic signals that exceeds the predefined threshold and triggers the moderate gas puff. This is the case when most of the E_{th} content is degraded - we apply the mitigation puff to a cold plasma[1]

The MGI valve is triggered at $t_{\mathrm{tr}} = 2.98\,\mathrm{s}$. The time interval in between valve opening and onset of cooling is included in the pre-cooling time. Thus, in the MGI case we can set the leftmost cyan cursor to t_{tr}. The onset of the pre-cooling is detected in both cases - moderate and massive - by $XUV^{\Phi=0}$, which views the gas jet from above (first dark blue cursor). The red curve traces the plasma response in front of the valve ($\Phi = 0$). The toroidally mirrored position $\Phi = \pi$, where the $XUV^{\Phi=\pi}$ subsystem is located, shows the response traced by the green curve. In MGI experiments, it is generally observed that the time of radiation detection at $\Phi = \pi$ corresponds to the start of thermal energy E_{th} degradation, the onset of small-scale activity in the Mirnov and soft X-ray signals (the small fluctuations are only visible in zoomed plots). In the plots of the MGI example, this time is marked by the second blue cursor (for defining τ_{tor} in the later section). From this time on, the cooling effect applies to the entire plasma column, whereas the toroidal distribution of the impurities is largely unequal as indicated by the relation between $XUV^{\Phi=0}$ and $XUV^{\Phi=\pi}$ curves.

In Figure VI.2, the radiation fronts in both scenarios are shown. The contours represent the line of sight signals of $XUV^{\Phi=0}$ and $XUV^{\Phi=\pi}$ (both top views) versus time. Directly in front of the valve, at $\Phi = 0$, the impurity-plasma interaction zone is observed from above by $XUV^{\Phi=0}$. Similarities and differences shall be emphasised in the following: The plasma interaction zone in MGI is a constricted luminous area at $\Phi = 0$. It is only observed by one or, occasionally, two lines of sight. This results in a luminous zone sharply

[1] The wording 'radiative dissipation' as noted in Figure VI.1 might thus be more convenient rather than 'pre-cooling'.

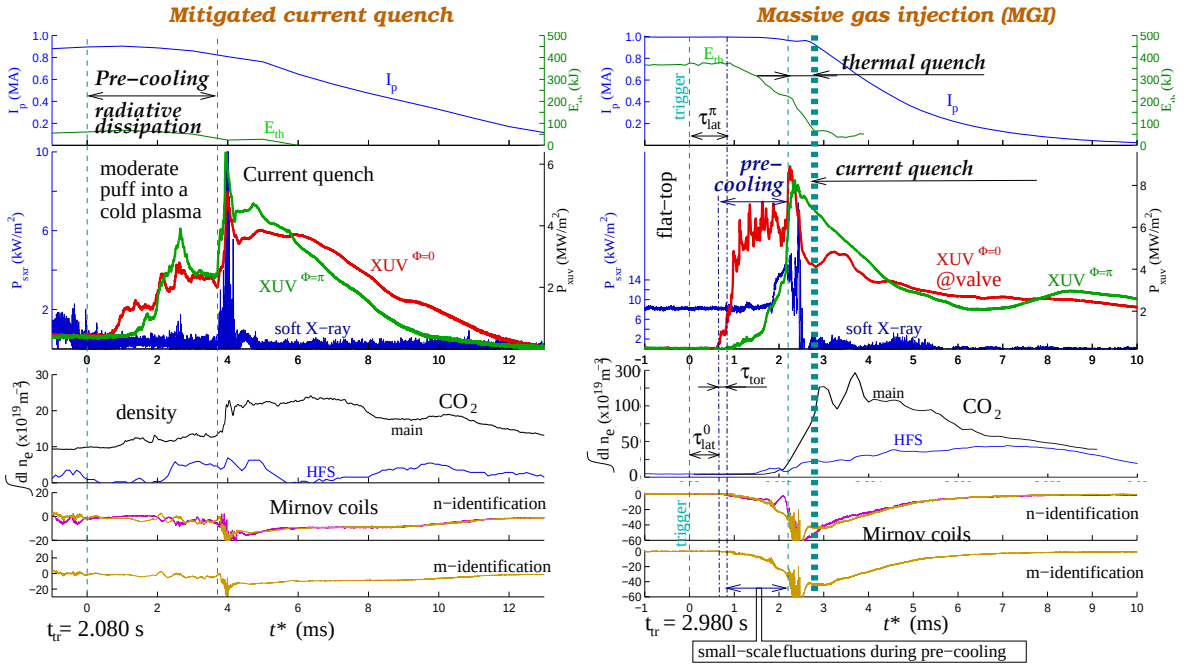

Figure VI.1: Overview of injection scenarios: Moderate (left, 0.18 bar l, distant valve, ≈ 150 cm distance from the plasma edge) and massive (right, 3.3 bar l, ≈ 13 cm away from the plasma edge). Signal labels are attached to the plots. The t^*-axis is zeroed at $t = 2.08\,\mathrm{s}$ (the safety system does not record the exact trigger time) and $t^* = t - t_{\mathrm{tr}}$ with $t_{\mathrm{tr}} = 2.98\,\mathrm{s}$ (MGI)..*XUV* plots correspond to earliest responding lines of sight. Neon is used in both cases, #24383 left and #24442 right.

delimited towards both sides, higher as well as lower channel indices. It remains the only structure for a couple of hundreds of microseconds (more precise below) and retains its initial constricted form. In the moderate puffing scenario, this area is broader and smears over, at least 5 lines of sight, which implies that the plasma response is extended over a broader surface on the low-field side. This is reasonable, because the impurities travel through the whole port of about 1.5 m length before they approach the plasma edge. Yet, a similarity of the two cases is the inclination of the track (versus time), which implies that the radiation front leaves the visual range of the one channel and enters the view of the next one, which views the plasma further inside. Reasonably, the radiation front moves. An outstanding individual property of MGI is the appearance of very pronounced inclined stripes. Two of them are marked in Figure VI.2 with arrows and tags (*'filaments'*). An inclined stripe in such a contour means that a spatially constricted radiation structure runs through the line of sight geometry (as explained in Section V.3.2). Its velocity is high compared to the velocity of the radiation front (a precise investigation on propagation velocities follows in later paragraphs).

In the moderate puffing case, the emission from the cooling front decays and the

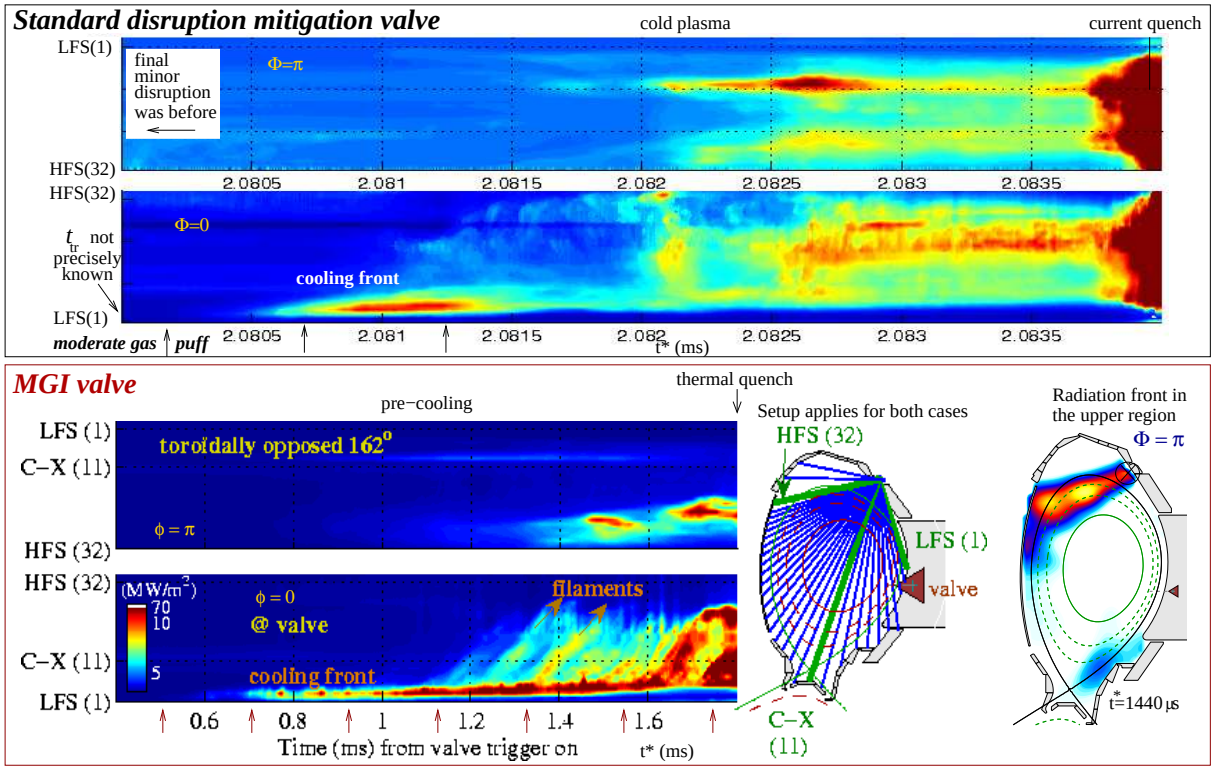

Figure VI.2: Radiation distribution during the pre-cooling in the mitigated disruption case (#24383, above) and the MGI shut down scenario (#24399, below), both in neon. $XUV^{\Phi=\pi}$ and $XUV^{\Phi=0}$ top view camera measurements are presented. The geometry at both toroidal positions is given in the lower middle. The denotation C-X marks the line of sight, which crosses the plasma centre and the X-point. HFS (high-field side) and LFS (low-field side). Arrows symbolise the gas puff direction. On the right, a tomography at $\Phi = \pi$ is inserted. (Time t^*=0 corresponds to t=2.08 s in #24383 and t_{tr} = 2.98 s in #24399.) The black cross on the upper right in the tomogram marks the artificial smearing towards the camera.

poloidal redistribution of impurities might be rather subdued. In MGI, the radiation from the cooling front holds on until the end of the pre-cooling. The duration of the MGI pre-cooling is roughly a half of the corresponding phase in the moderate puff, although the latter is already cooled and undergoes an instable condition, in which the energy confinement is affected (note that only the pre-cooling phase is shown in Figure VI.2).

Review: Moderate and distant - massive and close injection cases
Though the moderate puff of 0.18 bar l, or 4.5×10^{21} atoms forms a radiation front, it subsequently expires and does not induce a rapid shut down. On the contrary, charging the valve with higher pressures (3.3 bar l, or 8×10^{22} particles) and reducing the distance between plasma and nozzle ($\approx$ 13 cm), we clearly induce a thermal quench after a short duration, in the presented case, the delay amounts 2.2 ms. The disruption is identified using soft X-ray and magnetic fluctuations known to represent the quench phase[2]. The density rises shortly before the thermal quench and goes up during the quenching. Throughout this section, it will emerge that also amongst the MGI shut downs listed in Table VI.1, differences of the radiation front behaviour in the pre-cooling phase appear.

VI.2 Overview of discharge parameters

The used sorts of gas, the plasma and impurity jet parameters are listed in Table VI.1. Generally, the pulses were operated in the ELMy H-mode regime and the toroidal field B_Φ amounts to -2.5 T, the opening time of the valve is at t_{tr}=2.98 s and the gas reservoir is $V_{\mathrm{r}} = 80\,\mathrm{cm}^3$. The heating beams are not switched off before the gas injection but keep on heating until the end.

It is noticed with regard to Table VI.1 that the choice of B_Φ and consequently q_{95} was restricted to a small variation to allow for ECRH heating during the current ramp-up[3]. Scans of q_{95}, as they were performed in e. g. TEXTOR, were thus not possible. Although comparable standard H-modes were used, differences in core and edge conditions are noticed: In #24399, #23306 and #23307, the injection was triggered during the occurrence of an ELM. No significant core mode activity was there in #24442, #24491 and #24398. However, different characteristics between shut down scenarios - in terms of all the evaluated measures - could not distinctively be attributed to MHD activity present during the flat top period until t_{tr}.

[2]We use the wording 'quench phase' for including both thermal and current quench. They partly overlap (Section III.4.5)

[3]The so-called ECRH assist (electron cyclotron heating) during the current ramp-up limits the adjustment of B_Φ.

	p_r (MPa)	I_p (MA)	$(P_{NBI} + P_{ECRF})$ (MW)+(MW)	E_{th} (kJ)	q_{95}	F_{eff}
Neon puff						
23304	0.49	0.8	5.0 + 0.0	430	5.2	0.32
24395	0.54	1	4.8 + 1.4	500	4.5	0.26
24399	1.1	1	9.6 + 1.4	648	4.5	0.21
24396	4.2	1	9.6 + 1.4	756	4.5	0.13
24442	4.4	1	2.5 + 0.7	369	4.5	0.20
24480	4.1	1	9.8 + 1.5	743	4.5	0.18
24491	3.9	1	2.5 + 0.8	383	4.5	0.22
He puff						
23308	0.17	0.8	5.0 + 0.0	413	5.2	0.24
23307	0.27	0.8	5.0 + 0.0	423	5.2	-
23306	1.7	0.8	5.0 + 0.0	418	5.2	0.39
24398	4.2	1	7.3 + 1.4	545	4.5	0.29
Ar puff						
24419	0.34	0.8	4.7 + 1.3	489	5.6	<0.1
24420	0.81	0.8	4.7 + 1.3	410	5.7	<0.1

Table VI.1: Discharge parameters of dedicated massive gas injection experiments (MGI) at $t_{tr} = 2.98\,s$. The symbols p_r, P_{NBI} and P_{ECRF} stand for the initial pressure in the impurity reservoir (denoted by *reservoir pressure*) and the heating power supplied by the NBI and ECRH systems, respectively. Fuelling efficiency $F_{eff} = \frac{\Delta n_e}{n_{inj}}$, the ratio between the increase of the total number of free electrons Δn_e and the total number of injected gas atoms n_{inj}. The implications of F_{eff} data are consulted in Chapter VII. F_{eff} data courtesy by Dr. G. Pautasso.

VI.3 Toroidal and radial impurity propagation

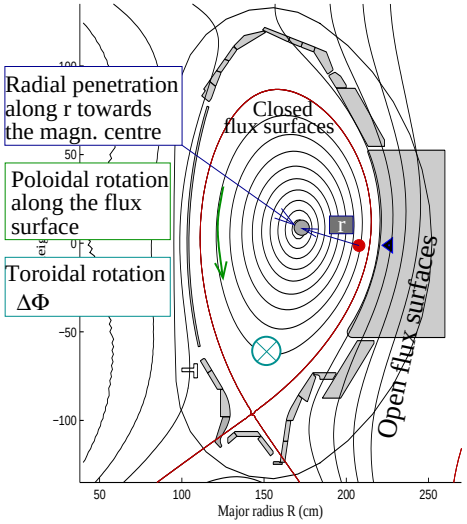

Figure VI.3: Definitions of *radial, poloidal* and *toroidal* movement.

In following sections, the terms *radial, poloidal, toroidal* and *helical* will often be used for the penetration or rotation direction of radiation structures. The neighbouring Figure VI.3 illustrates those directions. 'Radial' penetration concerns the minor radius r and means towards the magnetic centre. We will also consider horizontal penetration across the flux surfaces. 'Poloidal' propagation or rotation is along flux surfaces in a poloidal plane. 'Toroidal' movement applies generally to a transport around the torus. Superimposing the toroidal transport with a poloidal movement, the propagation is in 'helical' direction.

VI.3.1 Latency times

The delay in between the initial radiation responses at $\Phi = 0$ and $\Phi = \pi$ is evaluated using the XUV stereo measurement. From the nozzle opening trigger on until an initial radiative response in the plasma periphery in front of the valve ($\Phi = 0$), the cooling of the plasma is delayed with the latency time τ^0_{lat}. It consists of a possible trigger uncertainty, of an opening delay and of the time of flight of the impurities. The superscript denotes the toroidal position $\Phi = 0$. Also at $\Phi = \pi$, a delay is defined and consistently denoted by τ^π_{lat}. The difference of the two latency times is described by τ_{tor}, which gives the travelling time of the ions half a torus around. The shortest τ^0_{lat} achieved by the MGI valve was found to be only 350 μs, the longest was 740 μs. The latency times and the resulting toroidal response delays are shown in Figure VI.4. The circles mark the latency times: The lower is symbolised by τ^0_{lat}, the upper is τ^π_{lat}. The connecting line represents the toroidal response delay $\tau_{\mathrm{tor}} = \tau^\pi_{\mathrm{lat}} - \tau^0_{\mathrm{lat}}$. The latency times range in between 350 μs (τ^0_{lat}) and 1100 μs (τ^π_{lat}) - the values for τ_{tor} from 78 μs to 280 μs.

Figure VI.4 presents τ_{tor} in three different diagrams, where it is plotted versus various jet or plasma parameters in order to find possible relations. In the leftmost box, the latency times are plotted versus the reservoir pressure p_{r}. Due to the same reservoir volume used in all the shut downs presented here, p_{r} is proportional to the number of injected atoms n_{inj}. A higher cooling rate is expectable in case of a higher amount of

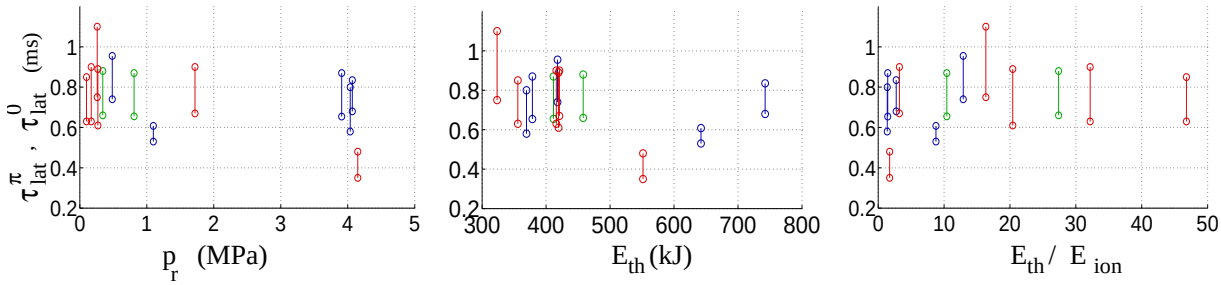

Figure VI.4: Latency times and toroidal response delay.
The lower circle marks τ^0_{lat}, the upper one τ^π_{lat}. The length of the connecting line symbolises τ_{tor}. The same latencies are plotted versus three different parameters (for $E_{\mathrm{th}}/E_{\mathrm{ion}}$ see Equation VI.1). Colouring: Argon in green, neon in blue and helium in red.

impurities injected per time unit. If this happened in a significant magnitude before the impurities reach $\Phi = \pi$, the transport via ionic sound velocity, which is proportional to the temperature as $v_{\mathrm{s,ion}} \propto \sqrt{T_{\mathrm{ion}}}$, would be reduced resulting in a longer τ_{tor}. Then, the plot would reveal such an effect by an increasing distance between lower and upper circle at higher pressures. This, however, is not revealed by the plots.

Another topic is the self-shielding mechanism, which is observed in pellet injection experiments [70]. That effect restrains the expansion of the ablated impurities around the pellet. If a higher pressure p_{r} in MGI maintained such a self-shielding effect by causing a stronger cooling, τ_{tor} would be dependent on p_{r}. Yet, again this is not seen in the plots.

As a next, the $E_{\mathrm{th}}-$axis used in the central plotting is considered: The edge temperature is proportional to E_{th} and it is a reasonable assumption that the toroidal transport of impurities could be faster if the plasma edge would be hotter due to the above noted relation between ionic sound velocity and temperature. This could possibly the case. However, the small amount of high-energy shut downs prevent from making substantiated conclusions.

The third plot accounts for the combination of E_{th}, n_{inj} and the ionisation energy $\Delta\epsilon_{\mathrm{ion}}$ necessary for producing a singly charged ion. The product, as written in Equation VI.1, gives the energy consumption for producing singly ionised impurities. It reads as

$$\frac{E_{\mathrm{th}}}{E_{\mathrm{ion}}} = \frac{E_{\mathrm{th}}(t^* < t_{\mathrm{tr}})}{n_{\mathrm{inj}}\Delta\epsilon_{\mathrm{ion}}}. \tag{VI.1}$$

If there was a high amount of energy available for ionising the atoms, one must inject more particles for introducing such debilitating effects on toroidal impurity transportation noted for the first and second plots.

However, the result is that none of these parameters influences the latency times, as it can be seen in Figure VI.4. Neither τ_{tor}, nor the first latency τ^0_{lat} seem to be functions of the

considered $x-$axes. The first latency actually poses the question, why it is not influenced by the time of flight τ_{tof} of the different atomic species. This is the topic of the following subsection.

VI.3.2 Mach number

The above-presented latency times τ^0_{lat} in Figure VI.4, are independent on the mass of the species. This is surprising, because at least $v_{\mathrm{tof}} \propto \sqrt{M}^{-1}$ should hold (v_{tof} is the time of flight of the impurity atom of mass M). This issue is considered in detail in the following by taking the geometries of the diagnostic views, the plasma and the valve into account. The considerations include the localisation of the initial interaction zone, the estimation of the size, the deduction of the Mach number and finally the evaluation of the opening time jitter on the basis of the inferred supersonic flow velocity.

The size of the initial radiation spot is inferable from the fact that only one detector view shows the initial response. In a close-up view, Figure VI.5 illustrates the initial response and the time scale involved. In this subsection, the initial response is discussed.

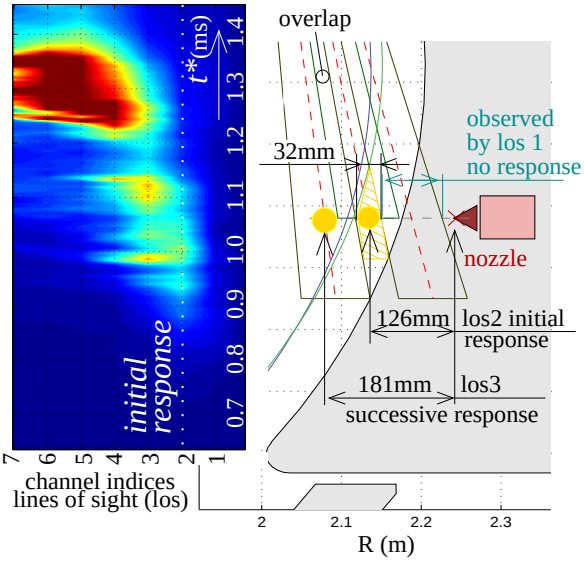

Figure VI.5: Close-up scheme of the plasma edge at $\Phi = 0$, Ne shut down #24480. Left: XUV measurement signals: Time versus channels ($t^* = 0$ at $t = 2.98$). Right: Line of sight geometry.

The first detector, which responds on the impurity injection is channel 2. In the right part of the neighbouring figure, the according geometry is shown: Channel 1 (line of sight no. 1) is the outermost one almost tangenting the nozzle. About 1/3 of its extension is overlapped with the neighbouring channel 2. The latter, again, overlaps with the third. The overlap-free region is marked by the yellow hatching. The horizontal extension of the overlap-free region on the horizontal projection of the gas jet is of only 3.2 cm. Symmetrically, the two neighbouring channels are illuminated more and more in time, which features the expansion of the radiation source. This happens in the space between nozzle and separatrix, because the dominant radiation does not change

to channel 3 for the duration of about 300 μs (it enters the next channel view after $t^* = 920\,\mu$s). Two separatrices are drawn. They constitute the delimitations to the outermost and innermost plasma column positioning with respect to the analysed discharges (Table VI.1). They differ to an extent, which is below the spatial resolution of the diagnostic. The measures inserted constitute the distances from the nozzle to the position of initial response. This requires that the first response happens at the horizontal projection of the nozzle axis. Due to the fact that the lines of sight overlap quite a lot ($\approx 1/3$), they provide for a relative good spatial resolution in the plasma edge. If only one detector is illuminated, the radiation source would consequentially be smaller than the maximal extension of the overlap-free region. The horizontal dimension of the overlap free region at the vertical position of the gas valve is (maximum) 3.5 cm for channel 2. The geometry considerations allow to conclude that the initial response occurs outside the separatrix within the scrape-off layer. The geometry is applied in the following to evaluate the neutrals velocities.

The hatched yellow area in Figure VI.5 has a vertical expansion of approximately 90 mm up and down. The distance between nozzle exit and response area is 126 mm. We infer from this a Mach number of 1.4 by just taking the inverse of the half extension of the Mach cone. This leads us to the velocity of the neutrals by

$$v_\mathrm{n} \;=\; \frac{126}{90}\, c_\mathrm{n} \tag{VI.2}$$

where c_n is the sound velocity of the neutrals at room temperature.

The t_tr-inaccuracy of the valve from discharge to discharge, which is denoted as valve jitter in what follows, can now be evaluated for understanding the large deviation of τ^0_lat in Figure VI.4 amongst the shut downs: In principle, Ar should take longer than Ne for travelling the nozzle-plasma distance. However, comparing Ar#24420 and Ne#24480, it turns out that argon approaches the SOL earlier than neon. This is explainable by the valve opening uncertainty. We fix the time of flight, denoted by τ_tof by the above-made estimation of the Mach number.

$$\tau_\mathrm{tof} \;=\; \frac{90\,\mathrm{mm}}{\sqrt{\gamma\,\frac{RT}{M_\mathrm{n}}}}, \tag{VI.3}$$

where the 90 mm results from dividing the distance between nozzle and point of first response by the Mach number of 1.4. Equation VI.3 results[4] in $\tau^\mathrm{Ne}_\mathrm{tof} = 277\,\mu$s and a $\tau^\mathrm{Ar}_\mathrm{tof} = 390\,\mu$s, which are the times flight for neon and argon, respectively.

The measured latency times τ_lat for the argon injection is 620 μs, in neon $\tau^\mathrm{Ne}_\mathrm{lat}$ amounts to 676 μs. The argon case marks the lower boundary of the jitter by

$$\min(\tau_\mathrm{jitter}) \,:\, \tau^\mathrm{Ar}_\mathrm{lat} \,-\, \tau^\mathrm{Ar}_\mathrm{tof} \;=\; 230\,\mu\mathrm{s}, \tag{VI.4}$$

[4] R is the gas constant, γ the adiabatic coefficient and T being room temperature.

and the largest possible jitter is derived from the neon case by

$$\max(\tau_{\text{jitter}}) \,:\, \tau_{\text{lat}}^{\text{Ne}} \,-\, \tau_{\text{tof}}^{\text{Ne}} \;=\; 400\,\mu\text{s}. \tag{VI.5}$$

The valve trigger jitters in between $\min(\tau_{\text{jitter}})$ and $\max(\tau_{\text{jitter}})$ in a range of $170\,\mu$s. This means that the lower circle in Figure VI.4, which constitutes the latency times of the different injection scenarios at $\Phi = 0$, is affected by an uncertainty of $+/-\,85\,\mu$s - under the assumptions of a supersonic jet of Ma $=$ 1.4 for argon as well as neon neglecting different viscosities in the nozzle exit, shocks within the reservoir, etc. Aside from this, we assumed that both neutrals get immediately ionised when they enter the view of channel 2. And finally we assumed that the neutral is ionised at the distance of 126 mm from the nozzle exit.

Conclusively, the evaluated valve opening jitter of $\pm 85\,\mu$s is a reasonable technical uncertainty, which is in fact small but nevertheless, it introduces a large scatter in Figure VI.4 for τ_{tor}^{0}.

VI.3.3 Methodological discussions: Initial response

The above-made observations are summarised and further developed with respect to the physical background.

The interaction zone in the nozzle vicinity is initially formed outside the separatrix in the SOL. The gas valve is opened, a neutral gas front arrives at the plasma edge with a delay time (latency) given by the nozzle-plasma distance and the respective neutrals velocity. A disc-shaped interaction zone is formed with about 10 cm diameter according to the angular jet divergence. The zone is of about 3.5 cm radial extension. The arriving atoms are ionised within an ionisation mean free path and the density rises, which causes a decrease in penetration depth of subsequently arriving neutrals. In parallel, the temperature is dropping in this narrow layer by atomic processes like radiation losses. The fast influx of energy along magnetic field lines due to the electron heat conduction counteracts the energy loss. If the density rise is strong and the temperature decrease small, then the pressure in the interaction zone may increase and it starts to expand along field lines as it is the case in cryogenic hydrogen pellet injections. The expansion speed is weakly or even independent on reservoir pressure as depicted by Figure VI.4. The same independence applies to the thermal plasma energy or the impurity ionisation energy. Also an impurity mass dependency is absent. At a first glance, at least the latter is astonishing due to the inverse square root mass dependency of the ion velocity. We focus on this issue below.

Pressure gradient driven B-parallel transport:
The toroidal delay τ_{tor} of the ion approach is measured by the XUV stereo measurement.

Assuming that the particles are travelling along magnetic field lines, the distance between the measurement positions is $L = 5.8\,\mathrm{m}$. Several later examples substantiate this assumption (albeit only in the initial response sequence). We consult XUV data from three shut downs of comparable E_{th} content but different gases and infer the toroidal cooling front expansion velocity by $v_{\mathrm{hel}} = \tau_{\mathrm{tor}} \,/\, L$:

$v_{\mathrm{hel}}^{\mathrm{Ar}} = 25.2\,\frac{km}{s}$ (#24420)
$v_{\mathrm{hel}}^{\mathrm{Ne}} = 27.6\,\frac{km}{s}$ (#24491)
$v_{\mathrm{hel}}^{\mathrm{He}} = 36.3\,\frac{km}{s}$ (#24398)

The velocities do not differ dramatically from each other. The question is, what is the ionisation degree. In case of no ionisation, one expects a mass dependent relation ($v_{\mathrm{atom}} \propto \sqrt{M_{\mathrm{atom}}}^{-1}$). Contrarily, ionisation produces an electron pressure rise. We assume that it is more significant than the temperature decrease, because we regard the very beginning of the shut down scenario, in which the energy supply into the zone is well sustained (temperature is sufficient for providing ionisation energy). And we assume that the pressure in the interaction zone interior is much higher than the background pressure. As a consequence, the B-parallel impurity flow is driven by the electron pressure p_{e}. The impurity ions evolve with sound velocity helically in B-parallel direction. The sound velocity c_{s} in a plasma of electrons and ions is given as [4]

$$c_{\mathrm{s}} = \sqrt{\gamma \frac{p_{\mathrm{e}} + p_{\mathrm{i}}}{\rho}} \tag{VI.6}$$

We claim that impurities are majorities such that the contribution of hydrogen is negligible. The number of charges n_{z} of the charge stage z and temperature T_{z} determine the sound velocity of the ion-electron fluid as

$$c_{\mathrm{s}} = \sqrt{\gamma \frac{n_{\mathrm{z}}\, T_{\mathrm{z}} + (n_{\mathrm{z}} \cdot z)\, T_{\mathrm{e}}}{n_{\mathrm{z}}\, m_{\mathrm{z}}}}, \tag{VI.7}$$

where we presuppose Debye shielding. With $T_{\mathrm{z}} = T_{\mathrm{e}} = T$, which is fulfilled in a dense plasma of short collision times, n_{z} cancels and we write

$$c_{\mathrm{s}} = \sqrt{\gamma \frac{(1+z)\, T}{m_{\mathrm{z}}}} \tag{VI.8}$$

The factor $(1+z)$ originates from the dominant electron pressure contribution ($z > 1$). This simple model explains well the unexpected weak variation of toroidal expansion with impurity mass.

An equivalent temperature is obtained by

$$T_{\mathrm{eq}} = \frac{m_{\mathrm{z}}}{(1+z)\,\gamma} \cdot v_{\mathrm{hel}}^2, \tag{VI.9}$$

where $v_{\rm hel} = c_{\rm s}$. For neon and argon, z might be strongly dependent on the distance between nozzle and ion. With the adiabatic coefficient of $\gamma = 5/3$ for these high collisionality conditions, the equivalent temperatures are listed as

$$T_{\rm eq}^{\rm Ar} = 158\,\frac{1}{(1+z)}\,{\rm eV},$$
$$T_{\rm eq}^{\rm Ne} = 93\,\frac{1}{(1+z)}\,{\rm eV},$$
$$T_{\rm eq}^{\rm He} = 33\,\frac{1}{(1+z)}\,{\rm eV},$$

for the three cases from above. Certainly, the composition of ionisation stages and henceforth, the effective charge stage z, is a function of the temperature T and density $n_{\rm z}$. Therefore, it varies in space and time and is, in principle, unknown. Yet, we may still consider qualitative numbers. For helium averaged along field lines around the torus, it should clearly range in between He^{1+} and He^{2+}. For neon and argon, the effective local charge might strongly increase with the toroidal distance from the nozzle, with the spatial average along field lines well above the one of helium. Argon may be of highest, neon of intermittent charge state. Reasonable numbers for the charge state inserted give a plausible average of the temperature in the interaction zone. Low temperatures in the edge are qualitatively consistent with the radiation curves shown in Figure II.4. The discussion above shows also that impurity transport is necessarily due to ion sound propagation. The neutrals outside the plasma can not directly reach the toroidally opposed side. They will be reflected from the plasma by elastic or charge exchange collisions. Even those starting about tangentially will hit the plasma after wall reflection and will be finally ionised in the nozzle vicinity after a few wall-plasma reflection cycles.

VI.3.4 Penetration depth

In the following, the radial penetration of the radiation front at the two toroidally spaced measurement positions is investigated.

Definitions

At the toroidal position where the valve is situated ($\Phi = 0$), only one fan of lines of sight is present ($XUV^{\Phi=0}$). Tomography is therefore not possible at this position. We thus have to consider the line of sight geometry and the shape of the radiation front. This is important for interpreting the radiation front movement correctly. The fan views the gas jet from above. This implies that a horizontal penetration into the plasma is well resolved, whereas an elongation of the radiation front along a magnetic flux surface like a half-moon is not directly identifyable. Moreover, such a half-moon like expansion would be indistinguishable from a purely radially penetrating radiation front. However, the sharp track in Figure VI.2, which represents the radiation front, implies that the radiation front is a very pronounced and spatially constricted structure. For the first some hundreds of microseconds, a half-moon shaped elongation is barely conceivable, because in such a case, at

least three or four channels[5] would be illuminated as it is the case in the moderate puffing scenario. The argumentation is comprehensible by considering the close-up drawing in Figure VI.5, where it becomes clear that the slightly inclined view geometry would depict an elongated half-moon in several channels. The same figure reveals that in a later stage ($t^* \geq 1.2\,\mathrm{ms}$), such a half-moon might be formed, because for short time slices, up to three channels are illuminated. Regarding the plasma topology: In order to find out, whether the radiation front indeed penetrates into the plasma interior or the plasma boundary just moves away from the nozzle, the magnetic plasma topology has to be taken into account. For this purpose, we trace the radiation front versus the magnetic flux coordinate q. The coordinate was introduced in Chapter II. Figure VI.6 demonstrates that the deformation or movement of the magnetic topology during the pre-cooling phase is in fact large: The magenta line constitutes the separatrix at the time of the initial radiative response - the red line is the separatrix at the end of the pre-cooling phase. In what follows, magnetic reconstructions are applied, which have a non-standard time resolution of $100\,\mu\mathrm{s}$. These equilibria are interpolated according to the XUV time resolution of $2\,\mu\mathrm{s}$.

$q(t)$ at $\Phi = 0$: q^0

Figure VI.6 shows the principle of finding the q^0-axis, on which the radiation front moves inwards. Consider the scheme on the left: The blue separatrix corresponds to the starting point of the radiation front movement. The front is symbolised by the blue dot. The

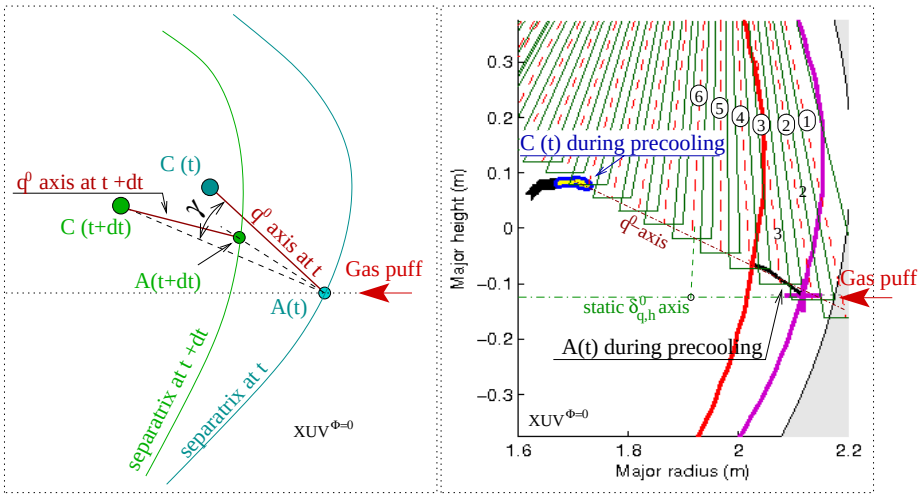

Figure VI.6: Schematic illustration of definition at $\Phi = 0$. The magnetic centre is denoted by C at the time t. The intersection point of the reference axis with the separatrix is denoted by A.

magnetic centre is symbolised by C (blue for the starting time). The red connection line of $A(t)$ with $C(t)$ is the first q^0 axis, which means that the intersection points of the lines

[5]Lines of sight are often denoted by channels in what follows

of sight with this axis are mapped to the q topology of time t. In the scheme on the right, the lines of sight are cut at those intersection points. In this sense, the intersection points - and thus the lines of sight - are labelled with q values. Tracing the line of sight signals versus those q values yields a radiation front profile versus q. This is done in the subsequent figures, which are explained later. Before, regard again the left scheme in Figure VI.6.

We find the successive q^0-axis: The green coloured elements in the scheme correspond to the equilibrium at $t+\mathrm{d}t$ ($2\,\mu$s later). The penetration direction of impurities, which reside in the radiation front, is of diffusive kind with a strong influence of the temperature and density gradients. We therefore assume that the radiation front moves radially towards the plasma centre. Two furthermore reasonable possibilities are, firstly, the poloidal expansion into a half-moon like shape and, secondly, a horizontal penetration. Both possibilities are included in a later section. Here, we illustrate exclusively the radial penetration and remark the deviation between radial and horizontal penetration in terms of a q uncertainty. The half-moon shape is not of any value here, whereas it is important in later discussions on the toroidal evolution.

In a radial penetration, the radiation front moves from $A(t)$ to $C(t+\mathrm{d}t)$. Since we do not know, when the plasma topology moves during $\mathrm{d}t$, we assume that the radiation front is dragged along the bisector in between $[A(t)C(t)]$ and $[A(t)C(t+\mathrm{d}t)]$. We draw a line along this bisector and obtain - at the intersection point with the green separatrix - the new radiation front position, $A(t+\mathrm{d}t)$.

$q(t)$ at $\Phi=\pi$: q^π

The cooling front position is derived from the 2-D radiation profiles generated with the maximum entropy tomography method. The $q-$value of the pixel with the highest emissivity at the respective time is indicated and pixels at a lower q are selected. This method identifies the falling edge of the cooling front towards a lower q. Therefore, some plots are halved in the following presentations. The radiation front is represented by the envelope of the blue dots. The envelope steepens and moves during the pre-cooling phase.

Explanation of Figure VI.7 and Figure VI.8: Both figures show $q^0(t)$ as well as $q^\pi(t)$. The emissivity is given in different units:

red: At $\Phi=0$: line integral measurements in radiant flux density

blue: At $\Phi=\pi$: radiant flux density per pixel area

Outside the separatrix, q is not defined. Possibly occurring artifacts from tomography thus are masked out from contributing to the radiation front profile at $\Phi=\pi$. Mainly, artifacts occur in the vicinity of the wall (see black cross inserted in the tomography in Figure VI.2 and discussions on artefacts in Chapter V). For interpreting the δ_{q}^0 profiles, the reader is referred to the time markers in the contour chart on the upper right, while

the profiles for δ_q^π can be reconsidered with the tomograms accordingly inserted on the right hand side of each profile graph. On the upper right, I_p and E_{th} and in the middle, two central soft X-ray signals from different toroidal locations are plotted. The time window includes the full duration of pre-cooling plus an initial sequence of the thermal quench. The exact starting time of thermal quench is marked in the soft X-ray plotting (see top row, in the middle): The graph labelled by *'soft X core'* gives the $q-$position of the maximal soft X-ray emission, which implies the location of the core plasma. The curve starts to fluctuate in between high and low q, when soft X-rays occasionally appear in arbitrary regions in the vessel. It hints at a stochastisation of the field lines. (The graph was generated with the aid of tomography.)

Toroidal penetration asymmetry

The series of radiation front profiles versus the plasma topology coordinate q, reveals the time history of the radiation front evolution in front of the valve and at the opposed position. The radiation front steepening is nicely featured and the toroidal asymmetry of the radiation front positions depicted. Note that radiation front penetration means an evolution to lower q-values (see Chapter II, definition of q).

Explanation of the pre-cooling in helium, Figure VI.7:

Frame α shows the radiation distribution at t_{tr}, meaning the conditions before the first response[6]. The distribution is typical for discharges in standard H-mode operation. Regarding the profile plots: The red graph shows the line of sight signals at $\Phi = 0$ versus $q^0(t_{tr})$. The blue dots are the pixel emissivities from tomography at $\Phi = \pi$. Considering first the red graph: It peaks at a low q^0. This, however, is misinterpreted as central radiation, because the top view geometry views the centre and the divertor simultaneously. The divertor appears usually as the brightest region for a broadband detector in a standard H-mode discharge. We conclude, the red graphs are valid not before the impurity radiation exceeds the divertor brightness. Nevertheless, frame α is shown for providing a reference for comparisons of the usual emissivities and the bright luminosities in an MGI shut down. In Frame β, the $\Phi = 0-$profile is valid, because the first impurities arrive at the plasma edge and introduce a significant edge radiation. The red profile is maximal at the q of the separatrix (q_{sep}). Note $q > q_{sep}$ is not defined, which means that radiation in the SOL is not included here. However, the important information is that the radiation front is formed in front of the valve with emissivities of about 6 times higher than the usual divertor radiation, but toroidally π around, the profile remains unchanged. This is also the case $100\,\mu$s later in frame γ, while the emissivity in front of the valve increases further by a factor of 2.

[6]Note, all the tomograms shown in the following are maximum entropy reconstructions without any boundary conditions.

In frame δ, 200 μs later, impurities are present in the full torus extension seen in the enhanced emissivities at $\Phi = \pi$ though only a slight increase of about +20 % is noted. A significant steepening is not the case. The cooling front at $\Phi = 0$ still remains outside the $q = 2$ surface and shows its maximum at $q > 3$. At ε or $t^* = 1$ ms, the cooling front at $\Phi = 0$ gets steepened on the approach of $q = 2$, while toroidally around, the profile is quite flat. Not before $t^* = 1.2$ ms, also there a steepening is observed. The blue profile shifts from now on subsequently towards $q = 2$ but does not reach this surface within the pre-cooling. Contrarily, the cooling front at $\Phi = 0$: At $t^* = 1.6$ ms or frame Θ, the impurities clearly are observed in the core. From this time on, soft X-ray emissivity falls and after furthermore 200 μs, the thermal quench is triggered. More details on the trigger of the thermal quench are given in Subsection VI.5.1.

Precooling in neon, Figure VI.8:

Again, frame α shows the ELM occurrence in form of the peaked red graph, which is misinterpreted to be at a low q. Regarding the full frame series, the two graphs for the stereo measurement correspond more to each other than in the case for helium. Up to Frame ζ, the deviation between them lies in the range of the $q-$ resolution. From this frame on however, the cooling front at $\Phi = 0$ is clearly closer to the centre as the other one. Also here, a discussion on the thermal quench trigger is carried on in Subsection VI.5.1.

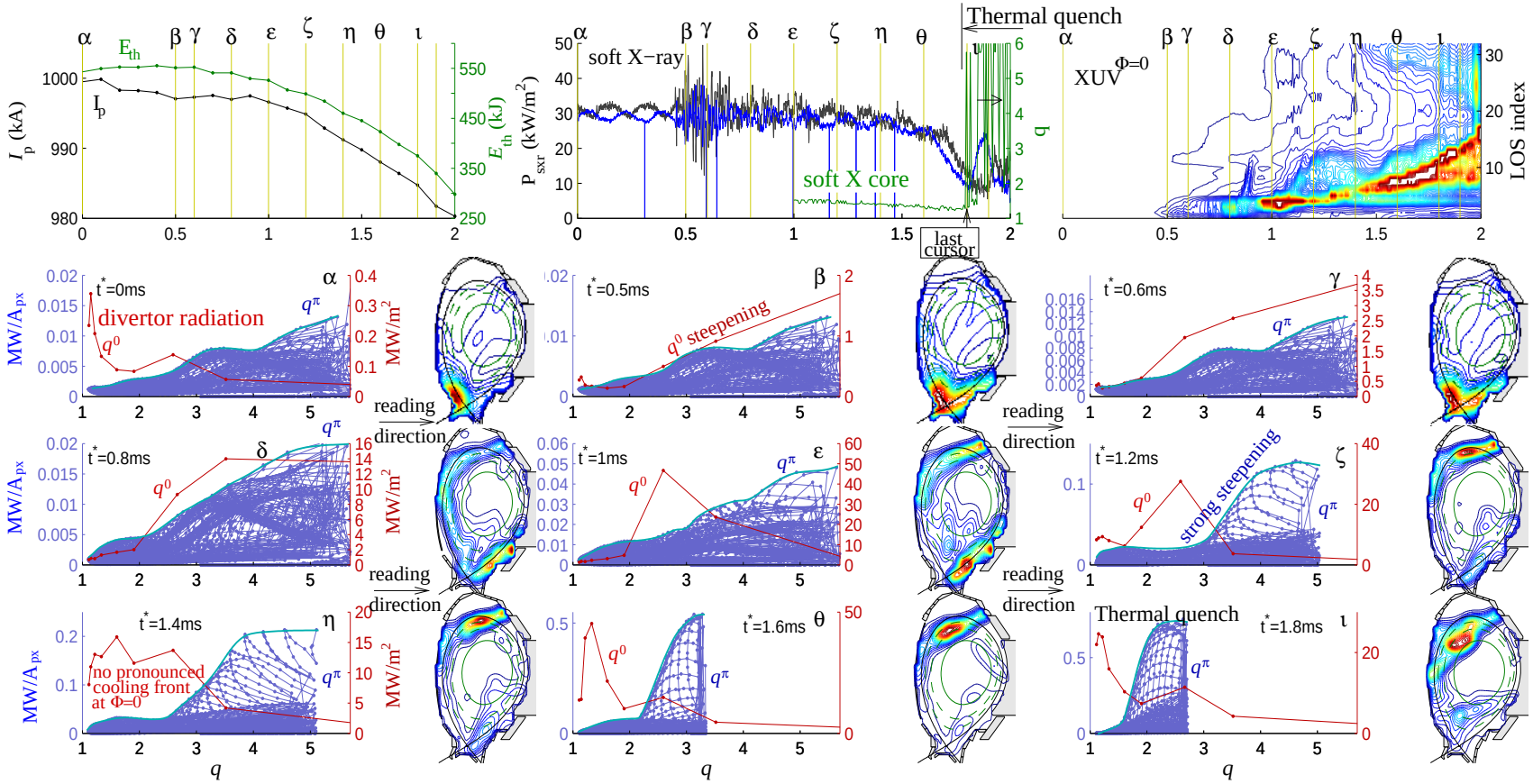

Figure VI.7: Cooling front penetration during massive helium injection (#24398). In the upper row: On the left, I_p and E_th, in the middle soft X-ray signals of central lines of sight at two different toroidal positions ($\Delta\Phi = 158°$) and on the right, an $XUV^{\Phi=0}$ contour is presented. The yellow lines mark the snapshot times from $\alpha \rightarrow \iota$. The tomographies correspond to the profile plots on the left.

Radiation front at $\Phi = 0$ versus q^0: Red line, emission profile of $XUV^{\Phi=0}$. Radiation front at $\Phi = \pi$ versus q^π: Blue envelope of pixel emissivities in units MW per area, $XUV^{\Phi=\pi}$.

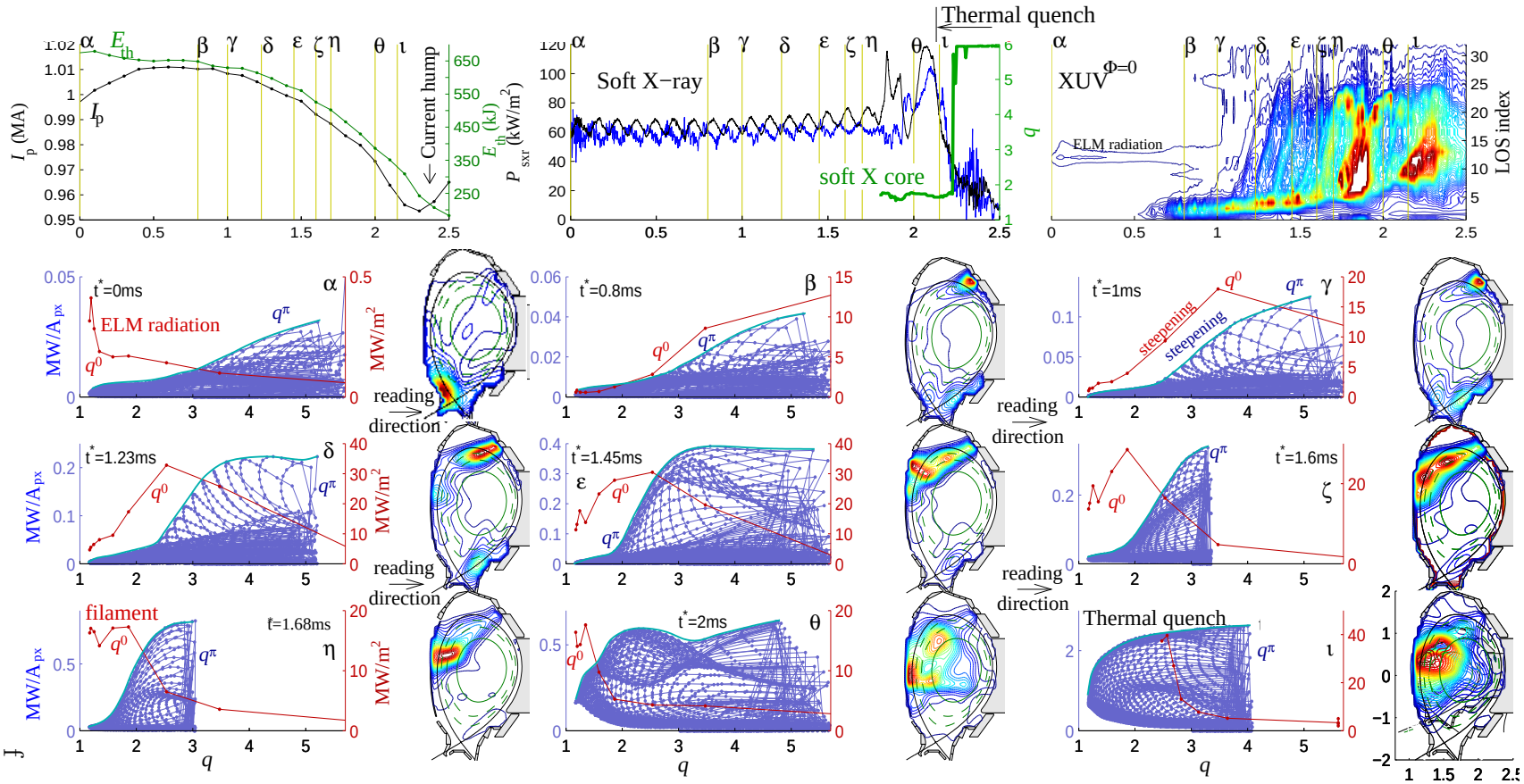

Figure VI.8: Cooling front penetration during massive helium injection (#24398). In the upper row: On the left, I_p and E_th, in the middle soft X-ray signals of central lines of sight at two different toroidal positions ($\Delta\Phi = 158°$) and on the right, an $XUV^{\Phi=0}$ contour is presented. The yellow lines mark the snapshot times from $\alpha \rightarrow \iota$. The tomographies correspond to the profile plots on the left.

Radiation front at $\Phi = 0$ versus q^0: Red line, emission profile of $XUV^{\Phi=0}$. Radiation front at $\Phi = \pi$ versus q^π: Blue envelope of pixel emissivities in units MW per area, $XUV^{\Phi=\pi}$.

Cross validation of radiation structure and magnetic field lines

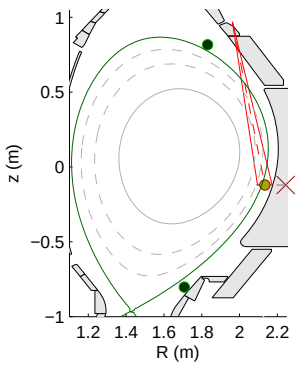

Figure VI.9: Initial response: Field line intersection points (see explanation on the side)

In Subsection VI.3.3, discussions on the early stage in pre-cooling were already performed. It was assumed that the ions travel along the magnetic field lines. We challenge this assumption in the neighbouring figure: The position of the initial response is marked by the yellow dot. We follow now the helical pathway of the particular magnetic field line, which intersects this dot. Toroidally half around, at the location of $XUV^{\Phi=\pi}$, we arrive at the positions marked by the green dots[a]. Channel 2 is also drawn - it detects the initial response.

[a]The magnetic field intersects the poloidal plane at $\Phi = \pi$ at two positions, because the field line points into as well as out of the paper plane.

The occurrence of radiating impurities at $\Phi = \pi$ is in fact demonstrated by $XUV^{\Phi=\pi}$ around those positions predicted by magnetic field-line tracing. Examples are shown in Figure VI.8, VI.7. In both, it is referred to the series from frame β and γ, which reproduces the radiation appearance around the lower as well as the upper position. In both figures, the H-mode typical radiation close to the inner divertor becomes weaker and is predominated by those gas jet related emission sources. At both positions however, XUV has a low spatial resolution, which causes inaccuracies as discussed earlier in Chapter V. Nevertheless, single line of sight signals show the response clearly in those regions.

Helical impurity transport along magnetic field lines in a very first instance is certainly the case. Yet, later stages exhibit different characteristics: Figure VI.10 reconsiders the neon shut down from Figure VI.8 in combination with magnetic field line information (see figure caption). We include a CMOS frame, which gives a spatial impression of the interaction zone during the pre-cooling phase. The disc-shaped interaction zone, as described in regard of the initial response, has distorted and expands in toroidal direction, whereas the vertical constriction still applies. In the following, we combine the XUV stereomeasurement with the magnetic surface information in order to find out, whether the impurity trajectories correspond to the pathways of magnetic field lines.

Let us consider the front in the poloidal cross-sectional view, where we clearly observe the interaction zone with an $XUV^{\Phi=0}$ channel from above[7]. This channel is inserted in the images in Figure VI.10. Recall that the position of the radiation source is not locatable along the line of sight - the source lies somewhere in the view geometry. Therefore, we assume the following: A half-moon shaped front could be formed. We put the lower cap of

[7]We select the channel of highest amplitude.

the moon onto the horizontal projection from the nozzle (see Figure VI.10, green dot). The upper cap is set onto a position, which is the most reasonable location under consideration of the radiation location at $\Phi = \pi$. The location of the red dot is selected such that we approach the radiation at $\Phi = \pi$ most accurately after following the magnetic field[8] line half around the torus to $XUV^{\Phi=\pi}$. The boundary condition for selecting locations of the radiation source at $\Phi = 0$ is that the radiation source must lie within the view of the inserted channel.

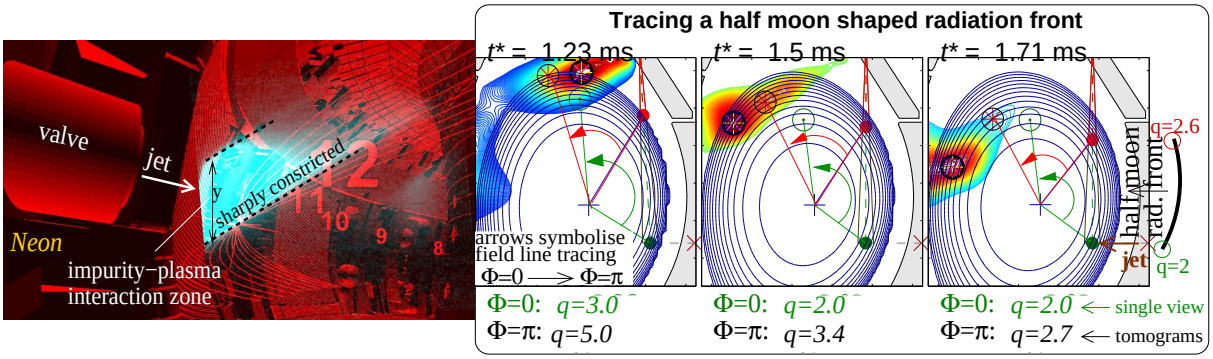

Figure VI.10: CMOS camera snapshot of interaction zone in front of the valve on the left. Right, a correspondence analysis of the toroidal stereo XUV measurement with magnetic field lines (#24399). The inserted channel observes the radiation front at $\Phi = 0$.
Green point: Radiation front position at $\Phi = 0$.
Red point: Upper end of the radiation front if it would expand in a half-moon like shape.
Both points are traced helically around to the $XUV^{\Phi=\pi}$ plane. The points intersect the poloidal plane at the correspondingly coloured symbols.
Thick encircled cross: Radiation maximum given by the tomogram. Its $q-$position is given on the bottom in black.

For clarifying the question, whether a time delay between impurity positions at $\Phi = \pi$ and $\Phi = 0$ is the case, three images, which are temporally spaced with about 200 μs, are shown on the right in Figure VI.10. Consider the image at $t^* = 1.23$ ms: We trace the field line, which corresponds to the green point, helically around and find the corresponding point in the $XUV^{\Phi=\pi}$ plane. It is radially further inside located than the radiation maximum given by the tomogram. This is indeed not very surprising, because we know that the $XUV^{\Phi=\pi}$ dynamics are delayed with a certain latency. As a second point, we trace the upper cap of the half-moon around. It arises at the same q-coordinate as given by $XUV^{\Phi=\pi}$ tomogram albeit it is poloidally shifted to the high field side. We conclude from the first image that the radiation at $\Phi = 0$ does not correspond to the radiation at $\Phi = \pi$ at the same time $t^* = 1.23$ ms.

[8]The field line, which intersects the red dot at $\Phi = 0$.

Whether a later radiation front position at $\Phi = 0$ corresponds to an earlier radiation front position at $\Phi = \pi$ is questioned in the following. The image at $t^* = 1.5\,\mathrm{ms}$ shows that the radiation given by the $XUV^{\Phi=\pi}$ tomogram passes the position suggested by tracing the upper cap of the half-moon around. This is amazing, because we do not find any shape or radiation front position within the channel at $\Phi = 0$, which could match the dynamics at $\Phi = \pi$. In the third image, the $XUV^{\Phi=\pi}$-tomogram depicts the radiation at the high-field side, where it remains until the thermal quench. Conclusively, the radiation front evolution is toroidally asymmetric and is not fixed to the field lines.

VI.3.5 Toroidal radiation asymmetry

Toroidal radiation asymmetry is evaluated and characterised by the TA value. Regarding neon: The four plots in the centre of Figure VI.11, can be compared in terms of a TA relation to E_{th} during the pre-cooling phase. It is nicely shown that the high-E_{th} plasmas exhibit a smaller mean value of the toroidal asymmetry during the pre-cooling $\langle \mathrm{TA} \rangle$, which implies that the impurities distribute more efficient in toroidal direction when the plasma is hotter. An indication number for the radiated energy is given: During Δt, the radiant power flux is accumulated, which yields $E_{\mathrm{xuv}}^{\Phi=0}$ and $E_{\mathrm{xuv}}^{\Phi=\pi}$ at the end of the considered time window Δt. The ratio of the energies is given in the middle of each window in Figure VI.11. For the neon shut downs, which differ in the pre-cooling phase related to E_{th}, compensate the radiated energy toroidally, which means that at the end of the scenario, the radiated energy at $\Phi = 0$ is equal to the radiated energy at $\Phi = \pi$. The energy ratios settle around 1. In helium, the initial asymmetry gets, so to speak, overcompensated during the current quench (energy ratios > 1). Argon behaves oppositely to helium: The plasma at $\Phi = \pi$ does not compensate the asymmetry from the pre-cooling nor in the thermal neither the current quench (energy ratios < 1). This is because argon tends to radiate toroidally symmetric during the thermal quench, because it forms a toroidally symmetric belt on the high field side. Argon triggers the thermal quench at the latest compared to helium and neon, which might be the reason for the more uniform redistribution around the torus.

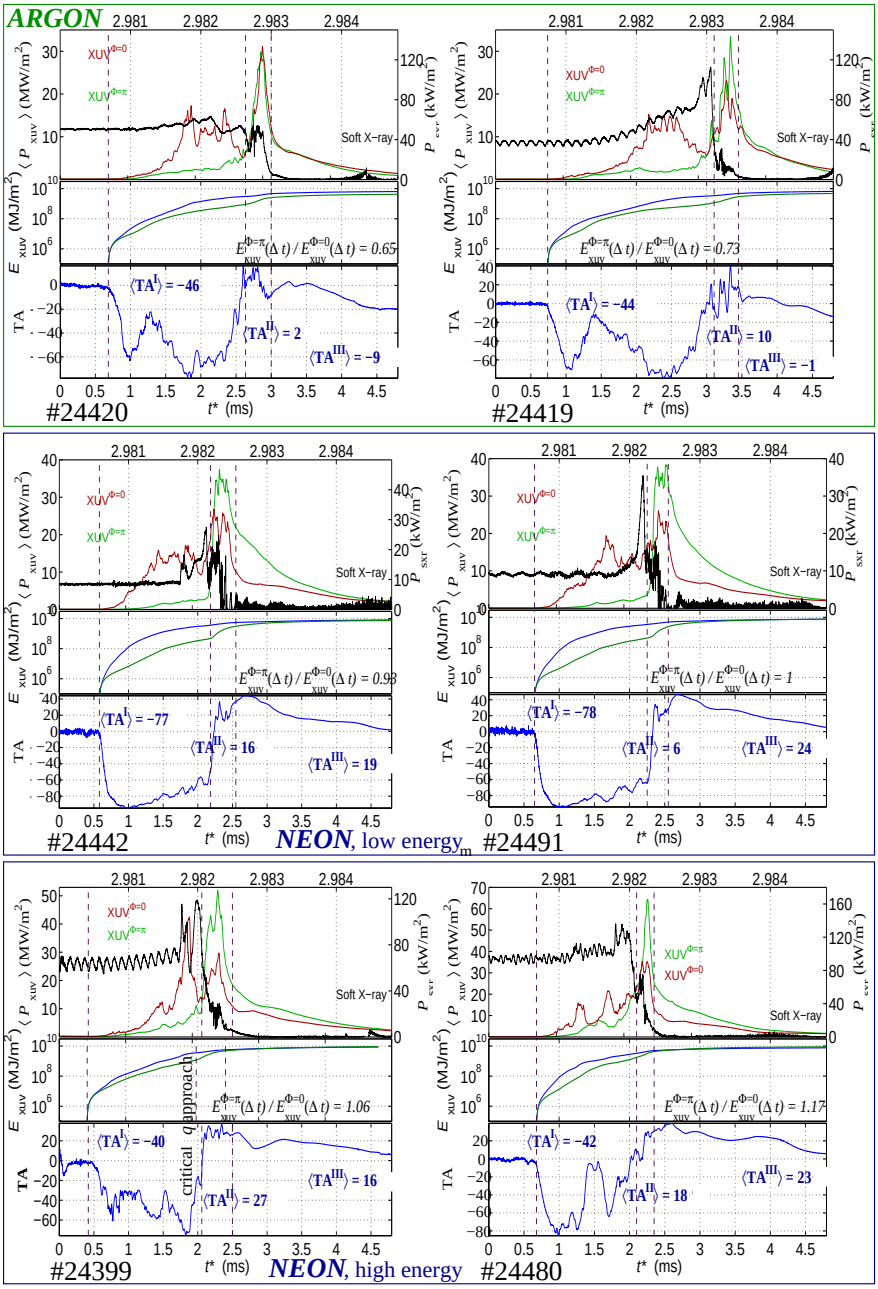

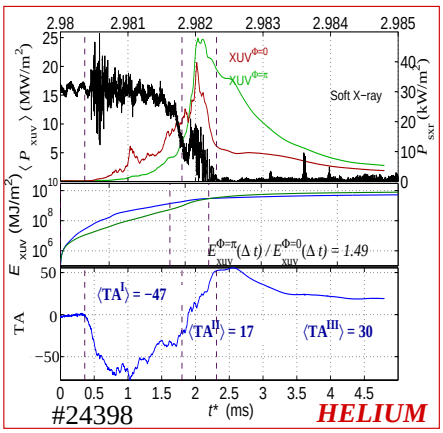

Figure VI.11: Toroidal radiation asymmetry in MGI shut downs. Each shut down is shown with three diagrams: The upper: Average value of the XUV radiant flux density signals in green ($\Phi = \pi$) and red ($\Phi = 0$), central single soft X-ray signal (black). Box below: Time integrated power signals shown above in the corresponding colours. Bottom: The TA number versus time. The time axis on the bottome applies for each graph. The phases are marked by the cursors: Precooling is in between the first two cursors, etc. The average values of TA are given for the respective phase durations with the according superscript.

VI.4 Poloidal impurity propagation

In the previous section, the radial and toroidal propagation of the radiation front during the pre-cooling phase was analysed. We stay in the pre-cooling phase and focus now on the poloidal impurity transport, which takes place in form of filamentary radiation structures. These structures detach from the turbulent interaction zone in front of the valve and are observed by the $XUV^{\Phi=0}$ camera. Imagine the filament as a tube-like[9] radiation source, whose axis is parallel to the magnetic axis. It moves poloidally away from the interaction zone and performs a poloidal rotation inside the separatrix. The $XUV^{\Phi=0}$ lines of sight observe the movement as an amplitude, which is phase shifted from channel to channel. Therefore, inclined stripes arise in the radiation pattern of this camera. Figure VI.2 showed an $XUV^{\Phi=0}$ pattern, where two filaments are marked by arrows. Figure VI.12 schematically illustrates the movement of a filament.

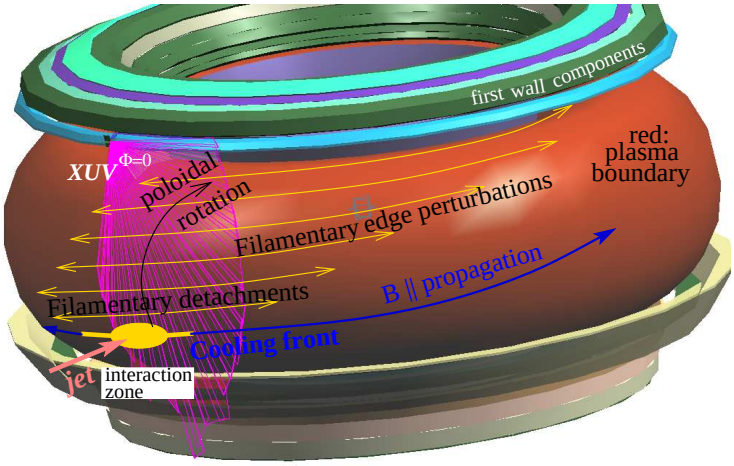

Figure VI.12: Scheme of filamentary edge perturbations. The interaction front is imaged as a yellow spot. Impurities propagate toroidally (blue arrow). Filamentary structures detach from the interaction zone, rotate poloidally and might expand toroidally to a certain extent (yellow double arrows). Note that they reside in the edge - they do not penetrate into the centre.

We gained the knowledge from Figure VI.2 that the occurrence of filaments is attributable to the reduced valve-plasma distance, the increased amount of injected particles and the higher jet pressure in MGI shut downs compared to the moderate puffing case. Accordingly, higher density and temperature gradients in the radiation front interior introduce the effect.

As shown by the TA traces in Figure VI.11 and in other illustrations such as Figure VI.2, the pre-cooling phase is characterised by a high toroidal radiation asymmetry. We

[9]Radially and poloidally constricted but toroidally expanded structure

noticed that the radiation front is not simply projectable via magnetic field tracing helically around the torus. This actually applies also for the filaments discussed here. We start therefore with the focus only on $\Phi = 0$, where they appear, and will turn toroidally around not before the fourth subsection, in which the $XUV^{\Phi=\pi}$ diagnostic is included. The section contains the following basic features:

- Filament trajectory
- velocity and,
- appearance toroidally around.

VI.4.1 Speed of poloidal filament rotation

Due to only one fan of lines of sight at $\Phi = 0$, the filament trajectory has to be discussed for an accurate evaluation of the filament speed: Basically, the filament could move radially, poloidally, it could rotate downwards or upwards. Figure VI.2 clearly shows that the stripes cover the full extension of the plasma. Due to this fact, a downwards directed movement on the low field side into the divertor is reasonably excluded. A movement across the flux surfaces into the main plasma region is surely not the case, because the soft X-ray diagnostic would capture such a pronounced impurity penetration during the pre-cooling phase. Therefore, the structure must rotate poloidally within the edge plasma. The direction of rotation is found to be upwards on the low-field side, because under this assumption, the filament exhibits a rather constant angular speed of rotation. The speed of rotation is evaluated in the following.

Regarding those two stripes marked in Figure VI.2: Before and after, striations appear either with a shorter length, of less pronounced contrast or of different inclination. The varying stripe lengths implies that the filament is lost by any reason: Conceivable is either a disintegration during the poloidal movement or an out-glowing due to a massive heat flux into the filament. Another aspect regards the superposition of toroidal and poloidal filament movement: Keep in mind that the poloidal $XUV^{\Phi=0}$ view geometry alone can not separate between poloidal and toroidal rotation, if the structure is helically adjusted and toroidally moving through the visual range of the diagnostic. In fact, the filament movement is an addition of poloidal and toroidal rotation if the toroidal plasma rotation is not locked. The poloidal revolution of the filament would only be traced fully if the ratio between poloidal and toroidal rotational speeds is sufficiently large. Therefore, the filament length L must sufficiently large for capturing a full turn (poloidal or toroidal) of the filament. Again, all together:

- The faster the poloidal rotation is at a given toroidal rotation speed and
- the larger the toroidal expansion, the more channels are passed by the filament.

Figure VI.13 illustrates the filament detection by $XUV^{\Phi=0}$ schematically.

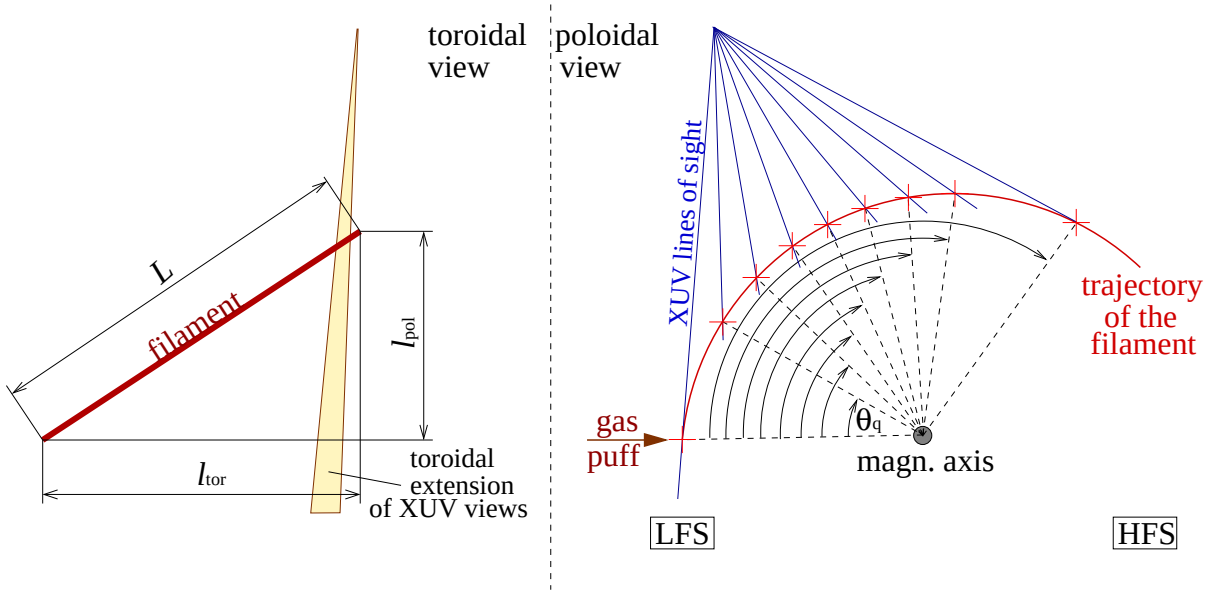

Figure VI.13: Schematic illustration of filament detection by $XUV^{\Phi=0}$. On the left, the toroidal - on the right, the poloidal views are shown. Abbreviations *LFS* for low field side, *HFS* for high field side.

In the following, the poloidal filament speed is evaluated. Referring to Figure VI.14: The discharge under consideration is the neon shut down #24399 (presented also in Figure VI.2). All signals of $XUV^{\Phi=0}$ for an initial sequence of the injection are shown on the upper left. The gray coloured signals correspond to the gray coloured lines of sight in the geometry drawing in the centre of the figure. They show strong fluctuations in the jet-plasma interaction zone. The coloured lines (red → orange) detect the filament. On the top, several lines of sight are gray coloured again. These channels do not detect the filaments. We deduce from this fact that the filaments rotate further inside the plasma.

The assumptions are itemised as:

- The full filament length L is observed (it does not glow out before it vanishes).
- The filament follows the magnetic field line
- The magnetic equilibrium reconstruction is close to reality

The reason why the upper gray coloured views do not detect the filament could also lie in the effect explained in the beginning of this subitem: The filament could just be lost after a certain time due to the toroidal movement - combined with a too small L for being still detectable. If that is the case, the assumption of $q = 2.5$ being the magnetic flux surface on which the filament resides, would be wrong. At this point it is emphasised that with two toroidal comparative measurements, an estimation of L is just impossible. Nevertheless, the assumption for q is reasonable, because each of the filaments in this shut

down either disperse before reaching the gray coloured lines of sight or do not cross them owing to being located closer to the plasma core.
In the plotting on the upper left of Figure VI.14, a blue cursor marks the onset of filament generation delayed by 1.1 ms with respect to t_{tr}. This position is used as origin for the x-axis in the plotting window below. There, only those signals, which are relevant for the filament characterisation are traced. The colour coding corresponds to the colours used in the geometry drawing. The chosen time window spans two plus the onset of a third filament revolution. This can be drawn from the number of maxima of a single signal and the synchronisation of the phase shift to the neighbouring signal. For this consideration, the second relative maximum is used. The vertical black lines on the bottom mark the starting time of the rising edges. The two lines shortly before 0.2 ms, lie extraordinary close to each other, because the corresponding view geometries overlap almost completely (see cyan coloured views 16 and 17 in the geometry drawing). The times of the vertical lines serve as axis for the plotting on the right hand side. The ordinate is the angle θ_{q} explained in Figure VI.13.

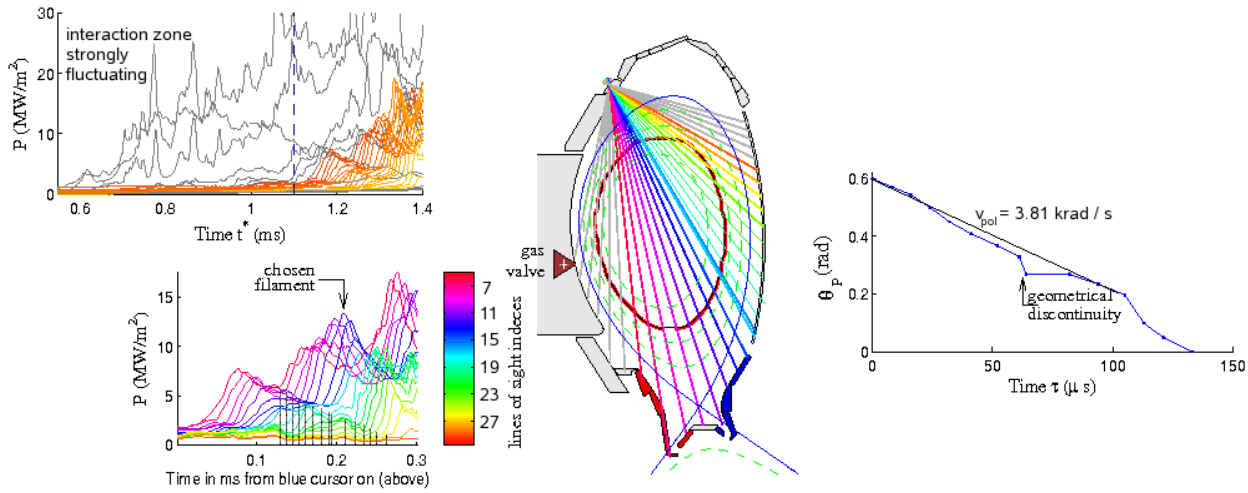

Figure VI.14: Speed of a neon filament rotation in shut down #24399. Vessel drawing: The gray lines of sight in front of the valve show strongly fluctuating signals. The differently coloured lines of sight show nicely the phase shifted amplitudes when the filaments run through the fan (the line colours correspond to the signal colours in the plot on the lower left). The gray lines on the top do not detect the filament. Plot on the right: The slope of the graph (angular filament position θ_{p} versus time τ) gives $v_{\mathrm{pol}} = 3.81\,\mathrm{krad/s}$. For evaluation purposes, the filament is assumed to rotate along the $q = 2.5$ surface.

The above investigated filament would move almost constant on the $q = 2.5$ surface, if the assumption of an upwards[10] directed filament trajectory is correct. With this perception, again, the line of sight geometry is considered for evaluating the poloidal

[10]Upwards on the low-field side.

speed of one of the subsequent filaments in the same shut down scenario. It is located a bit farther inside the plasma. See Figure VI.15: Line of sight no. 4 observes the radiation front. The channel is labelled by 'edge channel' and marks the edge of the hot plasma (between valve and radiation front, the plasma is already cooled with the consequence that still incoming impurities delivered by the valve, are not ionised anymore). The filament mandatorily lies on or inside the tangented area of the edge view. Channels 8 and 14 are selected, because they nicely observe the passage of the filament through their visual range. Channels of higher indices than 14 intersect the filament trajectory with more and more shallower angles, which results in a longer duration the filament requires for passing through the visual range of the single views. This is clearly featured by the bending of the filament track versus time in the contour plotting on the outer left.

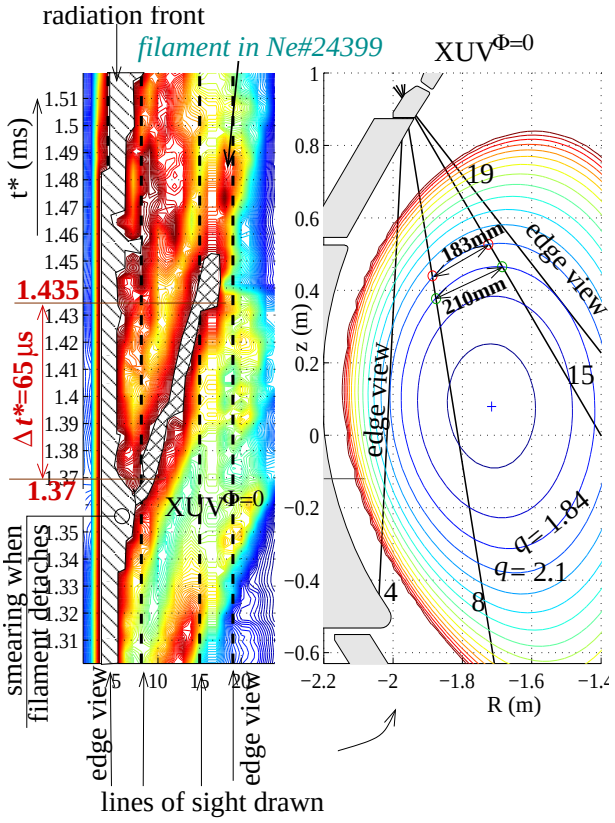

Figure VI.15: Filament speed in m/s in #24399. The single hatching marks the radiation front - the cross hatching marks the filament.

$v_{\mathrm{pol}} = \frac{210}{6.5\times10^{-2}} \frac{\mathrm{mm}}{\mathrm{ms}} = 3.2 \frac{\mathrm{km}}{\mathrm{s}}$

The upper 'edge channel' is the last line of sight, which detects the filament. After t^*=1.49 ms, the filament either glows out or it moves toroidally (or helically) out of the toroidally restricted visual range. Consider again the edge views: A significant smearing of the cooling front precedes the filament detachment. The filament then detaches and performs - as explained above - a poloidal rotation until it illuminates the other 'delimiting' edge channel. The smearing in the beginning of the filament formation is either due to a sudden sheering away from the nominal cooling front position or due to a cooling front expansion along the flux surface. Conceivably, it could be smeared in form of a half-moon (explained e. g. in Figure VI.13).

VI.4.2 Radiation patterns for different gas species and reservoir pressures

In this paragraph, we focus on the comparison of radiation patterns given by the top view cameras $XUV^{\Phi=0}$ and $XUV^{\Phi=\pi}$. The focus lies on the asymmetry of fine structures. In those patterns presented in Figure VI.16, we observe filaments, striations and magnetic mode rotation, which all constitute poloidal cooling structures. As published in [26], the discharges presented in this thesis exhibit the trend to lower fuelling efficiencies with an increasing E_{th}. The focus in this paragraph is put onto this issue by comparing of what we define as discharges of *low* and *high* E_{th}.

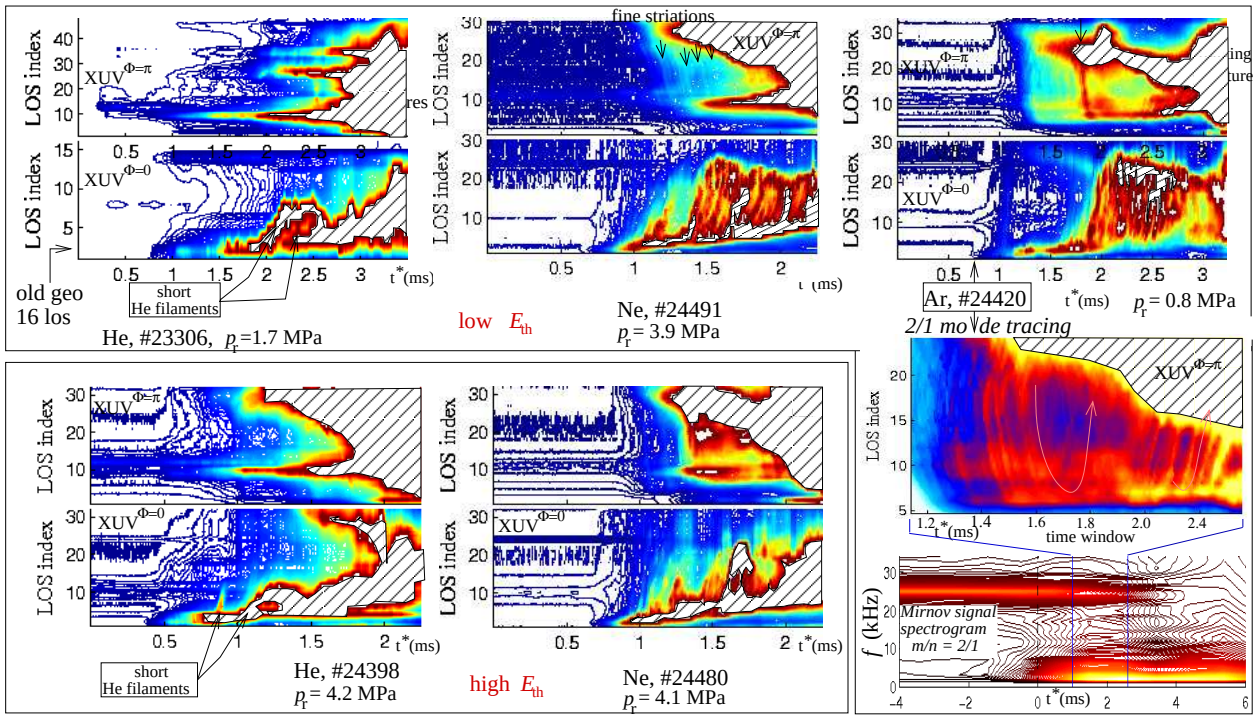

Figure VI.16: Fine structured radiation patterns in different gas injection scenarios. The area of large emissivity is hatched. On the lower right, a spectrogram of a signal of a Mirnov coil on the midplane, low-field side is shown.

In Figure VI.16, the $XUV^{\Phi=0}$ and $XUV^{\Phi=\pi}$ top view camera measurements are imaged as contours versus time. In total, five shut downs are shown - three of low E_{th} and two of high E_{th}. In the upper row, the discharges He #23306, Ne #24491 and Ar #24420 are conform with the requirement of a comparably low E_{th} (418 kJ, 383 kJ, 410 kJ). On the bottom, shut downs of higher energies are shown: Helium, 545 kJ and neon 746 kJ.

Comparison high-low E_{th} in helium:

Starting with the helium injection presented on the upper left. At $\Phi = 0$, the well-known 'track' features the radiation front. The radiation front moves inwards until a short, but

very pronounced filament appears ($t^* \approx 2\,\mathrm{ms}$). This short filament removes the impurities from the interaction zone. After roughly $200\,\mu\mathrm{s}$ from then on, the radiation front is formed anew due to still delivered impurities. This mechanism is a basic feature of filaments, which applies also to the other sorts of gas: It removes impurities from the radiation front. This phenomenology is also observed in the high p_r, high E_th helium case, shown below. Again, short filaments occur. The radiation front again is reduced in its luminosity. Considering the $XUV^{\Phi=\pi}$ measurements: Horizontal structures are imaged, but no rotational movement. Conclusively, a special helium feature is that at $\Phi = 0$, the 'short filaments' are the only pronounced filamentary structures observable.

Comparison high-low E_th in neon:

The neon shut down placed on the bottom of Figure VI.16 has an almost two times higher E_th content than the upper one. Both were performed with comparable p_r. The low E_th shut down exhibits a very frequent filamentation activity. Toroidally oppositely appearing fine striations are detected - albeit we note that the appearance of such structures at $\Phi = \pi$ is not a common feature in neon. Striations at $\Phi = \pi$ are observable in #23304, #24395, #24396, #24491,
not observed at $\Phi = \pi$ in #24399, #24442, #24480.
With respect to Table VI.1, in which the E_th values of the respective shut downs are listed, we conclude that striations in neon at $\Phi = \pi$ are not related to E_th and not related to the activity of filamentary edge perturbations in front of the nozzle.
Referring again to Figure VI.16: The high E_th case #24480 shows, as mentioned, no rotating structures at $\Phi = \pi$. Also at $\Phi = 0$, filamentation is of weaker dynamics compared to the low-E_th case above. But note that a striation pattern at $\Phi = \pi$ was found in the second high energy shut down #24396. A discussion on an E_th dependence of striation patterns is therefore hardly substantiated, whereas filamentation might be reduced with enhanced E_th (see also Figure VI.17, where $XUV^{\Phi=0}$ data of, again, one high E_th and one low E_th discharge is compared. Also there, the high E_th case exhibits less filamentation dynamics).

Comparison high-low E_th in argon:

The beginning of the scenario is comparable to the others. In the course of injection however, the radiation front is completely displaced and resides from 2 ms on in the upper plasma region. The filamentation is extremely active and multifaceted. At $\Phi = \pi$, the signals show a structure, which performs full poloidal turns. The contour is separately shown on the lower right to emphasise the activity at $\Phi = \pi$. The structures are enclosed in themselves and are present for almost 1.5 ms. The mechanism is the same as depicted in the edge cooling disruption in Chapter V. In the corresponding contours in Figure V.9, the core mode correlated edge radiation is shown. There, a large amount of nitrogen was residing in the edge - here, the argon impurities in the edge trace the

rotation of the central 2/1 mode, which was present already before the gas valve trigger. Note that this mode tracing mechanism is not related to impurity redistribution rather than to an excitation of impurities due to an enhanced radial energy flux correlated to the mode frequency. And note, the mode tracing mechanism is not an effect related to a specific sort of impurity rather than to the rotation speed of the central mode: The slower the mode rotates, the more pronounced is the effect and the brighter it appears to radiation detectors. (Some remarks regarding the observed magnetic mode: As we know from the edge cooling disruption in Figure V.9, one stripe, which passes through the fan of $XUV^{\Phi=\pi}$ in one direction corresponds to half a poloidal turn of the central mode. In Figure VI.16, two neighbouring points, where the trace changes its direction from downwards to upwards, are temporally spaced with $\approx 0.24\,\mathrm{ms}$. This corresponds to a mode frequency of $f_{2/1} = \frac{1}{2*0.24\mathrm{ms}} \approx 2\,\mathrm{kHz}$. Such small frequencies are also depicted by the magnetic spectrogram shown on the lower right in Figure VI.16.)

VI.4.3 Intensive radiation burst in the pre-cooling phase

In several shut down scenarios[11], the following effect took place: As the radiation front penetrated deep into the plasma, a very intense radiation flux takes place. This strong response on the impurity front happens at a certain penetration depth and is followed by a redistribution of impurities, meaning a poloidal transport to the high field side. The burst occurs at a penetration depth comparable amongst the different scenarios. It is viewed from above with the $XUV^{\Phi=0}$ fan of lines of sight and appears always in the same channel. (Recall that tomography is not possible at this location ($\Phi = 0$).) At $\Phi = \pi$, the burst does not occur. The burst is an additional effect, which is toroidally asymmetric. It is an important phenomenon due to two reasons: As a first aspect, the high emissivity potentially poses a risk in terms of radiative load on nozzle protectors or wall components, because e. g. in #24399, the radiation flux densities are even higher than in the thermal quench. In a second respect, the radiation front penetration into the centre is interrupted. Instead of penetrating further in radial direction, the impurities face a kind of a barrier and are redistributed or transported poloidally via a filament to the high field side. Figure VI.17 shows the behaviour of two neon scenarios (#24399 and #24442).

Both neon shutdowns show a distinct radiation front and filament activity during the pre-cooling phase. The high emission of the above described burst is marked by a green hatching. Comparing the times of the burst amongst the two cases, we find a comparable time, $t^* \approx 1.8\,\mathrm{ms}$. The position is depicted by the same channel in both cases (channel 6). A subsequent deformation of the plasma boundary on the low-field side (LFS, marked in Figure VI.17 as 'shrinkage') is clearly featured also in both cases. In the short sequence

[11]The significant plasma response is observed in neon exclusively. It is observed in three of five neon shut downs: Present in #24399, #24442 as well as #24480 - it is absent in #24491 and #23304.

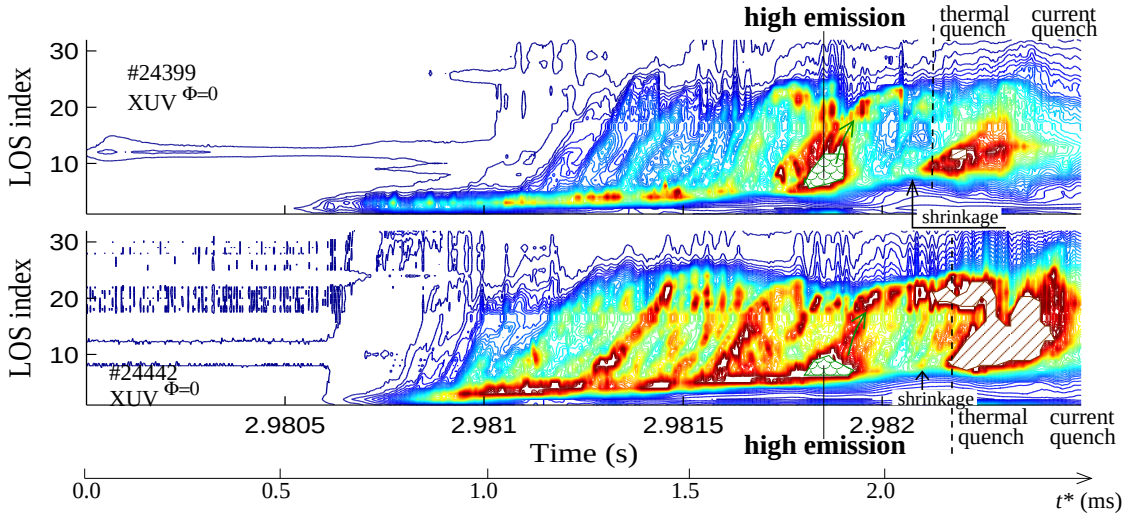

Figure VI.17: Penetration depth dependent intensive radiation burst and interruption of radiation front penetration. Above: $XUV^{\Phi=0}$, #24399, $p_r = 1.1\,\mathrm{MPa}$; below: $XUV^{\Phi=0}$, #24442, $p_r = 4.4\,\mathrm{MPa}$. Bright emissions are cut and hatched. The time axis applies for both contours.

between the last filament and the thermal quench onset, (maximal 200 μs duration), the radiation front in the vicinity of the valve is not reestablished. During this sequence, also the filament activity is low and impurities are either located mainly at the high-field side (#24442) or they are smoothly distributed across the poloidal cut observed by $XUV^{\Phi=0}$ (#24399).

The burst first occurs in channel 6 and shifts within a few tens of microseconds to channel 7 before it decays in both channels. Then, the filament arises. We will now include the opposed toroidal location $XUV^{\Phi=\pi}$ for investigating the toroidal plasma response on the penetrating impurities. For these considerations, we additionally will include the magnetic topology for finding the q position, where the burst happens. The magnetic data is also used for tracing the burst position toroidally around for finding a correlation between radiation at $\Phi = 0$ and $\Phi = \pi$.

Figure VI.18: The series of images covers a duration of 110 μs. It concerns the shut down #24399. Channel 7 is inserted and we assume the radiation front residing on the horizontal projection of the gas nozzle axis. The green dot marks the corresponding position. The $XUV^{\Phi=\pi}$ tomogram is inserted (recall, it is toroidally π shifted). The tomogram shows the radiation maximum at a higher q at this time. Switching back to $\Phi = 0$, where the filament is born at this point in time. We know from the previous sections that it performs a poloidal rotation along the respective magnetic flux surface. Henceforth, we fix the q at 1.7 (green) from now on. In the second snapshot, the radiation front is observed by channel 8. We put the green dot onto the intersection point of the channel with the respective q surface. Then, we trace the corresponding field line toroidally π around to the $XUV^{\Phi=\pi}$ position and arrive at the green circle. Again, the

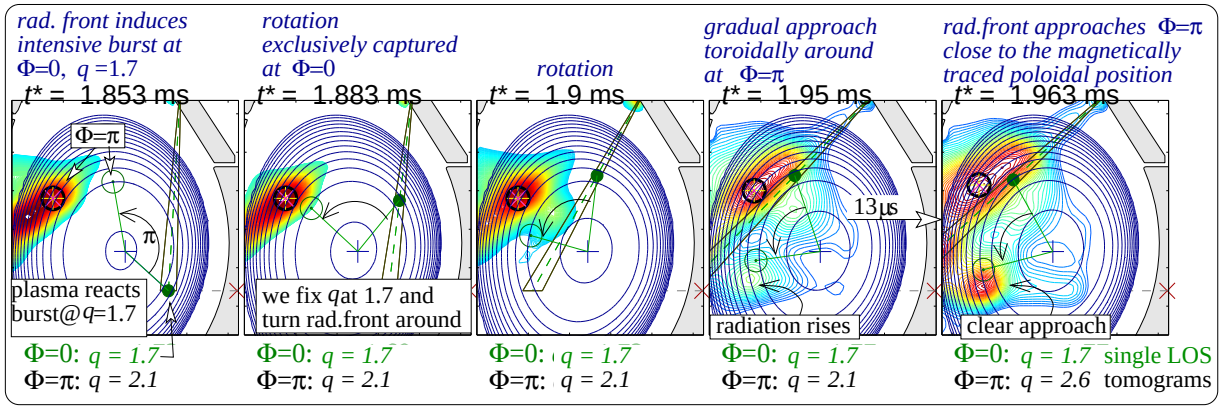

Figure VI.18: Plasma response on impurities at a critical position. Shut down #24399. The green channel observes the radiation maximum at $\Phi = 0$. Field line tracing:
Green dot at $\Phi = 0$ $\rightarrow$ is traced to $\rightarrow$ green circle at $\Phi = \pi$.

q values of radiation and the traced cooling front do not correspond to each other. The condition after furthermore 17 μs is shown in the third snapshot. And again, the radiation at $\Phi = \pi$ does not react. Contrarily, from the fourth snapshot on, the plasma at $\Phi = \pi$ responds to the burst: An additional structure is appearing close to the traced circle. It becomes gradually stronger from snapshot 4 to 5, which are temporally spaced of only 13 μs.

Conclusively, the intensive burst is communicated toroidally around with a time delay of about 150 μs. It is in comparable order with respect to the delay times evaluated in the earlier discussions on the initial response ($\tau_{\mathrm{tor}} = \tau^{\pi}_{\mathrm{lat}} - \tau^{0}_{\mathrm{lat}}$, Figure VI.4). We deduce that the cooled plasma region, in which the radiation front resides, does not change significantly its temperature during the pre-cooling. With respect to the position of the burst, we note that the q coordinate is in the vicinity of the resonant flux surface $q = 2$, which is well known from many other works as being a critical q for the appearance and growth of a magnetic instability. However, in this stage of the disruption, the magnetic equilibrium reconstruction is not trustable anymore, because the radiation front has penetrated several centimetres and cooled the outer region of the plasma. A redistribution of the current profile due to the high resistivity in the outer region is surely the case. The magnetic flux topology might therefore be affected by an uncertain error bar. Anyway, a generation of a resonant mode is not observable in magnetic measurements. A more reasonable explanation for the high emission is the approach at a new energy reservoir. Before the front approaches at the critical position, the edge temperature is steadily reduced, which is reflected in the constant penetration velocity of the radiation front. However, when the front arrives at the hot core plasma, a sudden energy burst could cause a disintegration of the spatially constricted cooling front as it is observed when a MARFE is flushed out by a sudden high energy conduction. At a low-q, the energy supply is fast and of small

duration, because the magnetic field lines penetrate the cooling front.

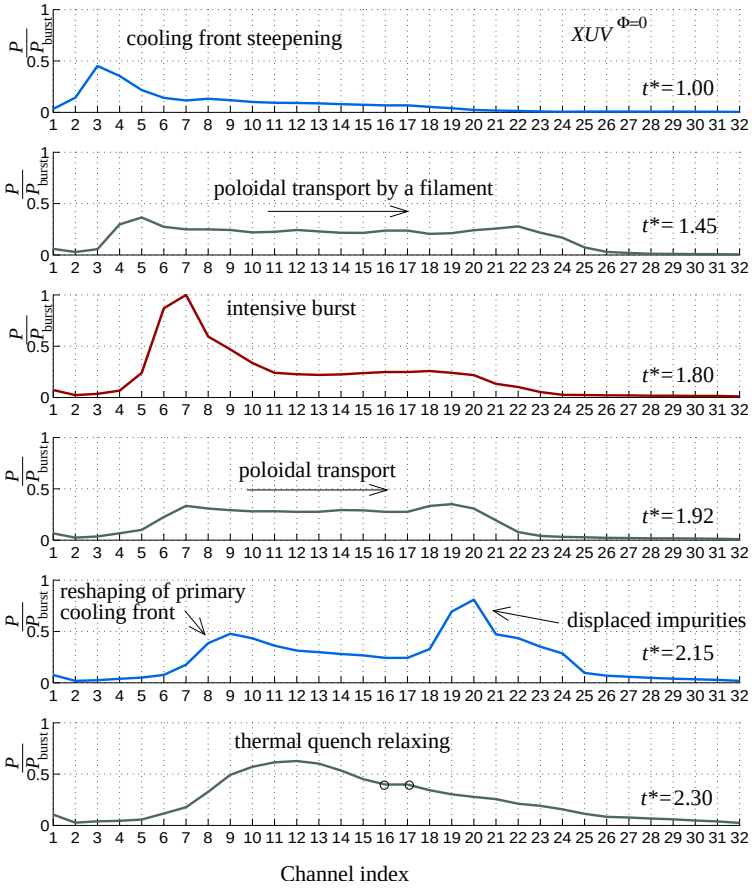

Figure VI.19: Intensive burst and redistribution. The XUV$^{\Phi=0}$ measurement signals are normalised on the intensity of the burst. The ordinate are the channel indices, note channel 16 and 17 overlap. Time t^* is equivalent to $t - t_{\mathrm{tr}}$.

Figure VI.19 reviews the whole scenario from profile steepening at low channel indices over relaxing processes by poloidal transport via filaments, further with the intensive burst and the subsequent poloidal transport through to the final balancing of the profiles in the thermal quench.

VI.5 Thermal and current quenches

As explained in Chapter III, the thermal quench is defined at the onset of soft X-ray fluctuations, which is typical for the thermal quench in disruptions[12]. Consider again the two figures on radiation front penetration VI.7 and VI.8. On the contrary to soft X-ray bulk emission, the thermal energy, E_{th}, decays already in the pre-cooling phase. Note the denotation 'thermal quench' regards exclusively the loss of central thermal energy, which is indirectly featured by the loss of soft X-ray bulk emissivity. The behaviour is clearly seen in the referred figures: Soft X-ray emission falls down to about a half of the initial emission. The decay is retarded and the signal starts to fluctuate. The onset of the current quench is defined by the current hump, which implies the current profile redistribution. It is not always visible and if not, the current just starts to decay during the soft X-ray fluctuations. The current hump is delayed only a few tens of microseconds with respect to the thermal quench. Both quench phases overlap in time.

In MGI experiments, we aim at fuelling the plasma within 2 milliseconds with electrons, bound and free. It is appreciable to reach a high density before the current quench onset to avoid the Dreicer effect. For the suppression of avalanching, it is necessary reach the critical density in the current quench. Electron density measurements are published in [26]. Here, we focus on the two-dimensional radiation distribution, because it implies the distribution of partly stripped impurities, which either constitute a source of free electrons or the carriers of bound electrons.

As we know from above, a penetration into the core during the pre-cooling phase is not the case. In neon, we clearly found a kind of a barrier at a position nearby the core plasma[13]. The significant difference between the plasma in the pre-cooling and thermal quench phase is the MHD activity (soft X-ray fluctuations), which might lead to a significant rearrangement of the magnetic topology in the thermal quench.

VI.5.1 Radiation distribution

The characteristics of the different gases during the thermal quench is the subject of this paragraph. It will be shown that the radiation front in the helium shut down #24398 settles in the core during the thermal quench, neon #24399 stays outside the core and covers the area on the high field side between edge and core. Argon behaves comparably to neon - albeit at a very last stage in thermal quench.

The thermal quench in the helium shut down #24398 shall be considered at first. The series of tomograms shown in Figure VI.20 is regarded. It ties up to the pre-cooling series presented previously in Figure VI.7. The thermal quench starts at $t = 2.9818\,\mathrm{s}$ and lasts

[12] We noted already in Chapter III: These fluctuations could be attributed to stochastisation or reconnection processes of magnetic field lines.

[13] Core plasma: $q < 2$

514 μs ($\Delta E_{\mathrm{th}} \approx 200$ kJ). The innermost dashed poloidal line inserted in the tomograms represents $q = 2$, which is known to be a critical flux surface in terms of the onset and growth of magnetic instabilities. The first and last frame belongs to the pre-cooling and current quench, respectively. At the beginning of the series, the cooling front in fact resides at $q = 2$ but does not induce the fast fluctuations in the soft X-rays. In β, the soft X-ray emissivity in the centre starts to fluctuate, from which we depict the thermal quench onset. In snapshot η, the maximal emissivity is detected. A tail of the emissivity significantly enters the area inside $q = 2$. Regarding the soft X-rays at ε, the signal falls at this time and shows the fluctuations typical for the thermal quench. From Θ on however, the luminous area expands. Tomography κ represents the distribution in the current quench. In this sequence, impurities are clearly present in the core. Note that the emissivity corresponding to this core radiation is only of about 60 % of the one in the thermal quench (frame ε).

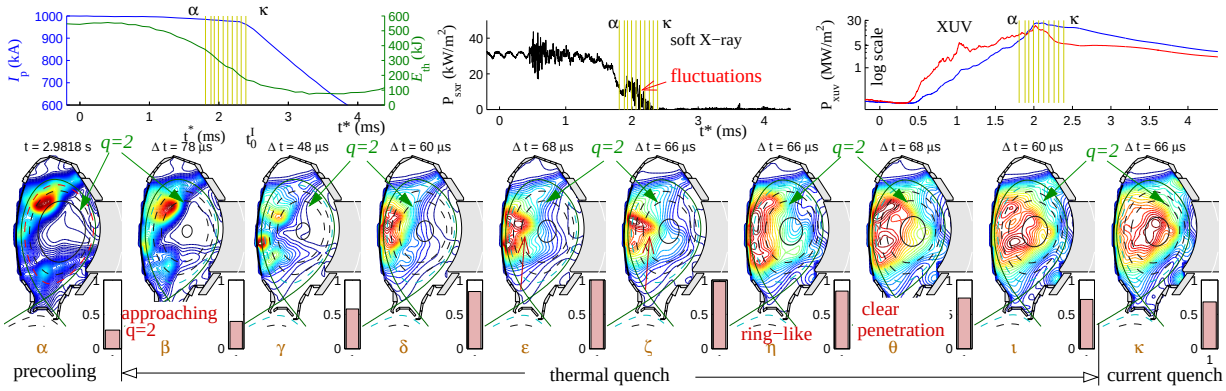

Figure VI.20: Radiation evolution during the helium shut down in the thermal quench (#24398). On the upper left, E_{th} in green and I_{p} in blue are drawn. In the middle, central soft X-ray. On the right, $XUV^{\Phi=0}$ in red and $XUV^{\Phi=\pi}$ in blue (logarithmic scale). The time points of the tomography series correspond to the yellow markers. The Δt label of the tomograms gives the time slice in between the tomograms. Bars on the bottom represent the emitted power at the corresponding time point normalised on the maximum within the series (here, frame ε).

In comparison to the thermal quench in Helium, Figure VI.21 presents the shut down in neon, whose pre-cooling is shown in Figure VI.8. The $q = 2$ surface from α to ι is drawn by the innermost dashed line, in κ it is represented by the innermost solid line. Regarding the signal traces of E_{th} and soft X-rays, the thermal quench sequence is more distinct observable than in the He shut down (soft X-ray fluctuations and increased $\mathrm{d}E_{\mathrm{th}}/\mathrm{d}t$ from snapshot β to δ). The duration shown here is 380 μs long, while again, the first tomography belongs to the pre-cooling and the last one to the current quench. The centre of radiation resided from α to γ basically between $q = 3$ and $q = 2$ above the midplane, while the falling edge of the cooling front significantly passes over $q = 2$, as described in Figure VI.8.

From δ on, a fragmentation leads to a distribution of impurities also to regions below the midplane. And from ε on, which is the frame of highest XUV emissivity, a more dispersed presence of impurities across the main plasma region is reconstructed. Nevertheless, neon behaves differently compared to helium in terms of impurity penetration: The bulk of the impurities remains outside the core, also in the current quench.

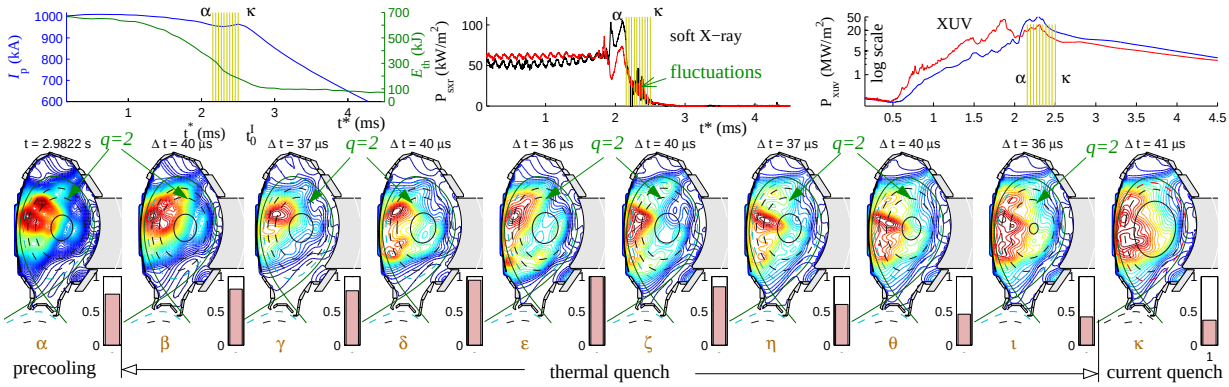

Figure VI.21: Radiation evolution during neon shut down in the thermal quench (#24399). On the upper left, E_{th} in green and I_{p} in blue are drawn. In the middle, central soft X-rays from toroidally separated cameras. On the right, $XUV^{\Phi=0}$ in red and $XUV^{\Phi=\pi}$ in blue. The time points of the tomography series correspond to the yellow markers. Bars on the bottom represent the emitted power at the corresponding time point normalised on the maximum within the series (here, frame ε).

As a next, the argon shut down #24420 is shown. In this special case, we expand the time window of our considerations into the pre-cooling for showing the history from mode rotation over a radiation contraction through to a MARFE-like high-field side impurity amassment. See Figure VI.22: Tomographies from α to δ represent the late stage of the pre-cooling: Snapshot α shows the main fraction of radiating impurities residing on the high-field side with the maximum below the midplane, which is completely different from the other cases. We significantly observe an open ring of radiation covering the low-field side. It disappears in the subsequent frames. Actually, the ring is rather a dotted line than a closed ring but note the tomography in this regard is dependent on the user defined smoothing function. So, an enhanced smoothing would rejoin the dots. This observation gives rise to be connected with the mode-like rotation revealed by the radiation patterns in Section VI.4. At ε, the structure significantly moves towards the core. Some microseconds after this short approach, soft X-ray start to fluctuate - the thermal quench is triggered. In the tomographies later than ε, a fragmentation is reconstructed likewise to He and Ne. The radiating structures do not penetrate to the core - also not in the current quench.

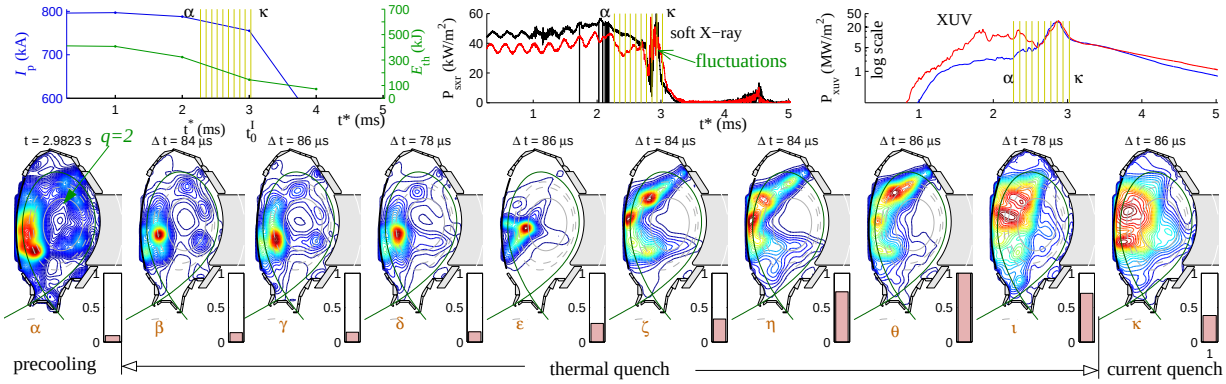

Figure VI.22: Radiation evolution during Ar shut down in the thermal quench (#24420). On the upper left, E_{th} in green and I_{p} in blue are drawn. In the middle, central soft X-rays from toroidally separated cameras. On the right, $XUV^{\Phi=0}$ in red and $XUV^{\Phi=\pi}$ in blue. The time points of the tomography series correspond to the yellow markers. Bars on the bottom represent the emitted power at the corresponding time point normalised on the maximum within the series (here, frame θ).

Radiation distribution during the current quench is basically of the character shown by the last image in the series in figures VI.20, VI.21 and VI.22.

VI.5.2 Power balance

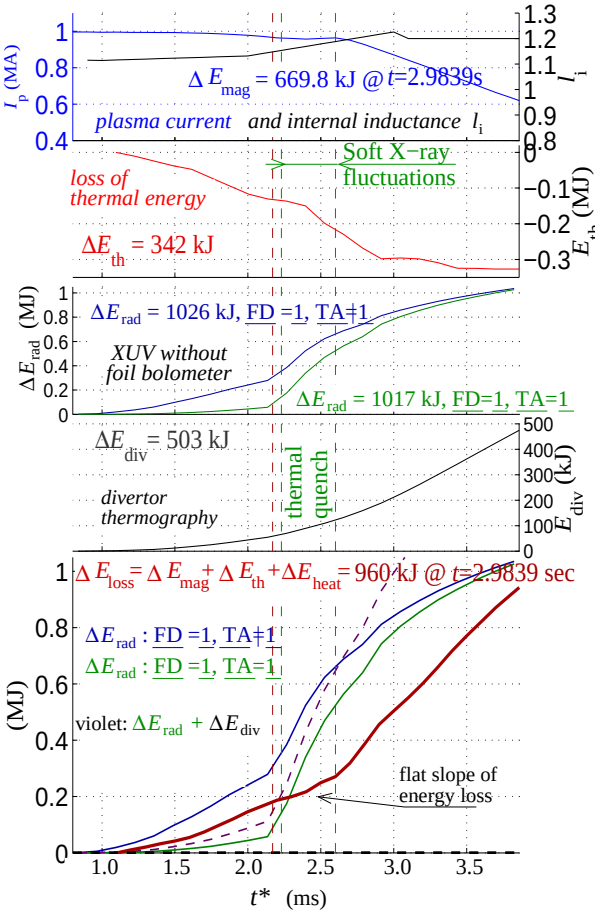

Figure VI.23: Energy balance in MGI, neon #24442. The inductance l_i is uncertain after $t = 2.983$ s and is thus forced to 1.2.

It was shown in Chapter V that the *XUV* radiation detectors are not applicable for measuring absolute power values for later stages in a disruption and it was explained that the impurity mixture has a significant influence on the comparison between diode and foil bolometry measurements. The diode measurement is thus affected by an uncertainty, which one only can tackle by applying a reference detector in the VUV spectral region. Nevertheless, Figure VI.23 shows an energy balance evaluated by taking the toroidal asymmetry into account without using the bolometer (due to the low time resolution). The plot window is restricted to the pre-cooling phase due to $f_{vuv} \rightarrow 6$ in later disruption phases. The pre-cooling phase is characterised by a very high toroidal radiation asymmetry, while the toroidal decay of emissivity between the stereo measurement positions is unknown. One can assume a linear decay between $\Phi = 0$ and $\Phi = \pi$.

This is shown in the third row of Figure VI.23 (the graphs and labels concern Equation V.5), where we switch the toroidal asymmetry matrix on and off by either applying the *local toroidal asymmetry* matrix TA (see Section V.2.2) or setting it to 1. The blue (with TA) and the green curve (TA=1) are the results. On the bottom, these curves are compared with the lost energy $\Delta E_{\text{loss}} = \Delta E_{\text{mag}} + \Delta E_{\text{th}} + \Delta E_{\text{in}}$, which includes all the present sources of energy. Presupposing a linear decay between $XUV^{\Phi=0}$ and $XUV^{\Phi=\pi}$, the radiated energy would exceed the lost energy from the plasma. This is clearly an overestimation. It can be compensated by using a shaped decay function such that the radiation is more shifted to $\Phi = 0$, while a decay function is surely strongly dependent on time due e. g. to successive filamentary detachments.

Chapter VII

Summary And Conclusions

In summary, the abrupt and massive injection of noble gases into keV tokamak plasmas generates localised radiative interaction dynamics, which have been reconstructed and characterised in this work with a hitherto unprecedented temporal and spatial resolution. The AXUV semi-conductor technology was employed in form of a 144-multichannel radiation tomography system and by following the principle of a stereo measurement with 32 additional lines of sight for tracking the poloidal and toroidal propagation of the radiation front from which the transport time scales of ions are deduced. The XUV photometer revealed the dynamics involved when the injected impurities induce strong radiative energy dissipation, which affects the plasma equilibrium and pushes it into disruptive conditions. New light was shed onto regimes, where standard tokamak diagnostics are usually inapplicable due to extraordinary circumstances such as excessive emissivities, strong magnetic perturbations, very high densities and finally due to the fast transient behaviour of all those parameters.

The method of massive gas injection for enhancing the electron density towards critical magnitudes, where runaway population is predicted to be suppressed, is put into practice by utilising one single, highly pressurised gas cell installed in the very close vicinity of the hot plasma periphery (13 cm distance). The reservoir is loaded by up to 8×10^{22} particles, corresponding to 4 MPa reservoir pressure. The valve opening time plus the gas flow duration ranges in the order of 2...3 ms. These experiments constitute the first ones following the strategy of injecting such a high amount of particles from a close distance. It is motivated by avoiding particle losses outside the plasma, which either directly load the pumps or are absorbed by the walls without contributing to the plasma fuelling. The spatially constricted jet-plasma interaction zone, however, led to a reduction of the fuelling efficiency as listed in Table VI.1 and published in [26], although the plasma density could indeed be increased. In fact, the fuelling efficiency is of crucial importance with respect to an application in ITER, because in case of a low fuelling efficiency, the required amount of injected particles would most likely exceed the capability limits of vacuum systems during

the injection. And, after the plasma termination, the remainder of injected matter could make long pumping sequences in between discharges necessary in order to avoid possible restart problems in subsequent discharges.

Review of the scenario

Toroidal transport: The new *XUV* photometer revealed the impurity transport times. We begin with the toroidal propagation time, starting with the very first impurity atoms arriving at the plasma edge in front of the valve. They are heated and ionised close to the plasma boundary and are guided helically around the torus with an average velocity of - for instance in case of neon[1] - 28 km/s, derived from the initial appearance of enhanced radiation at the opposite camera location as discussed[2] in Section VI.3.3.

During the pre-cooling duration of 1.5 ms (the time between valve trigger and disruption start) and with a field line of about 6 m length half around the torus, these early neon ions circulate around the whole torus only 3.5 times. In the meanwhile, the valve continues to deliver particles, reaching some transient maximum and decaying afterwards. This main part of the jet arrives later at the plasma, still continuously creating ions, which again travel along field lines with a comparable helical velocity around the torus (see Section VI.4.3). Henceforth, due to their delayed creation, they can travel only correspondingly shorter helical distances until the disruption occurs. In the edge of the helical field line structure of a tokamak, this means that the poloidal area covered by the ion trajectories is also smaller. In consequence, the bulk of the injected species do not have the chance to redistribute over the full torus on the short timescales before the disruption occurs. In conclusion, the time in between gas valve trigger and disruption is too short for a uniform impurity redistribution, which is mandatory for fuelling the plasma efficiently in order to suppress runaway population. Yet, reducing the gas valve pressure[3] below 0.5 MPa leads to a significant enhancement of the fuelling efficiency of 40 %. This is due to a combination of two effects: A more extended pre-cooling phase, which lasts 35 % longer than in high-pressure cases and a reduced reflection of neutral particles at the interaction zone between jet and plasma.

The sequence in between valve trigger and disruption was denoted by *pre-cooling phase* in this work. As mentioned, *the duration of the pre-cooling phase is a significant parameter for increasing the fuelling efficiency*, because we already operate at - or even beyond - the limit, where the helical transport time scale is in the order of the pre-cooling duration itself. Consequentially, a uniform redistribution in the whole plasma column is practically unattainable with the single-injector approach. A double-jet system with toroidally spaced injectors is therefore recommended.

[1] Discharge indication number #24491.

[2] The radiation arises due to ionic transport not due to an expansion of a neutrals cloud as explained in the referred section.

[3] See Table VI.1, discharge #23304, $p_r = 0.49$ MPa, $E_{th} = 430$ kJ, $F_{eff} = 0.32$.

Radial penetration and filaments: The jet-plasma interaction zone in front of the nozzle radiates at high emissivities of up to 10 times more than toroidally π around[4]. The impurity delivery from the nozzle lasts for about 2 ms - depending on reservoir pressure and gas species. In a first instance, the neutrals are ionised in the plasma boundary in a region, where the plasma electron temperature is sufficiently high (see radiation curves in Figure II.4). Ionised particles are steered along the helical magnetic field as explained above. Considering neon, for instance, the ratio between the measured radial and toroidal propagation speed is 1/112. The neon interaction front penetrates into the plasma interior with a speed of about 250 m/s. This means that, with a simple linear extrapolation, a massive neon-plasma interaction zone would have reached the plasma centre after about 2 ms (with the minor plasma radius $r = 0.5$ m), which is not observed. In this regard, an arising effect, which interferes the radial forward penetration, is the fragmentation of the interaction front, which leads to a separation of impurities from the interaction zone in form of condensed helical structures characterised in this thesis. They rotate poloidally away across magnetic field lines (in parallel to the toroidal expansion described above). They transport impurities poloidally towards the high field side of the torus without fuelling the core plasma. In this work, these structures are referred to as filaments[5]. As a consequence of filamentation, the localised interaction front carries a lower amount of impurities. One might deduce a negative effect with respect to the fuelling behaviour compared to scenarios, where the filamentation activity is low, because then, a massive impurity front would penetrate towards the core and fuel the plasma with a higher efficiency. However, in conclusions based on the results of this work, the occurrence of filamentation has two important positive effects:
Filamentation helps to reduce the large radiation fluxes from the local interaction zone on adjacent wall structures. If massive gas injection would be applied in ITER, one fears about wall melting due to an extreme thermal load onto nozzle protectors and surrounding wall components via electromagnetic radiation. Additionally, the massive poloidal transport by filaments towards the high-field side is favourable from the point of view that a disruptive plasma might radiate toroidally more uniform, if impurities were finally accumulated on the high-field side in a toroidally symmetrically fashion. In fact, disruptions with a toroidal belt-like argon accumulation on the high-field side were toroidally rather symmetric in the thermal and current quench phases[6]. Neon and helium, however, seem to behave somewhat differently: A helium or neon radiation front, which evolves like a helical belt around the torus, covers several flux surfaces simultaneously, while the

[4]Under consideration of transient radiation bursts.

[5]See measurement data in Figure VI.15 and schematic illustration in Figure VI.12.

[6]Argon toroidally symmetrically on the high-field side, see Figure VI.17. Radiation in the current quench, see Figure VI.11.

track does not correspond to the pathways of magnetic field lines[7]. This seems to imply a more complicated three-dimensional cooling pattern grown from the strongly radiating jet-plasma interaction zone on the low-field side. The high toroidal radiation asymmetry during the energy quench in neon and helium is reasonably connected with this effect. For this reason, it might be favourable for future experiments to inject the gas from the high-field side, which exudes substantiated optimism with respect to generate a toroidally more balanced radiation front and less radiation asymmetry during the energy quench phases.

The filament shape: The speed ratio between the filamentary motion in poloidal direction and the mean ionic expansion in helical direction is about 1/8 (corresponding to the filament presented in Figure VI.15), i. e. the poloidal filament velocity is significantly smaller than the (bidirectional) expansion velocity along field lines. Accordingly, a filament should look like a poloidally moving tube with capped ends ('cigar shaped' filament) with continuously increasing length, because it would expand helically with the helical expansion speed corresponding to the speed ratio. However, in between the stereo measurement positions of the new XUV diagnostic, only estimates about form and behaviour of the impurities can be made. Assuming that the radiating filament length during separation from the interaction zone is comparable to the interaction spot diameter, the filament might be visible toroidally π around at poloidally comparable positions, because a poloidal rotational movement of e. g. 1 m corresponds to a helical travel of 8 m, as expressed by the above-noticed speed ratio. The filament, however, does not lead to a pronounced radiation increase toroidally π around, because firstly its shape might be strongly distorted due to the magnetic shear and secondly its luminosity reduces due to a dilution by the rapid helical expansion corresponding to the helical velocity of impurities noticed above.

Shut down control: The radial penetration speed of 250 m/s is indeed slow, compared to the helical and poloidal ion propagation. It can not be accelerated by enhancing the reservoir pressure of the gas cell by a factor of four and it is quite constant in case of a doubled thermal plasma energy. This hints at an operational regime, which is decoupled from these particular jet and plasma parameters. This can be seen directly in Figure VI.11, when comparing the pre-cooling time durations in the four different neon cases. Note this paragraph applies to neon only due to too small parameter variations in argon and helium.

Radial penetration interruption accompanied by an *intensive radiation burst:* As discussed above, filaments transport impurities away from the penetrating radiation front. The penetration itself was interrupted in some cases shortly before the major disruption. The interruption occurs when the front approaches a certain penetration depth close to

[7]This issue is presented for a neon case in Figure VI.10.

the plasma core, with the consequence of a sudden, very intensive emission burst. The equilibrium is perturbed such that magnetic flux reconstructions might not be accurate anymore. We thus conservatively estimate that the radiation front could have approached to a certain q, which is critical for MHD mode excitation. In these experiments, an approximate q of 1.7 was noted. It lies in between two critical values for q: The resonant q of 1.5 ($m/n = 3/2$) was observed e. g. in pellet injection scenarios as a threshold for producing the so-called core snake [71]. And the resonant $q = 2$ surface is commonly known as a region, which strongly reacts on perturbations with the production of tearing modes. In the here presented cases, however, mode excitation was not confirmed at those respective times.

The thermal and current quench phases: For collisional runaway suppression, the density in the current quench must be sufficiently high. While helium fully penetrates into the plasma core in the late disruption phase and radiates from a well centred plasma, both neon as well as argon, do not penetrate to the very centre but their radiation remains at the high field side in the region between inner heat shield and centre. Whether the penetration depth of neon or argon is enough for suppressing runaway avalanching is a subject for future investigations.

Outlook:

On the basis of both the investigations on radiation dynamics carried out in this thesis and the density related elaborations published by Pautasso *et. al.* [26], we clearly envisage further actions, first and foremost the double-jet approach with one additional injector installed on the high-field side. The possibility of employing two injectors at toroidally spaced locations surely offers a greater scope for modifying the shut down scenario. Generally, investigations on massive gas injection scenarios are, for the time being, restricted to experimental strategies because the complicated three-dimensional toroidally and poloidally asymmetric radiation dynamics challenge currently available simulation codes. Mostly for this reason, the great deal of improvements to the diagnostic equipment are of important value in order to get new insights by keeping pace with the rapidly developing radiation structures during a massive gas injection scenario. This thesis demonstrated that it is worthwhile to further develop new XUV cameras. A conceivable approach, with respect to the application of multilayer reference detectors for the VUV spectral region, is constituted by water-cooled diode housings equipped with an externally moveable shutter in order to firstly avoid severe mechanical stresses by thermal loads and secondly shield the highly sensitive coatings from particle and photon radiation fluxes during standard discharges.

With respect to the density measurement during the shut down scenario, this thesis revealed that the radiation magnitudes vary strongly with the measurement position, which gives rise to spatially concentrated impurity accumulation. Therefore, further interferometer lines at least at one additional toroidal position are mandatory.

Bibliography

[1] H. A. Bethe: Energy production in stars. Amsterdam: Elsevier Publishing Company; 1972

[2] ITER: Homepage. Cadarache: Internet 30.04.2010 (http://www.iter.org)

[3] Fusion for energy: Homepage. Barcelona: Internet 30.04.2010 (http://fusionforenergy.europa.eu)

[4] J. Wesson. Tokamaks. Oxford: Clarendon Press; 2004

[5] R. Dux: Impurity Transport in Tokamak Plasmas. Habil. Universität Augsburg, 2004.

[6] Max-Planck-Institut für Plasmaphysik: Internet 30.04.2010 (http://www.ipp.mpg.de)

[7] H. P. Summers. Atomic data and analysis structure users manual. Abingdon: JET Joint undertaking; 1994

[8] M. Sokoll: MHD-Instabilitäten in magnetisch eingeschlossenen Plasmen und ihre tomographische Rekonstruktion im Röntgenlicht. Diss. Technische Universität München, 1997.

[9] P. J. Mc Carthy. Phys. Plasmas; 6, 9 (1999)

[10] B. B. Kadomtsev. Soviet Journal of Plasma Physics; 1, 5 (1975): 389...391

[11] International Radiation Detectors, Inc: Brochure: Internet 30.04.2010 (http://www.ird-inc.com)

[12] V. G. Weizer, *et. al.* J. Appl. Phys.; 50, 4443 (1979)

[13] T. Yunogami, T. Mizutani, K. Suzuki, S. Nishimatsu. Japanese Journal of Applied Physics; 28, 10 (1989): 2172

[14] H. R. Harrison, S. Dimitrijev. Microelectronics Journal; 22, 3-38 (1991)

[15] S. M. Ritzau, H. O. Funsten, R. W. Harper, R. Korde. IEEE Transactions on Nuclear Science; 45 (1998): 2820...2825

[16] L. R. Canfield, R. E. Vest. Metrologia; 35 (1998): 329...334

[17] E. M. Gullikson, R. Korde, L. R. Canfield, R. E. Vest. Journal of Electron Spectroscopy and Related Phenomena; 80 (1996): 313...316

[18] R. Korde, C. Prince, D. Cunningham, R. E. Vest, E. Gullikson. Metrologia; 40 (2003): 145...149

[19] K. F. Mast, J. C. Fuchs, M. Allgäuer, P. T. Lang, M. Münch, R. Reichle, G. Schramm, G. Weber. Technisches Messen; 64 (1997): 164...171

[20] J. C. Fuchs, K. F. Mast, A. Herrmann, K. Lackner: Twodimensional reconstruction of the radiation power density in ASDEX Upgrade; 21$^{\text{th}}$ Conf. of the EPS, Montpellier, France, 1994.

[21] C. P. Tanzi: Emission of Soft X-Ray And Microwave Radiation From Tokamak Plasmas. Diss. FOM Instituut voor Plasmafysica, Rijnhuizen, The Netherlands, 1996.

[22] A. Flaws: The Role Of MHD Instabilities in The Improved H-Mode Scenario. Diss. Universitaet Stuttgart, 2009.

[23] C. Goerner: Tomographische Untersuchung von globalen Alfven-Eigenmoden am Stellarator Wendelstein VII-AS. Diss. Technische Universität München, 2002.

[24] M. Anton, *et. al.* Plasma Phys. Control. Fusion; 38 (1996): 1849...1878

[25] P. H. Rutherford. Phys. Fluids; 16, 1903 (1973)

[26] G. Pautasso, D. Coster, T. Eich, J. C. Fuchs, O. Gruber, A. Gude, A. Herrmann, V. Igochine, C. Konz, B. Kurzan, K. Lackner, T. Lunt, M. Maraschek, A. Mlynek, B. Reiter, V. Rohde, Y. Zhang, X. Bonnin, M. Beck, G. Prausner. Plasma Phys. Control. Fusion; 51 (2009)

[27] G. Pautasso, C. J. Fuchs, O. Gruber, C. F. Maggi, M. Maraschek, T. Pütterich, V. Rohde, C. Wittmann, E. Wolfrum, P. Cierpka, M. Beck. Nuclear Fusion; 47 (2007): 900...913.

[28] G. Pautasso, D. Coster, X. Bonnin, T. Eich, J. C. Fuchs, B. Kurzan, K. McCormick, B. Reiter, V. Rohde: Disruption mitigation in ASDEX Upgrade with the in-vessel fast valve. 22$^{\text{nd}}$ IAEA Conf. Fusion Energy, Geneva, Switzerland, 2008.

[29] ITER Physics Expert Group on Disruptions, Plasma Control and MHD, ITER Physics Basis Editors and ITER EDA. Nucl. Fusion; 39, 12 (1999): 2251...2389

[30] T. C. Henders, *et. al.* Nucl. Fusion; 47 (2007): 128...202

[31] D. G. Whyte, T. C. Jernigan, D. A. Humphreys, A. W. Hyatt, C. J. Lasnier, P. B. Parks, T. E. Evans, P. L. Taylor, A. G. Kellman, D. S. Gray, E. M. Hollmann. Plasma-Surface Interactions in Controlled Fusion Devices; 15 (2003): 1239...1246

[32] R. S. Granetz, E. M. Hollmann, D. G. Whyte, V. A. Izzo. Nuclear Fusion; 47, 9 (2007)

[33] M. Lehnen, A. Alonso, G. Arnoux, S. A. Bozhenkov: First experiments on massive gas injection at JET - consequences for disruption mitigation in JET and ITER. 36^{th} Conf. of the EPS, Sofia, Bulgaria, 2009

[34] G. Pautasso, T. Pütterich, C. J. Fuchs, O. Gruber, C. F. Maggi, M. Maraschek, V. Rohde, C. Wittmann, E. Wolfrum, P. Cierpka, M. Beck: Plasma shut-down with the fast impurity puff on ASDEX Upgrade; 34^{th} Conf. of the EPS, Warsaw, Poland, 2007

[35] T. C. Hender, R. Fitzpatrick, A. W. Morris, P. G. Cardolan, *et. al.* Nuclear Fusion; 32 (1992)

[36] J. T. Scoville, R. J. La Haye, A. G. Kellman, T. H. Osborne, *et. al.* Nuclear Fusion; 31 (1991)

[37] G. M. Fishpool, P. S. Haynes. Nuclear Fusion; 34 (1994)

[38] D. E. Roberts, D. Sherwell, J. D. Flectcher, G. Nothnagel, J. A. M. de Villiers. Nuclear Fusion; 31 (1991)

[39] J. A. Snipes, J. D. Campbell, P. S. Haynes, T. C. Henders, *et. al.* Nuclear Fusion; 28 (1988)

[40] R. J. La Haye, L. L. Lao, E. J. Strait, T. S. Taylor. Nuclear Fusion; 37 (1997)

[41] M. F. F. Nave, J. A. Wesson. Nuclear Fusion; 30 (1990)

[42] T. H. Jensen, A. W. Leonard, R. J. La Haye, M. S. Chu. Phys. Fluids; B3 (1991)

[43] P. C. Stangeby. The Plasma Boundary Of Magnetic Fusion Devices. Taylor & Francis Group, 2000

[44] E. J. Strait, L. L. Lad, L. L. Luxon, E. E. Reis. Nuclear Fusion; 31 (1991): 527

[45] P. Noll, *et. al*: Stabilization of vertical position and control of plasma shape in JET. 11th Symp. Austin, 1985, Vol. 1, IEEE, New York, 1986: 33...40.

[46] O. Gruber, G. Pautasso, V. Mertens, F. Mast, M. Schittenhelm, W. Suttrop, M. Ulrich. 15th Int. Conf. Seville, 1994, Vol. 1, IAEA, Vienna, 1995: 675...684.

[47] D. F. Howell, T. C. Hender, G. Cunningham. Nuclear Fusion; 47 (2007): 1336...1340

[48] H. Zohm, F. X. Soeldner, H. Bruhns, R. Büchse, F. Leuterer. Plasma Phys. Control. Fusion; 33 (1991): 1423

[49] J. Kesner, *et. al.* Nucl. Fusion; 35, 2 (1995)

[50] B. Lipshultz, *et. al.* Journal of Nuclear Materials; 145-147, 15 (1987)

[51] Y. Nakamura, R. Yoshino, Y. Neyatani, T. Tsunematsu, M. Azumi, N. Pomphrey, S. C. Jardin. Nucl. Fusion. 36 (1996)

[52] D. F. Düchs, G. Haas, D. Pfirsch, H. Vernickel. J. Nucl. Mater.; 53, 102 (1974)

[53] A. Herrmann *et. al.*: Change from low to high power load and edge profiles in comparable H-mode discharges in ASDEX Upgrade. 36th Conference of the EPS, Sofia, Bulgaria, 2009.

[54] T. Eich et. al. Plasma Phys. Control. Fusion; 49 (2007): 573-604.

[55] A. Kallenbach, M. Balden, R. Dux, T. Eich, C. Giroud, A. Huber, G. P. Maddison, M. Mayer, K. McCormick, R. Neu, T. Petrie, T. Pütterich, J. Rapp, M. Reinke, K. Schmid, J. Schweinzer, S. Wolfe. 19th International Conference on Plasma Surface Interactions, San Diego, USA, 2010.

[56] U. Samm, *et. al.* Plasma Phys. Control. Fusion; 35, B167 (1993)

[57] A. C. C. Sips, *et. al.* Nucl. Fusion; 49 (2009)

[58] L. Giannone, *et. al.* Plasma Phys. Control. Fusion; 47 (2005): 2123...2143

[59] M. Z. Tokar, *et. al.* Plasma Phys. Control. Fusion; 37, A241 (1995)

[60] K. Lackner, *et. al.* Plasma Phys. Control. Fusion; 36, B79 (1994)

[61] G. A. Ratta, J. Vega, A. Murari, G. Vagliasindi, M. F. Johnson, P. C. de Vries. Nuclear Fusion; 50 (2010)

[62] P. C. de Vries, M. F. Johnson, I. Segui. Nuclear Fusion; 49 (2009)

[63] C. G. Windsor, G. Pautasso, C. Tichmann, R. J. Buttery, T. C. Hender. Nuclear Fusion; 45 (2005): 337...350

[64] G. Pautasso, S. Egorov, Ch. Tichmann, J. C. Fuchs, A. Herrmann, M. Maraschek, F. Mast, V. Mertens, I. Perchermeier, C. G. Windsor, T. Zehetbauer. Journal of Nuclear Materials; 290-293 (2001): 1045...1051

[65] M Camplani, B. Cannas, A. Fanni, G. Pautasso, G. Sias, P. Sonato: Tracking of the plasma states in nuclear fusion device using SOMs. Engineering Applications of Neural Networks; 11^{th} EANN International Conference, London, 2009.

[66] D. Wroblewski, G. L. Jahns, J. A. Leuer. Nuclear Fusion; 37, 6 (1997)

[67] B. Esposito, G. Granucci, S. Nowak, J. R. Martin-Solis, P. Smeulders, L. Gabellieri, M. Maraschek, H. Zohm, G. Pautasso, L. Urso: Disruption control on FTU and ASDEX Upgrade with ECRH. 22^{nd} Conf. IAEA Fusion Energy, Geneva 2008.

[68] B. Esposito, G. Granucci, S. Nowak, J. R. Martin-Solis, L. Gabellieri, E. Lazzaro, P. Smeulders, M. Maraschek, G. Pautasso, J. Stober, W. Treutterer, L. Urso, F. Volpe, H. Zohm. Nuclear Fusion; 49, 6 (2009)

[69] K. Hoshino, M. Mori, Y. Yamamoto, H. Tamai, T. Shoji, *et. al.* Phys. Rev. Lett.; 69, 2208-2211 (1992)

[70] K. Gal. E. Belonohy, G. Kocsis, P. T. Lang, G. Veres. Nucl. Fusion; 48 (2008)

[71] F. Alladio, *et. al.* Plasma Phys. Control. Fusion; 35 (1993): B241...B251

[72] L. R. Baylor, T. C. Jernigan, S. K. Combs, S. J. Meitner, N. Commaux, D. A. Rasmussen, P. B. Parks, M. Glugla, S. Maruyama, R. J. H. Pearce, M. Lehnen. 23^{rd} IEEE/NPSS symposium (2009)

[73] M. N. Rosenbluth, S. V. Putvinskij, P. B. Parks. Nuclear Fusion; 37 (1997): 955...966

[74] Z. Yong-Zhen, F. Xing-Ya, G. Gan-Cheng, X. De-Ming, Z. Yin-Jia. Chin. Phys. Soc. and IOP Publishing Ltd; 15 (2006)

[75] D. H. Perkins. Introduction to high energy physics. Addison-Wesley Publishing Company Inc., 1987.

[76] H. Bolt, *et. al.* Journal of Nuclear Matter; 155-157, 256 (1988)

[77] H. Bolt. 16^{th} Symp. Fusion Techn., London, 1990.

[78] Bartels: Atomic and Plasma-Material Interaction Data for Fusion. Supplement to the Journal Nuclear Fusion; 5, 225 (1994)

[79] J. B. Withley: Atomic and Plasma-Material Interaction Data for Fusion: Supplement to Journal Nuclear Fusion; 1, 109 (1991)

[80] M. N. Rosenbluth, *et. al.* Nuclear Fusion; 37, 955 (1997)

[81] S. V. Putvinski, *et. al.* Plasma Phys. Control. Fusion; 39 (1997): B157...B171

[82] J. W. Yang, J. Y. Cao, Q. X. Zeng, *et. al.* Chin. Phys. Lett.; 14, 2 (2002): 230

[83] R. Nygren, T. Lutz, D. Walsh, G. Martin, M. Chatelier, T. Loarer, D. Guilhem. Journal of Nuclear Materials; 241-243 (1997): 522...527

[84] F. Saint-Laurent, C. Reux, J. Bucalossi, A. Loarte, S. Bremond, C. Gil, P. Moreau, J. L. Segui: Control of runaway electron beams in Tore Supra. 36^{th} Conf. of the EPS, Sofia, Bulgaria, 2009.

[85] J. R. Martin-Solis, B. Esposito, R. Sanchez, J. D. Alvarez. Phys. Plasmas; 6, 238 (1999)

[86] S. A. Bozhenkov, M. Lehnen, K. H. Finken. Plasma Phys. and Control. Fusion; 50, 10 (2008)

[87] H. Dreicer. Phys. Rev. Lett.; 117, 329-342 (1960)

[88] H. Smith, T. Fehler, T. Fülöp, K. Gai, E. Verwichte. Plasma Phys. and Control. Fusion; 51, 12 (2009)

[89] A. H. Compton. Phys. Rev.; 21, 5 (1923): 483...502

[90] F. M. Levington, *et. al.* Phys. Fluids B; 5, 2554 (1993).

[91] A. Mlynek, G. Schramm, H. Eixenberger, G. Sips, K. Mc Cormick, M. Zilker, K. Behler, J. Eheberg. Rev. Sci. Instrum.; 81,3 (2010)

[92] A. Mlynek: Real-time control of the plasma density profile on ASDEX Upgrade. Diss. Ludwig-Maximilians-Universität München, 2010.

[93] M. E. Maraschek: Alfénwellen in toroidaler Geometrie am Tokamak ASDEX Upgrade. Diss. Technische Universität München, 1997.

[94] D. Wagner, G. Grünwald, F. Leuterer, A. Manini, F. Monaco, M. Münich, H. Schütz, J. Stober, H. Zohm, T. Franke, M. Thumm, G. Gantenbein, R. Heidinger, A. Meier, W. Kasparek, C. Lechte, A. Litvak, G. G. Denisov, A. V. Chirkov, E. M. Tai, L. G. Popov, V. O. Nichiporenko, V. E. Myasnikov, E. A. Solyanova, S. A. Malygin, F. Meo, P. Woskov. Nuclear Fusion; 48 (2008)

[95] H. Höhnle, W. Kasparek, J. Stober, A. Herrmann, R. Neu, U. Stroth: Investigation of the O2- and X3-mode heating in ASDEX-Upgrade. 36^{th} Conf. of the EPS, Sofia, Bulgaria, 2009.

[96] V. Mertens et. al. Nuclear Fusion; 37 (1997)

[97] G. P. Maddison *et. al.* Nuclear Fusion; 43 (2003): 49...62

[98] A. Kallenbach *et. al.* Journal of Nuclear Materials; 639 (2001): 290...293

[99] A. Kallenbach, R. Dux, J. C. Fuchs, R. Fischer, B. Geiger, L. Giannone, A. Herrmann, T. Lunt, V. Mertens, R. McDermott, R. Neu, T. Pütterich, S. Rathgeber, V. Rohde, K. Schmid, J. Schweinzer, W. Treutterer. Plasma Phys. Control. Fusion; Vol. 52, no. 5 (2010)

[100] J. C. Fuchs *et. al.*: Radiation distribution during impurity seeding experiments in the full tungsten ASDEX Upgrade. Proc. 36^{th} EPS Conference on Plasma Physics, Sofia (2009)

[101] R. Dux et. al. Journal of Nuclear Materials; 309-391 (2009): 858-863.

[102] A. Kallenbach, J. C. Fuchs, T. Eich, L. Giannone, O. Gruber, A. Herrmann, L. D. Horton, C. F. Maggi, H. Meister, H. W. Müller, V. Rohde, A. Sips, A. Staebler, J. Stober. Nuclear Fusion; 49 (2009)